TRANSITION METAL PHOSPHORUS TRICHALCOGENIDE (MPX_3) AS SATURABLE ABSORBER FOR MODE-LOCKED THULIUM-DOPED FLUORIDE FIBER LASER

AZIM DANIAL BIN AZAM

INSTITUTE FOR ADVANCED STUDIES

UNIVERSITI MALAYA

KUALA LUMPUR

2023

TRANSITION METAL PHOSPHORUS TRICHALCOGENIDE (MPX_3) AS SATURABLE ABSORBER FOR MODE-LOCKED THULIUM-DOPED FLUORIDE FIBER LASER

AZIM DANIAL BIN AZAM

DISSERTATION SUBMITTED IN FULFILMENT OF THE REQUIREMENTS FOR THE DEGREE OF MASTER OF PHILOSOPHY

INSTITUTE FOR ADVANCED STUDIES

UNIVERSITI MALAYA

KUALA LUMPUR

2023

UNIVERSITY OF MALAYA

ORIGINAL LITERARY WORK DECLARATION

Name of Candidate: Azim Danial bin Azam

Registration/Matric No.: 17166959/3

Name of Degree: Master of Philosophy

Title of Project Paper/Research Report/Dissertation/Thesis ("this work"):

S-Band Mode-Locked Thulium-Doped Fluoride Fiber Laser Using Transition Metal Phosphorus Trichalcogenide As Saturable Absorber

Field of study: Physical Science

I do solemnly and sincerely declare that:

(1) I am the sole author/writer of this Work;
(2) This Work is original;
(3) Any use of any work in which copyright exists was done by way of fair dealing and for permitted purposes and any excerpt or extract from, or reference to or reproduction of any copyright work has been disclosed expressly and sufficiently and the title of the Work and its authorship have been acknowledged in this Work;
(4) I do not have any actual knowledge, nor do I ought reasonably to know that the making of this work constitutes an infringement of any copyright work;
(5) I hereby assign all and every right in the copyright to this Work to the University of Malaya ("UM"), who henceforth shall be the owner of the copyright in this Work and that any reproduction or use in any form or by having any means whatsoever is prohibited without the written consent of UM having been first had and obtained;
(6) I am fully aware that if in the course of making this Work, I have infringed any copyright whether intentionally or otherwise, I may be subject to legal action, or any other action as may be determined by UM.

Candidate's Signature Date:

Subscribed and solemnly declared before,

Witness's signature Date:

Name:

Designation:

ABSTRACT

In this work, the performance of three materials from the transition metal phosphorus trichalcogenide family (MPX_3) for generation of mode-locked pulses in the optical S-band region using thulium-doped fluoride fiber (TDFF) as gain medium were investigated. The advancement of technology and rise of industrial revolution 4.0 brings about a bigger need for ultrafast long-range telecommunication. The current use of C-band and L-band optical telecommunications are quickly being saturated. To encounter this, one prospect is to expand into the S-band. As such, major advancements of optical amplification technology for S-band is required. Generation of laser in S-band region was usually achieved by Erbium-doped fiber (EDF) as the gain medium. However, the high phonon loss of silica fiber in S-band reduces its efficiency. The alternative of this is the ZBLAN glass or known as fluoride glass. When doped with Thulium, this gain medium emits at 1500 nm wavelength when pumped with 1400 nm laser source. This is right within the S-band region. Furthermore, the low phonon loss of fluoride glass makes the laser system more efficient. Mode-locked pulse generation in the S-band region can be achieved through active or passive means. Passive pulse generation is comparatively simpler and cheaper than active in order to obtain megahertz repetition rates and picosecond pulse width. Previous studies have used semiconductor-based saturable absorber (SESAM) and carbon-based SA such as graphene. The use of MPX_3 material as saturable absorber is interesting as these materials have been proven in semiconductor and energy storage applications. The proposed laser system can shed light on the practicality of a new class of 2D material as a viable optical material in wide variety of photonics applications.

Keywords: *Metal Phosphorus Trisulfide, Saturable Absorber, Thulium doped Fluoride fiber laser, Mode-locking pulses*

ABSTRAK

Dalam kerja ini, prestasi tiga bahan daripada keluarga logam peralihan fosforus trichalcogen logam peralihan (MPX_3) untuk penjanaan denyutan mod terkunci di rantau jalur S optik menggunakan gentian fluorida berdop thulium (TDFF) sebagai medium perolehan telah disiasat. Kemajuan teknologi dan kebangkitan revolusi perindustrian 4.0 membawa keperluan yang lebih besar untuk telekomunikasi jarak jauh ultra pantas. Penggunaan semasa telekomunikasi optik jalur-C dan jalur-L dengan cepat menjadi tepu. Untuk menghadapi ini, satu prospek adalah untuk berkembang ke jalur-S. Oleh itu, kemajuan besar teknologi penguatan optik untuk jalur-S diperlukan. Penjanaan laser di julat jalur-S biasanya dicapai oleh gentian optik berdop Erbium (EDF) sebagai medium gandaan. Walau bagaimanapun, kehilangan fonon dalam gentian silika yang tinggi dalam jalur-S mengurangkan kecekapannya. Alternatifnya ialah kaca ZBLAN atau dikenali sebagai kaca fluorida. Apabila didop dengan Thulium, medium gandaan ini memancarkan pada panjang gelombang 1500 nm apabila dipam dengan sumber laser 1400 nm. Ini betul-betul dalam julat jalur-S. Tambahan pula, kehilangan fonon kaca fluorida yang rendah menjadikan sistem laser lebih cekap. Penjanaan denyutan mode terkunci di julat jalur-S boleh dicapai melalui cara aktif atau pasif. Penjanaan nadi pasif adalah secara perbandingan lebih mudah dan lebih murah daripada aktif untuk mendapatkan kadar ulangan megahertz dan lebar nadi picosecond. Kajian terdahulu telah menggunakan penyerap boleh tepu berasaskan semikonduktor (SESAM) dan SA berasaskan karbon seperti graphene. Penggunaan bahan MPX_3 sebagai penyerap boleh tepu adalah menarik kerana bahan ini telah terbukti dalam aplikasi semikonduktor dan penyimpanan tenaga. Sistem laser yang dicadangkan boleh memberi penerangan tentang kepraktisan kelas baharu bahan 2D sebagai bahan optik yang berdaya maju dalam pelbagai aplikasi fotonik.

ACKNOWLEDGEMENTS

All Praise to Allah S.W.T. for His Blessings, granting me the capabilities of improving myself and increasing my knowledge and the chance of completing this research and dissertation. I thank my supervisors Professor Ulung Datuk Dr. Harith Ahmad and Dr. Muhamad Zharif Samion for their guidance, support, and encouragement throughout this research. This dissertation would have been completed without their wisdom and guidance.

Additionally, I would like to thank all the staff members and lecturers of the Photonics Research Centre Universiti Malaya (PRCUM) for their cooperation and assistance. My gratitude extends to my colleagues and friends for their ideas, motivations, suggestions, and assistance throughout this work.

Special thanks to my parents for their unwavering support, making this whole endeavor possible in the first place, and making the result of this work much more worth it. I dedicate this work and its successes to them.

TABLE OF CONTENTS

LIST OF FIGURES

LIST OF SYMBOLS AND ABBREVIATIONS

AI	:	Artificial Intelligence
ASE	:	Amplified Spontaneous Emission
CNT	:	Carbon Nanotube
CW	:	Continuous Wave
DIW	:	De-Ionized Water
EDFA	:	Erbium-Doped Fiber Amplifier
EDX	:	Energy Dispersive X-ray
ESA	:	Excited State Absorption
FBT	:	Fused Biconic Taper
$FEPS_3$	:	Iron Phosphorus Trisulfide
FESEM	:	Field Emission Scanning Electron Microscope
FTIR	:	Fourier Transform Infrared
FWHM	:	Full-Width Half Maximum
GSA	:	Ground State Absorption
GVD	:	Group Velocity Dispersion
HRTEM	:	High Resolution Transmission Electron Microscope
IPA	:	Isopropyl Alcohol
ISO	:	Optical Isolator
IUPAC	:	International Union of Pure and Applied Chemist
JCPDS	:	Joint Committee on Powder Diffraction Standards
LD	:	Laser Diode
LPE	:	Liquid Phase Exfoliation
MCVD	:	Modified Chemical Vapor Deposition
$MnPS_3$	:	Manganese Phosphorus Trisulfide
MPX_3	:	Transition Metal Phosphorus Trichalcogenide
$NiPS_3$	:	Nickel Phosphorus Trisulfide
NIR	:	Near Infrared
NMP	:	N-Methyl-2-Pyrrolidone
OC	:	Output Coupler
OPM	:	Optical Power Meter
OSA	:	Optical Spectrum Analyzer
PC	:	Polarization Controller

PWG	:	Planar Waveguide
RBW	:	Resolution Bandwidth
RFSA	:	Radio Frequency Spectrum Analyzer
SA	:	Saturable Absorber
SC	:	Scandium
SESAM	:	Semiconductor-based Saturable Absorber
SMF	:	Single-Mode Fiber
SNR	:	Signal-to-Noise Ratio
TBP	:	Time-Bandwidth Product
TBPF	:	Tunable Bandpass Filter
TDFF	:	Thulium-doped Fluoride Fiber
TGA	:	Thermogravimetric Analysis
TLS	:	Tunable Laser Source
UV-Vis-NIR	:	Ultraviolet-Visible-Near Infrared
WDM	:	Wavelength Division Multiplexor
XRD	:	X-ray Diffraction

CHAPTER 1: INTRODUCTION

1.1 Overview

Technological advancement have connected mankind like never before. Early telecommunications relied on copper wires to send telegrams. Introduction of optical fiber 1996 changed the landscape of long-range telecommunication, using light to transmit information across massive undersea optical fiber cables. Since then, major advancements have been made to improve its performance, including the development of optical amplification technology operating across multiple range of bandwidth. Network operators are currently using optical systems operating over the C-band spectral region of between 1530 nm to 1565 nm. This is also known as the "erbium widow" as erbium dopant in silica fiber emits at this range. Since this is a common band (represented by the C in C-band) used for commercial purposes, this may not suffice for industrial applications such as machine learning, artificial intelligence (AI) development and data centres which requires high-speed links. To cope with that, some operators have expanded their capabilities to the "Long-wavelength" band (L-band), operating over the optical spectral region of 1565 nm to 1625 nm. Transoceanic transmission of C+L bands have been reported previously. Despite the availability of the ultra-wideband optical system, there are demands for more fiber capacity and wider telecommunications bandwidth as modern data transfers have achieved hundreds of terabits per second. The incoming commercialization of 6G telecommunications systems also threaten to overwhelm the current C+L band system. As such, further expansion of the available bandwidth is required.

One such prospect is the "Short-wavelength" band (S-band) which operates at the optical spectral region of 1460 nm to 1530 nm, just before the C-band. The S-band is a great candidate for bandwidth expansion due to its low fiber loss. Its proximity to C-band allows for almost

similar setup such as using erbium doped silica fibers as amplifier (EDFA). Transmission in the S-band utilizing EDFA both in field and laboratory research have shown low-noise with high optical gain characteristics. However, erbium-doped fibers shows an intense amplified spontaneous emission (ASE) which has a gain peak at 1530 nm (Sharma & Raghuwanshi, 2017). As this is at the edge of the S-band operation region. The silica host also has an inherently high phonon energy within the S-band region, reducing the efficiency of EDFA in that region. An alternative would be fluoride-glass host. Fluoride glass, or also known as ZBLAN (ZrF_4-BaF_4-LaF_4-AlF_4-NaF) is more transparent in the IR region of S-band (Jha et al., 2012). Fluoride glass also has lower phonon energy in comparison to silica glass, reducing non-radiative emission in form of heat. This also reduces the possibility of heat damage to the fiber and allows it to operate at a much higher power. Silica fiber also can only be doped up to 0.1 mol% dopant concentration. In contrast, fluoride fiber can be doped to several mol% concentration (Miyajima et al., 1994). This makes the packaging much more compact due to the shorter gain medium fiber length required. These factors also results in a higher operational efficiency. Thulium can be used as the dopant in fluoride fiber for emission in the S-band region.

Generally, a closed laser system, known as a laser cavity, generates a constant output power over time. This beam is known as continuous wave (CW). However, for a laser to carry information, it must be modulated. This will generate pulses which will carry binary data. Pulse generation in lasers are commonly divided into two different modes of operations such as Q-switching, and mode-locking. However, in data transmission, mode-locking is preferred as its ultrashort pulse duration allows for larger bandwidth and faster transmission speed . Mode-locked pulses are not only useful in telecommunications applications but have also proven

significant in various fields such as biomedical, manufacturing and material processing. Pulse generation of lasers can be achieved using either one of two methods; active and passive. Active method require the use of devices powered by external means. This usually results in a package that is bulky and complicated, requiring constant maintenance. As such, passive method is currently the preferred option for pulse generation due to its lower cost and compact package design, making it more efficient. This is mainly achieved using a device known as a saturable absorber (SA).

Saturable absorbers are devices with nonlinear optical properties that has a specific absorption loss for light that decreases at high optical intensities. One proven SA is the semiconductor saturable absorber, or SESAM, which have shown results with multiple gain mediums operating at different center wavelengths. However, bandwidth limitations and high manufacturing cost caused by complicated fabrication process limited its use. As a replacement, scientist are looking towards nanomaterials for their optical characteristics. One current commonly used nanomaterial for pulse generation is graphene. Graphene, however, have low modulation depth and high non-saturable loss. It also cannot withstand high operational optical power, affecting its long term reliability. Another option is to use a different family of nanomaterial. Researchers are looking toward the chalcogenides family, specifically the transition metal phosphorus trichalcogenide (MPX_3) family. The materials in this family have a general formula of $M^{II}PX_3$, where M, P and X represent the transition metal, phosphorus and a chalcogen, specifically S or Se. The monolayers of this materials are held in bulk form by the weak Van der Waals force, requiring little work to exfoliate. This family exhibits an intermediate band gap of 1.3 to 3.5 eV and have been successfully reported in semiconductor, energy storage and optoelectronics applications. MPX_3 materials' nonlinear optical features,

like saturable absorption, make them prime candidates for generating ultra-short pulses, vital in fields like telecommunications. Their rapid femtosecond to picosecond response times enable efficient pulse modulation, facilitating the creation of mode-locked pulses with short durations. MPX_3 materials have also been reported to have high thermal stability. Their broad S-band absorption and mechanical/thermal stability boost their versatility in mode-locked laser systems. However, there are little report of its use in laser applications, specifically as a saturable absorber. In this research, we study the performance of transition metal phosphorus trichalcogenide (MPX_3) as a saturable absorber in a thulium-doped fluoride fiber laser for mode-locked pulse generation in the S-band spectral region.

1.2 Problem statement

There have been various research into mode-locking operation in C-band, L-band and 2 μm spectral region. The advancement of technology demands further expansion of bandwidth. As such, research into S-band is required. Current S-band systems utilizes depressed cladding erbium-doped fiber. However, as mentioned previously, silica-hosted fiber gain mediums have low efficiency due to its high phonon energy when compared to fluoride fiber. For efficient mode-locking operation in S-band, the use of thulium-doped fluoride fiber should be investigated.

The use of saturable absorber as a passive mode-locker has piqued the interest of many researchers worldwide. The use of 2D materials such as graphene and carbon nanotubes have been successfully reported. Most recent development is the study on transition metal phosphorus trichalcogenides (MPX_3), which have shown outstanding performance in semiconductor, energy storage and optoelectronics fields. This makes it an interesting subject

for investigation together with the thulium-doped fluoride fiber. However, previous works on pulse fiber lasers using saturable absorbers in the S-band region are only focused on the generation of Q-switched pulses. Q-switched pulses typically have repetition rate in the kilohertz range and pulse width in the microsecond range. This causes the pulse to have lower peak power. The proposed solution is to generate mode-locked pulses in the S-band region, whereby this type of pulses has higher repetition rate, typically a few megahertz. The pulse widths of mode-locked pulses can be extremely short, in the pico- (10^{-12}) or femto-second (10^{-15}) region. Thus, the peak power of mode-locked pulses will be significantly higher than Q-switched pulses. Mode-locked fiber lasers are favorable for various applications such as high-speed data transmission and laser spectroscopy.

1.3 Thesis Objective

This research was done with the objective of analyze the performance of MPX_3 in thulium-doped fluoride fiber laser system as a saturable absorber for mode-locked pulse generation in S-band region. Achieving this requires two major steps of work:

1) To develop an MPX_3/arc-shaped fiber saturable absorber suitable for the generation of mode-locked pulses in the S-band region
2) To analyze the mode-locked pulses using MPX3/arc-shaped fiber as the saturable absorber and thulium-doped fluoride fiber as the gain medium

1.4 Thesis Arrangement

Prior to beginning any experiments, we need to understand the basic principles of fiber lasers in S-band along its current technologies and applications. We also need to understand the behavior of the thulium-doped fluoride fiber laser and its operation both in continuous wave

(CW) and pulsed operations, specifically mode-locked along with any past researches done on it. We then need to understand saturable absorbers and how to optimize a 2D material for mode-locking operations in S-band, specifically the metal phosphorus trisulfide (MPX_3) family. These are done in a literature review in Chapter 2. Chapter 3 summarizes the construction of the thulium-doped fluoride fiber laser for pulse operations in the S-band region along with the components used in its construct. The equipment used for analysis and their background and working principle are also depicted in Chapter 3. Chapter 4 presents the methodology of material syntheses and fabrication of the arc-shaped fibers used in this work. Chapters 5, 6, and 7 presents the experimental work including characterization of material and arc-shaped fiber for $FePS_3$, $MnPS_3$ and $NiPS_3$-based SA respectively. Results of pulse generation for each material are also presented in Chapters 5, 6, and 7. Tests of long-term stability are also reported. The dissertation is concluded in Chapter 8, which also makes recommendations for additional research projects to further advance the field of study.

CHAPTER 2: LITERATURE REVIEW

2.1 Overview

The first part of this chapter will discuss the history of fiber lasers and its developments. Following that, this chapter discusses the theoretical basis of the generation S-band fiber laser. The chapter next focuses on the Thulium-doped Fluoride Fiber gain medium that was implemented in this experiment. Pulse laser operations, specifically mode-locked pulses are discussed next, followed by the history and applications of saturable absorbers, particularly the one used in this experiment, transition metal phosphorus trichalcogenide (MPX_3).

2.2 Fiber Laser Technology

2.2.1 History of Fiber Laser

Since the demonstration of fiber lasers in the 60's by Snitzer *et al*. (Mary et al., 2014; Snitzer, 1961), it has shown tremendous improvements. Today, fiber laser are employed in various applications including industrial processing, materials development, medical treatment and diagnostics among others. Far from what was envisioned, advancement of fiber lasers and fiber optics has reformed laser technology. By that time, it was known that fiber optics can carry light. In 1965, Tippet *et al.* showed the possibility of information transfer process using fiber laser in their work (Tippett et al., 1965). However, due to Rayleigh scattering, viable communications via fiber optics was unachievable due to its high signal loss. A pair of United Kingdom based scientists by the name of Charles Kao and George Hockham (Kao & Hockham, 1966) then developed theories for limitations of glass in 1966. They concluded that the losses was a result of impurities within the fiber material itself. Further studies demonstrated that a material named fused-silica, or Silicon Dioxide (SiO_2) performed best. Their findings contributed to the development of fiber optics with a much better transmission, dropping the

attenuation value from 1000 db/km to just 20db/km, making long range signal transmission possible, revolutionizing optical communication. Development of a diverse fields of optical fiber based photonics applications was thrown into overdrive as network operators seek to replace the copper cables with fiber optics as demands increase for data transmission. For their discovery, Kao & Hockham was awarded with the 2009 Nobel Prize in Physics.

While Kao and his team provided a method for carrying data across fiber optics, the concept of fiber amplifier was first established in 1966, when Koester *et al.* reported observations of amplification and oscillation of light between aa passive core and its cladding (Koester, 1966). However, laser and photonics studies stagnated between the 70's and 80's (Urquhart, 1988). That was until a group of researchers from the Physics and Electrical Engineering Department of Southampton University showed fabrication of fibers doped with rare-earth ions. Pool *et al.* employed a modified chemical vapor deposition (MCVD) process to achieve doping in optical fibers (Poole et al., 1985). Since then, researchers have doped optical fibers with various rare-earth elements in an effort to create a viable laser amplifier. Some examples of elements used are Ytterbium, Thulium, Erbium and Holmium and showed promising capabilities (Agrawal, 2001). Some combinations of those elements, called co-doping were also employed with success such as Thulium-Holmium, Erbium-Ytterbium to name a few. With the presence of these amplifiers, new laser operation modes have also been discovered. This improves on previous restrictions in pulse width (duration) and energy resulting in light pulses achieving sub-nanosecond pulse width (Csele, 2011; Gursel, 2018).

2.2.2 Fiber Laser Operation

Fiber laser works using the concept of spontaneous emission of atoms, specifically its dopant. There are two common energy states of an atom: ground when energy is at lowest and excited when energy level is increases within the atom. When an energy is supplied in a form of electromagnetic wave at a certain wavelength, in this case via pump, it is absorbed by the atom, exciting it electron to a higher energy level. This electron then spontaneously drops back to a lower energy level, emitting a specific wavelength (Addanki et al., 2018; Melton et al., 2018). This is called amplified spontaneous emission (ASE). Figure 2.1 illustrates a simple energy diagram of the process.

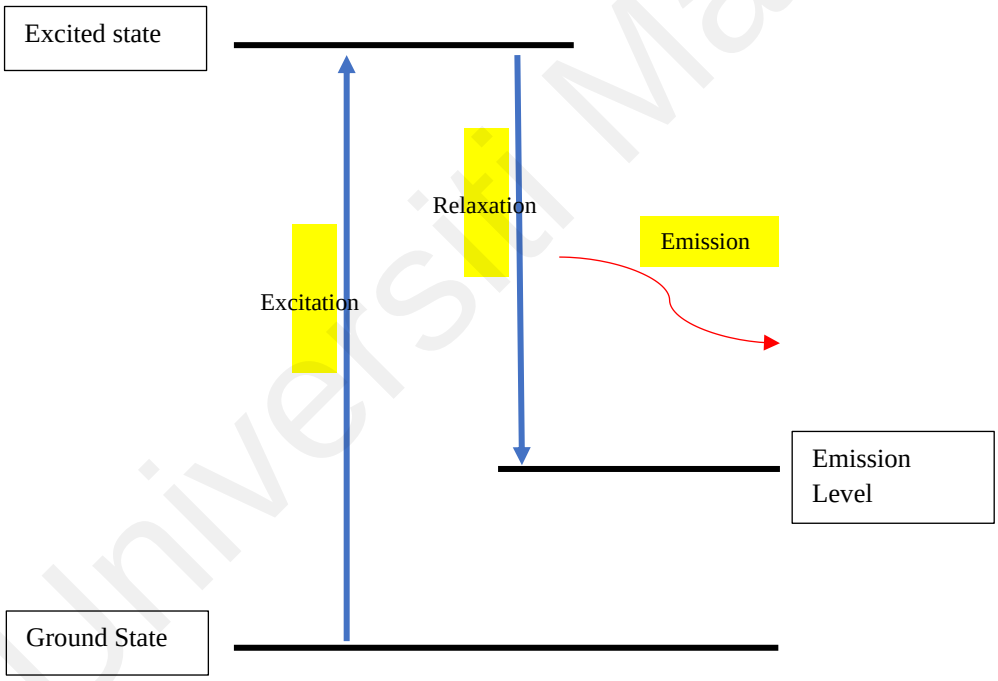

Figure 2.1: Simple energy diagram of ASE

Fundamentally, a fiber laser is a form of solid-state laser in which the active media being employed is an optical fiber which have rare-earth ions doped in them (Digonnet, 2001; Koester & Snitzer, 1964). A common structure of a basic longitudinally pumped doped-fiber laser system consists of two mirrors with the doped-fiber, called the gain medium, clamped in between. This structure is called a laser cavity. A pump source in form of laser in specific wavelength is supplied through the mirror on one side. The other side will propagate out the resulting lasing output beam along with any excess pump that have not been absorbed by the gain medium. A simplified schematic of the setup is shown in Figure 2.2. Within the gain medium, absorption of photon of the pump wavelength occurs, causing population inversion at the wavelength specific to the dopant in the gain medium (Urquhart, 1988). In turn, the light reflection within the cavity enables the emitted photon to then force the atoms at a higher state to discharge energy at specific wavelengths, resulting in a stimulated emission. As the emission are in phase, all photons resulting from the stimulated emission are coherent, resulting in laser of same frequency and energy.

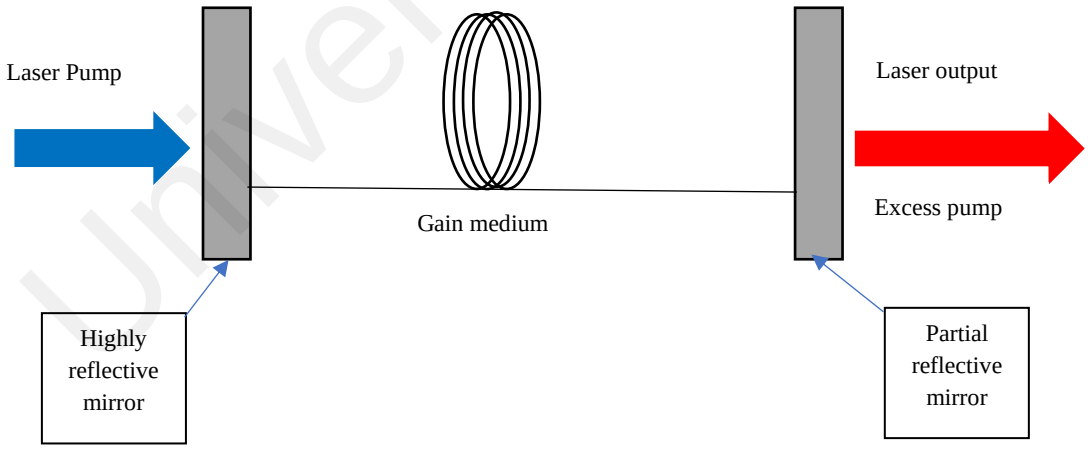

Figure 2.2: Ring laser cavity setup

Manufacturers can manipulate the dopants in fiber optics to achieve a desired wavelength emission and power. This makes the fiber laser versatile in terms of range of output wavelengths. Not only that, the simple construction of fiber laser makes it robust and reliable for use in multiple applications in the industry (Ahmed, 2015; Mur, 2011).

2.3 Optical short-wavelength band (S-band)

Currently, network operators are using the C-band region of wavelength range of 1530 nm to 1565 nm. Some industrial high-speed links also stretches into the L-band region of 1565 nm to 1625 nm, making use of C+L band telecommunications system over transoceanic distances. Both uses similar Wavelength Division Multiplexor (WDM) and Erbium-Doped Fiber Amplifier (EDFA) technologies. Compared to systems using only C-band, C+L band doubled the capacity of existing infrastructure. However, while C+L band is a commercial reality, that system is now quickly being saturated and demand for higher fiber capacity is at an all-time high as more and more data must be communicated faster than ever before. As such, expansion is necessary. Researchers are looking into expanding into the S-band using currently available infrastructure, incorporating it into the existing C+L band system. Predictions showed that the S+C+L band can double the current C+L capacity as shown in Figure 2.3 (Semrau et al., 2020)

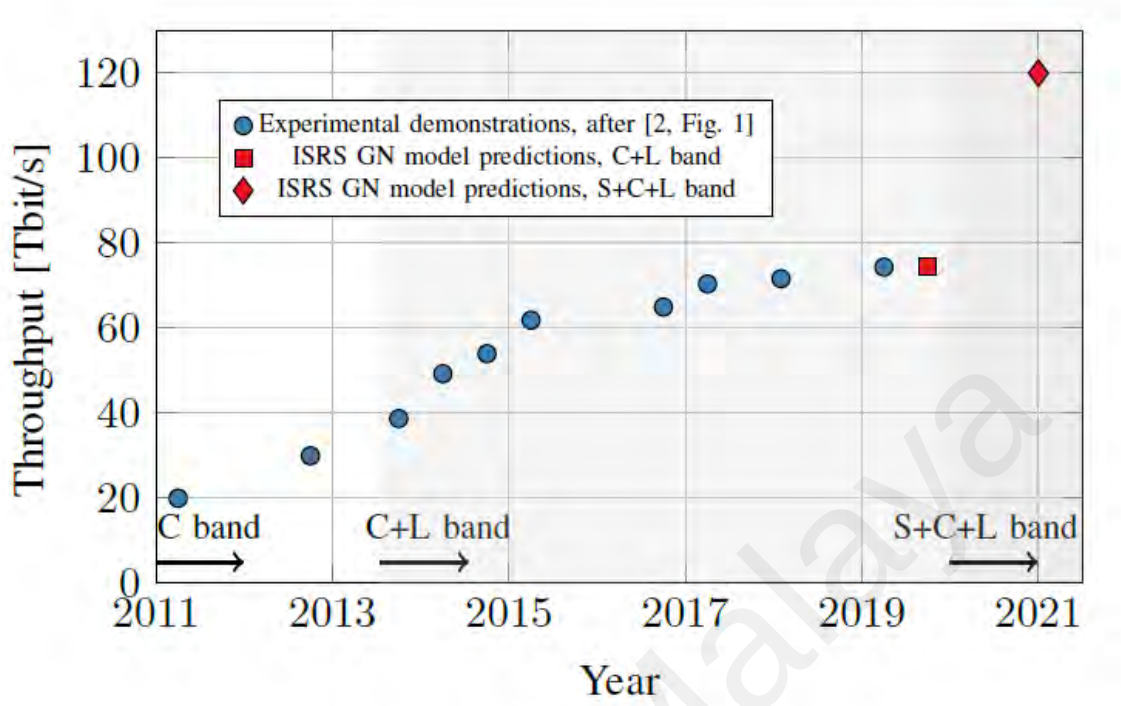

Figure 2.3: Throughput of C, C+L and prediction for S+C+L band (Semrau et al., 2020)

Currently, S-band are achieved using a conventional EDFA in both labs and practical uses. However, the amplification in S-band is limited due to issues such as incomplete active erbium ions inversion resulting in lower ASE. Lasing of EDFA also shows high peak at 1530 nm, which is not ideal for S-band operations (Arbore, 2005). Another method is using an augmented version of EDFA, the Depressed Cladding – Erbium Doped Fiber Amplifier (DC-EDFA). DC-EDFA emission wavelength range of 1488 nm to 1508 nm made it possible to be used as amplifier in the S-band region. However, DC-EDFA has a higher noise profile in comparison to EDFA (Ahmad et al., 2009). It is also very sensitive to polarization, which can be induced by bending and twisting the DC-EDFA fiber itself or even the fiber connecting it to other auxiliary components. Replacing the dopant in the silica glass fiber host with Thulium will allow for better emission at S-band. However, the silica host also contributes to high loss.

Silica have an inherently large phonon energy, making emission at S-band with Thulium dopant highly ineffective. A such, a replacement for silica glass fiber host for Thulium dopant for amplification in S-band must be investigated.

2.4 Thulium-doped fluoride fiber laser

Over the years since the introduction of optical fiber, the material of choice have always been silicon dioxide, also known as fused silica. Its capabilities to withstand high temperatures allows it to undergo arc fusion splicing at high current, allowing for ease of on-site fabrication. It also is known for having low scattering and absorption loss, suitable for telecommunication applications. In addition, fused silica is also capable of operating in humid and intense environment as it is hydrophobic and chemically resistant. Silica-based optic fiber can also be easily doped with rare-earth elements and have generated good amplification results. However, amplification in S-band proved to be difficult to achieve due to high phonon energy in silicon dioxide. A modified version of EDFA, which is commonly used for C-band amplification, known as the DC-EDFA, have been used for amplification in the S-band region. Nonetheless, its amplification is hampered by the high noise profile. DC-EDFA fiber laser system is also highly sensitive to polarization, making fine tuning an ultrashort pulse system difficult.

In this work, thulium dopant was used in a fluoride fiber host. The fluoride fiber is also known as the ZBLAN (ZrF_4-BaF_2-LaF_3-AlF_3-NaF), founded in 1975 by Poulain and his team (Poulain et al., 1975). Fluoride fiber have shown attenuation levels lower than that of modern silica fibers and closer to a theoretical best attenuation curve. This is shown in Figure 2.4. Fluoride fibers also possess a much smaller phonon energy at 600 cm^{-1} in comparison to silica

at 1100 cm^{-1}, further proving is capabilities in the IR region. Fluoride fibers also exhibits a low glass transition temperature, temperature dependent refractive index, and refractive index.

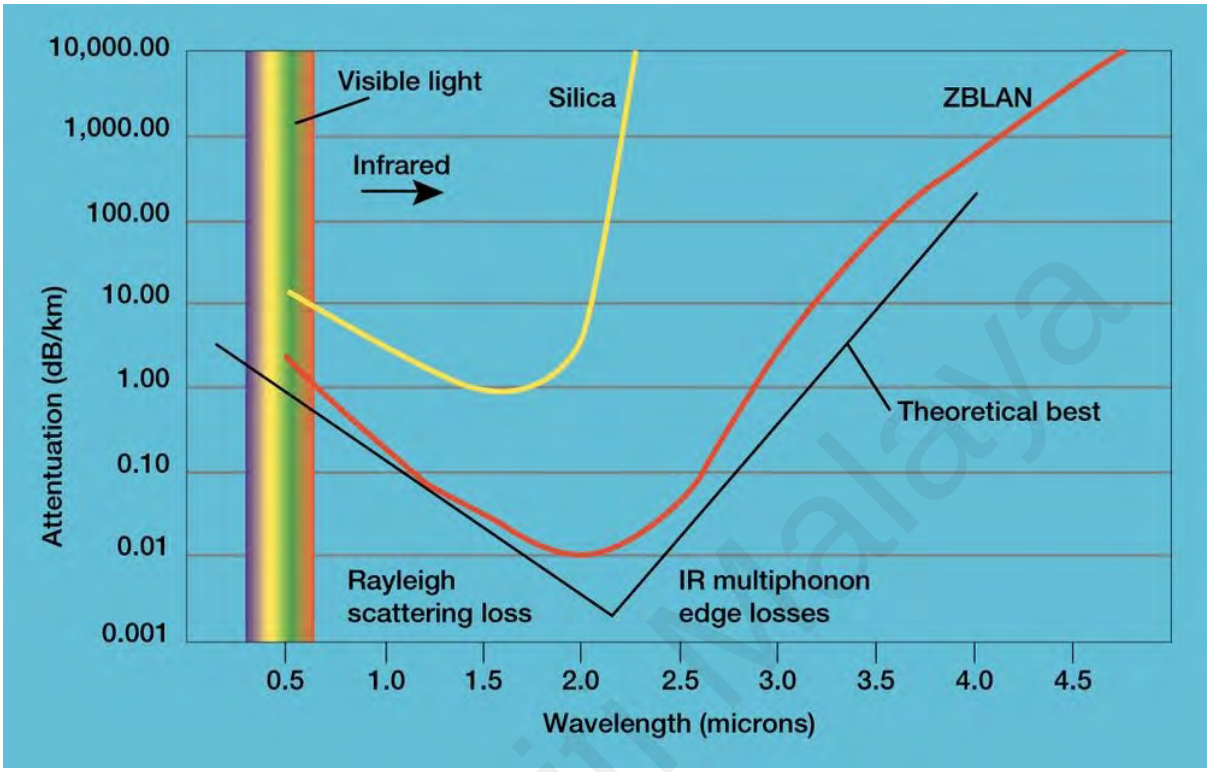

Figure 2.4: Attenuation of fluoride fiber in comparison to silica (NASA, 1998)

For amplification in S-band region, the dopant used in fluoride fiber is Thulium. Thulium is one of a group of seventeen chemical elements classified by the International Union of Pure and Applied Chemist (IUPAC) as a rare-earth element. Including Yttrium (Y) and Scandium (SC) (Leigh, 1990), these are a small group of elements of atomic number 57 (Lanthanum, La) to 71 (Lutetium, Lu) that are relatively plentiful in the Earth's crust, despite their name. Rare-earth elements have long been used as a dopant of optical fibers for use as amplifiers and laser applications (Bünzli & Piguet, 2005). One optically interesting attribute of these elements is their incomplete 4f subshell, allowing for electrons in that shell to travel freely between various

possible energy layers of the 4f subshell. Dissolution of Lanthanide ions in fluoride also meant that the ions possess a state of trivalent ionization with a transition spectrum closely identical to those of free ions (Digonnet, 2001).

For the application of laser generation, thulium ion (Tm^{3+}) are a preferred lanthanide element due to its wideband laser generation region capabilities. To better understand the electronic transition mechanism of Tm^{3+}, its energy level diagram is provided in Figure 2.5

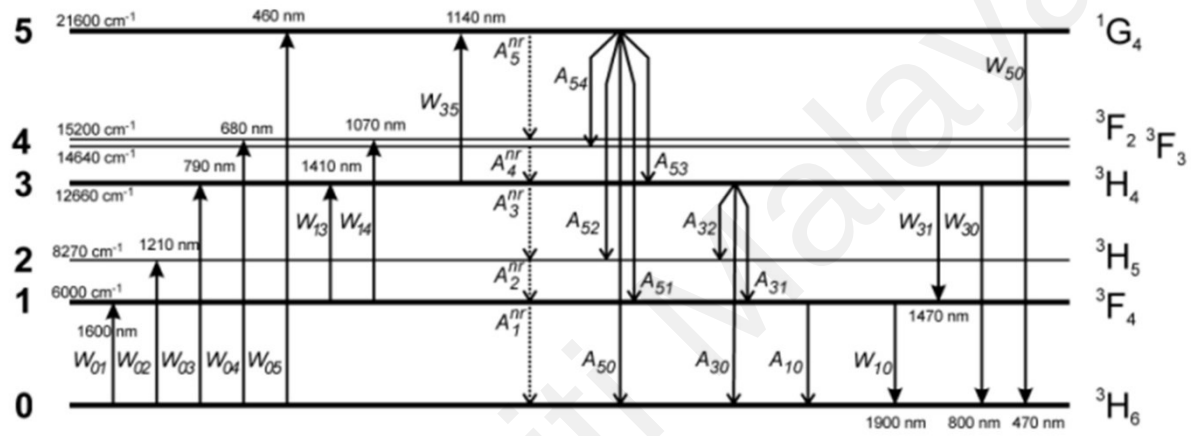

Figure 2.5: Tm^{3+} energy diagram showing possible transitions (Peterka et al., 2011)

We can see that S-band emission occurs at the wavelength of approximately 1470 nm, where the transition from $^3H_4$ to $^3F_4$ occurs. (Peterka et al., 2011). According to reports by Aosaza *et al.* and Floridia *et al.*, this can be achieved either by single or dual wavelength pumping (Aozasa et al., 2000; Floridia et al., 2004). The latter utilizes 2 different laser pumps at wavelengths 800 nm and and 1050 nm to achieve two-level energy hopping (Gomes et al., 2003). Pumping with 800 nm laser inducing the Tm^{3+} Ground State Absorption (GSA), exciting the electrons from level $^3H_6$ to $^3H_4$, and the 1050 nm laser depopulates level $^3F_4$ to $^3F_2$ using strong Excited State Absorption (ESA), simultaneously populating levels $^3H_4$ to $^3F_2$. These two

pumps generates population inversion, which results in the S-band emission via relaxation from $^3H_4$ to $^3F_4$.

Single pumping technique uses s single pump laser, making it much less complicated. This can be done by pumping either with a 1400 nm laser or 1050 nm laser, which would result in GSA and ESA from $^3H_6$ to $^3F_4$ and then to $^3H_4$. However, 1050 nm pump requires depopulation from $^3H_5$ to $^3F_4$ and from $^3F_2$ to $^3H_4$ energy levels, making 1400 nm pump preferable as it has direct GSA/ESA when compared to 1050 nm pump. Aosaza *et al.* reported using 1400 nm pump source for amplification in thulium-doped fiber, resulting in gain encompassing a wavelength range of 1480 nm to 1510 nm for ideal laser generation in the optical S-band region.

2.5 Pulse laser operations

A laser beam operation that has its output power constant over time is known as a continuous wave (CW) laser. It works by continuous replenishment of gain medium population inversion using a steady pump source. While some applications require CW, it is practically impossible in some lasing media, while other lasers may require continuous, extremely high power, oftentimes resulting in excessive heat release, destroying the laser. As such, another method of laser operation is required. Pulse laser refers to any operations of laser other than CW. In this case, the laser's optical power hits high intensities at regular intervals. This high intensity moments are ultrashort, usually in the range of micro-second down to femto-seconds magnitude. This operation of laser is also versatile. Some applications may require higher power, in which case the repetition rate can be reduced to allow for higher buildup of energy between each pulse. This can be done since the pulse energy is the result of average laser power against time taken between pulses (Popa et al., 2010)

Various researches have been done on laser pulse operations in the C-band region (Kasim et al., 2014; Muhammad et al., 2012; Zhao et al., 2014) as it was, and still is the commercial bandwidth for telecommunications. Similarly, expansion towards the L-band also resulted in intense research being done (Dong et al., 2011; Zhou et al., 2014) and even the 2 μm region have been in the spotlight thanks to its "eye-safe" range (Li et al., 2014; Wang et al., 2014). Even so, the constant demand for faster data transmission and larger bandwidth have pushed research interest towards the S-band region. This research achieves that by using a Thulium-doped Fluoride fiber laser system due to the Thulium ions emission in the S-band. In addition to that, the fluoride fiber host makes the system much more efficient as it has a lower phonon energy compared to common silica glass fibers.

2.5.1 Mode-locked pulses

Mode-locked pulses are ultra-short pulses operating at pico-seconds or even femto-seconds duration. These pulses are commonly highly intense and have a very strong signal with a high signal-to-noise ratio (SNR). Light, as we know it, is a type of electromagnetic waves which have different modes. As such, lasers operates with longitudinal modes which have slightly random phases within the operational wavelength. Mode-locking is a technique in which the random phase modes are matched at a certain time interval that matches the light round-trip within the laser cavity. This effectively locks the different modes, hence 'mode-locked'. The random modes are now in phase, making constructive interference as it oscillates within the cavity. The constructive interference generates a high intensity pulse in an ultrashort time. A modulator is commonly used as a method to lock the modes to achieve a mode-locked

operation. This is done by periodically modulating the loss within the system. Figure 2.6 visualizes this effect.

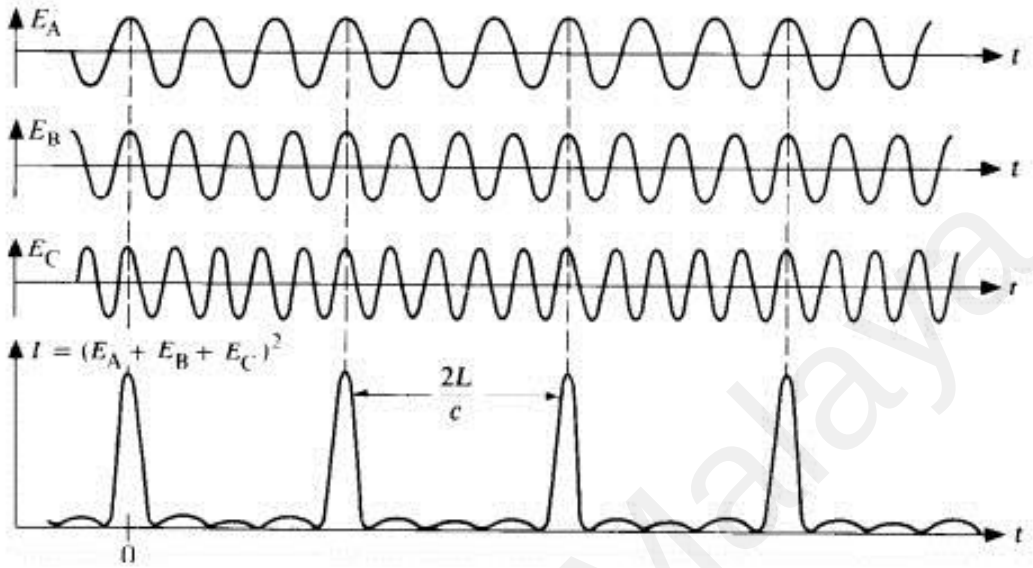

Figure 2.6: Mode-locking technique (Ennejah & Attia, 2013)

As mentioned, the time interval between each pulses matches the round-trip time of light within the cavity. This is called the repetition rate or frequency, and can be determined as follows:

$$Repetition\ rate = \frac{C}{Ln} \qquad Equation\ 2.1$$

where c, L and n identifies as light speed, length of cavity and refractive index of travel medium, and results in the unit Hertz (Hz). This formula can also be inversed to calculate for round-time of the laser cavity, with result in unit second (s). This equation also shows that with a longer cavity length, round-trip time takes longer resulting in a low repetition rate.

Mode-locking can be done by either active or passive means. The active method utilizes either an electro-acoustic or electro-optic modulators to periodically modulate the system's resonator loss. This method allows user to adjust the pulses generated by the laser system through adjustments of the modulators. However, since the modulators are a separate device and require its own power to operate, the resulting system will be very complicated and bulky. The same effect can also be achieved with a passive technique. Passive technique utilizes a device known as a saturable absorber (SA). This is commonly a preferrable method for users wanting a compact and simple package without the requirement of adjustable modulations. SA's operate off the laser itself, requiring no other source of power to do its job. With less complications to its setup, SA's also modulates loss much faster than its electronic, oftentimes resulting in a much shorter pulse width and in turn, much higher pulse energy.

2.6 Saturable absorbers

Saturable absorber (SA) are optical materials or elements that possess a nonlinear absorption characteristic, where its absorption is lower at high light intensities and vice versa. This is prominent in gain medium with absorbing dopant ions, where depletion of ground state ions can occur as a result of high intensities. This process bears resemblance to semiconductor operations, where absorption for photon energies are reduced when electrons are excited from the valence band to the conduction band.

The first reports of SA based mode-locking were reported using an organic dye in a ruby laser, resulting in nanoseconds pulse width (Mocker & Collins, 1965). The year 1966 saw De Maria *et al.* demonstrating a lower pulse width with picosecond pulses (DeMaria et al., 1966) and was further improved by Valdmanis *et al.* in 1986 with pulse width as low as 27 fs

(Valdmanis & Fork, 1986). Knowledge of semiconductor productions and operations improved by the 1990's and produced the semiconductor-based saturable absorber (SESAM). SESAM's were the preferred choice for mode-locking applications for a long time (Keller et al., 1996). Its operation uses the technique of quantum dot or multiple quantum well structures (MQW). SESAM's also have a longer lifespan and are generally robust. Nevertheless, the costly complicated production of SESAM's combined with its narrow operational bandwidth limited its use significantly. As such, researchers are looking toward nanomaterials as its replacement.

2.6.1 Transition metal phosphorus trichalcogenides

One interest of researchers for nanomaterial-based SA is the 2D and 3D materials, taking advantage of their unique optical characteristics for generation of ultrashort pulse lasers (He et al., 2019; Set et al., 2004). However, these materials do come with some major caveats. For example, graphene has low modulation depth, whereas 3D materials such as carbon nanotube (CNTs) have broadband operation which is dependent on its diameter and a high non-saturable loss (Kuo & Hong, 2014; Martinez & Sun, 2013). In search of a more reliable SA material, researchers look to a new member of the 2D nanomaterial family, metal phosphorus trichalcogenides. With intermediate bandgap of members of this family ranging between 1.3 to 3.5 eV, these materials exhibit huge potential applications in optoelectronics, semiconductor, and energy storage (Gui et al., 2021; Han et al., 2021; Wang et al., 2018; Wang et al., 2021). These materials are simplified using the general sum, $M^{II}PX_3$, where M can be the transition metal such as manganese (Mn), iron (Fe), copper (Co), nickel (Ni), or zinc (Zn), while X represents either selenium (Se) or sulfur (S) (Zhang et al., 2021). Similar to other 2D materials, each MPX_3 sheets are held to each other by the weak Van der Waals force, making it easy to

be thinned into several layers thick or even single layer nanosheets via liquid or mechanical exfoliation methods (Gusmão et al., 2019; Liu et al., 2019; Zhu et al., 2018).

CHAPTER 3: THULIUM DOPED FLUORIDE FIBER (TDFF) LASER CAVITY

3.1 Overview

The chapter encompasses the construction of the laser cavity system itself, introducing and explaining the role of every component used to ensure optimal operation of the thulium-doped fluoride fiber laser. This then proceeds to introduce the final cavity configuration optimized for mode-locking operations. The chapter will then introduce the measuring equipment necessary for the study of the mode-locking operation of the system such as the optical spectrum analyser (OSA), the oscilloscope, the radio frequency spectrum analyser (RFSA), and the autocorrelator among others.

3.2 Laser cavity setup

The generation of stable continuous wave thulium-doped fluoride fiber laser requires multiple crucial components to ensure optimal operation condition for mode-locking to occur. Construction of the ring laser cavity requires the use of components such as laser diode, wavelength division multiplexor, optical isolator, output coupler, and polarization controller, all connected in a loop. A stable and optimized laser cavity allows for the addition of an SA into the cavity to generate a mode-locked laser system by introducing nonlinearity into the laser. This subchapter will discuss the mechanism of each component and its significance in this work.

3.2.1 Laser Diode (LD)

Some semiconductor materials can generate light from a supply of electrical energy. The current flowing through the p-n junction of a semiconductor material will recombine the electron-hole pairs in its heterostructure, causing a release of energy in the form of photons.

This effect is spontaneous but can also be stimulated by an incident photon. This will result in optical amplification as the optical feedback from the photon in the laser resonator causes laser oscillation (Keiser, 1999). This is where the term laser derives from, the light is amplified as the result of stimulated emission within the laser resonator. The device using this concept is known as the laser diode.

While the most common semiconductor lasers are formed off the laser diode concept, there exists some lasers not requiring diode structures. As such, they do not belong to the diode laser category. These include optically pumped semiconductor lasers, and quantum cascade lasers. The former utilizes semiconductor materials that are undoped and cannot conduct significant current of electricity (Keiser, 1999). In this work, a FOL 1405RTD – 657 – 1400 TEC laser diode obtained from Fitel Co. was attached to a Gooch & Housego EM595 Benchtop LD controller. The laser diode emits laser at 1400 nm wavelength. This is then used to pump the gain medium, stimulating emission in the S-band region. The LD setup is shown in Figure 3.1.

Figure 3.1: Laser diode attached to a controller

3.2.2 Optical Isolator (ISO)

Similar to the concept of a diode allowing current to pass in one direction and block it in the opposite direction in an electrical circuit, an optical isolator allows light to only pass in one direction and not the opposite. This is crucial as stray reflected light will cause feedback in the laser cavity, causing problems such as parasitic oscillations and frequency instabilities (Amemiya & Nakano, 2010). The LD can also be damaged by a stray backpropagation of light into the LD, making the ISO crucial in preventing unnecessary damage.

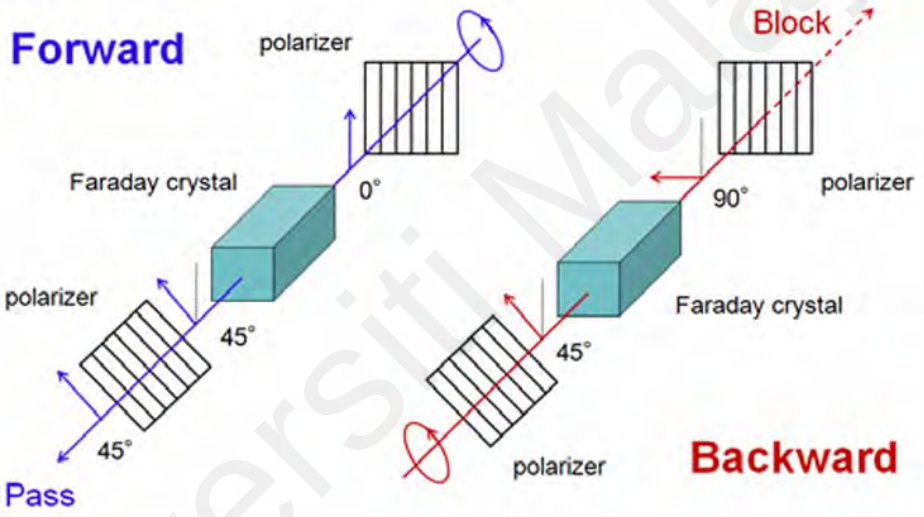

Figure 3.2: ISO schematics (Amemiya & Nakano, 2010)

ISO employs the concept of nonreciprocity using the Faraday effect. In this magneto-optic phenomena, an incident light passing through a transparent material will have its polarity rotated by the magnetic field. This magnetic field is parallel to the light propagation direction. In an ISO, polarizers are set at each end of a Faraday rotator. The input polarizer and output polarizer are angled in a way such that a forward propagating light have the similar polarity as

the output polarizer after it has passed the Faraday rotator, and light propagating backward will have a polarity that is perpendicular to the input isolator after passing the Faraday rotator. This concept have been further explained by Amemiya and Nakano in 2010 and their schematics, shown in Figure 3.2, further clarifies the concept (Amemiya & Nakano, 2010).

3.2.3 Wavelength-division multiplexing (WDM)

Wavelength division multiplexing is a method of sending optical signals of various wavelengths down a single fiber. The signals are combined, transmitted within the same fiber, and then separated again at the end. This method allows for many channels, carrying different data, to be transmitted together. Transmission capacity of fiber optics can be maximised in this way and fibers, and even amplifiers are more efficiently utilised. In addition to telecommunications, WDM also serves as a method for multiple optical fiber-based sensors to be interrogated using just a single fiber (Ishio et al., 1984).

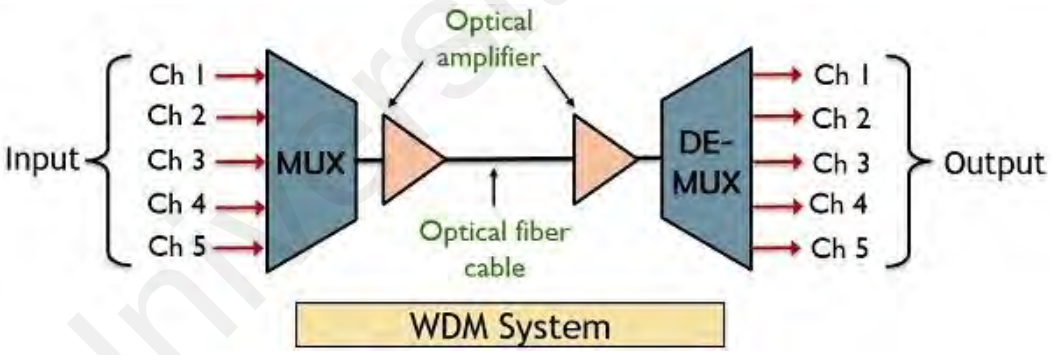

Figure 3.3: Wavelength-division multiplexing (Electronics, 2023)

In theory, massive channel bandwidth can be achieved by transmitting through a single fiber at high data rate. This way, we can exploit the maximum transmission capabilities of an optical

fiber. However, even with the wide available transmission bandwidth of a low-loss silica fiber, the data rate possible for silica glass fiber far exceeds the capabilities of current optoelectronic transceivers. Furthermore, the various dispersion values at different wavelengths will negatively impact wide bandwidth transmissions, restricting the maximum transmission distance. WDM method provides a solution to these problems by sustaining low rates of transmission at each channel, keeping between 10 to 100 Gbit/s. Combining multiple of these channels will result in total high data rate (Keiser, 1999). This is visualised in Figure 3.3.

In this work, the WDM is used twice in the ring laser cavity. The first WDM is used to isolate the 1480 nm wavelength light emitted by the TDFF gain medium in the cavity from the 1400 nm wavelength light pumped by the LD into the cavity. A second WDM is then used after the gain medium. This is to remove excess pump from the LD, preventing it from entering the ring laser cavity. Thus, allowing for easier mode-locking.

3.2.4 Optical coupler (OC)

One of the basic components of any fiber optic setups is the optical coupler (OC). Commonly used couplers are also called FBT splitters or FBT couplers, named after the technique used to fabricate the OC. The fused biconic taper (FBT) method splits optical power and/or wavelengths by fusing the two bare, tapered fibers in the shape of an "X". The fused section is then pulled until the targeted optical characteristics are met. Multiple FBT OC's can be fused to form a tree structure which coalesce the splitting effects for an output power ratio of 1xN or 2xN, in which N represent the number of outputs.

For the use of splitting light into two outputs with minimal loss, common FBT coupler used is the 1x2 OC, which can also be used to achieve the effect of merging two lights into one output. For this study, we will use a 1x2 FBT OC with output ratio of 90%:10%. Figure 3.4 illustrates a 1x2 coupler.

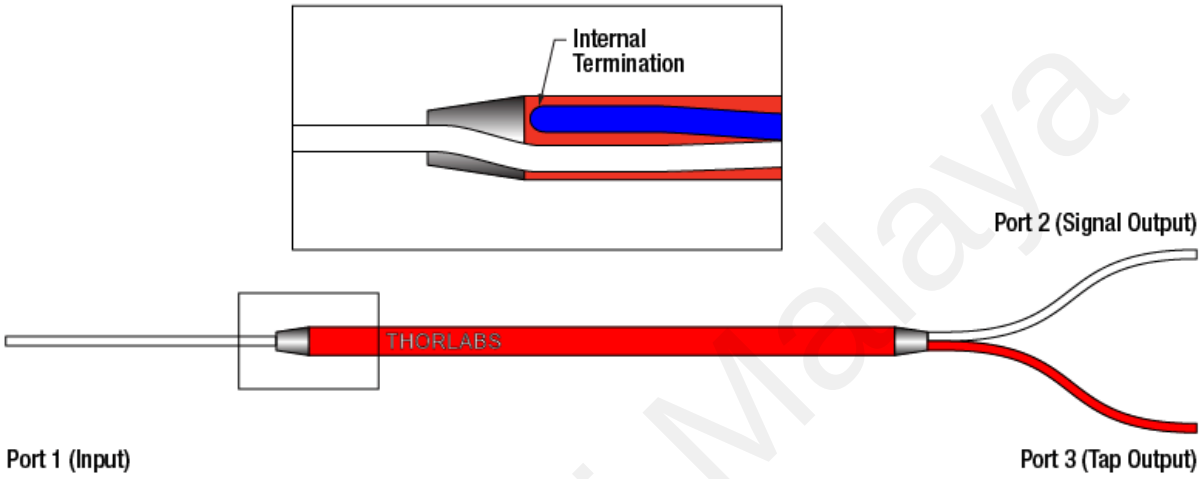

Figure 3.4: 1x2 FBT optical coupler (Thorlabs, 2023)

3.2.5 Polarization controller (PC)

Birefringence effect can be induced on an optical fiber when physical stress such as bending twisting. The polarization controller (PC) takes advantage of this property to allow for predictable control of a system's polarization. One common type of PC is the "bat ear" controller. This method uses holders which allows users to coil (in effect, bend) the fibers on the paddles. The total retardation is inversely proportional to the bending radius of the holder. The retardation amount is also dependent on the length of the fiber used, i.e., the number of loops on the holder. Some PCs have holders which allow users to set the number of turns (in

effect, length) of the loops in the holder. This method allows for the control of λ/2 (half-wave) or λ/4 (quarter-wave).

Commonly used configuration of a PC is the 3-paddle configuration. Three coils of set number of fiber loops are used in a sequence, where the middle acts as the half waveplate while the two outer ones acts as the quarter waveplates. The coils can be rotated independently around the axis in line with the input and output fibers. Adjusting the position of the paddles allow for the alteration of the input polarization state into any output state while maintaining the wavelength. Figure 3.5 shows the concept of polarization controller and an example of a PC.

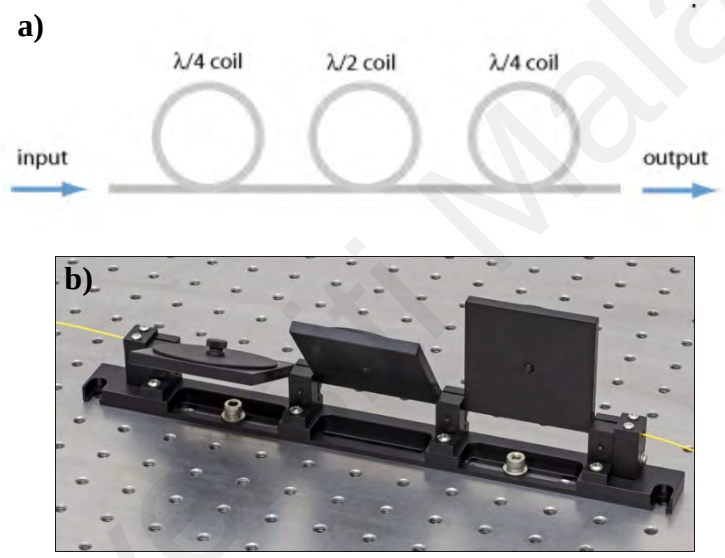

Figure 3.5: (a) polarization controller concept (b) 3-paddled polarization controller (Thorlabs, 2023)

3.2.6 Final cavity configuration

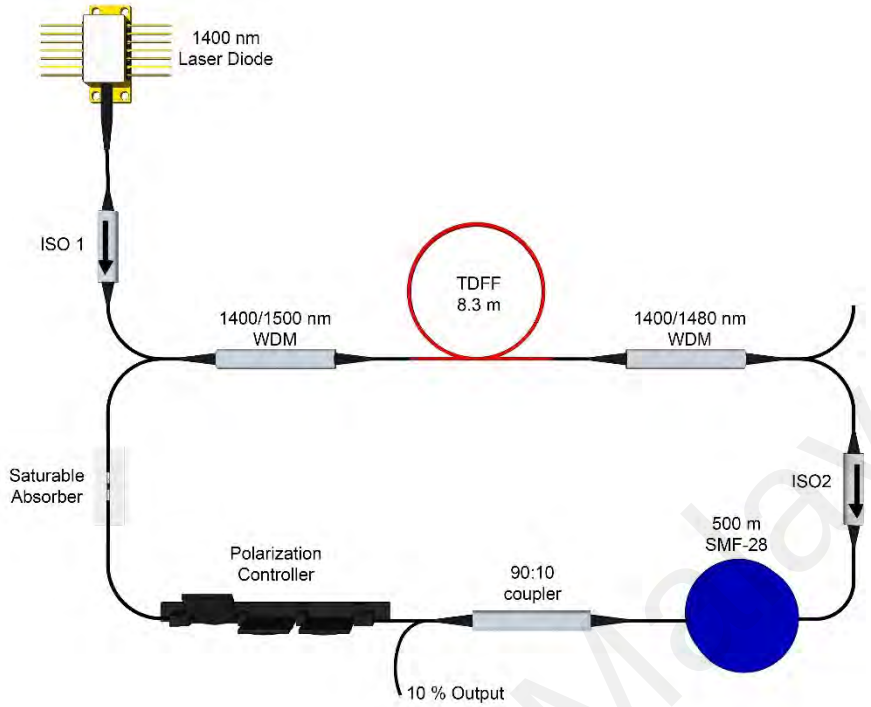

Figure 3.6: Final laser cavity configuration

The final laser cavity configuration is as shown in Figure 3.6. The LD used is from Fitel Inc., model number FOL 1405RTD. This LD is capable of generating a pump laser of 1400 nm wavelength with the pump power reaching up to 280 mW. The LD is controlled with a Gooch & Housego EM595 Benchtop LD controller. The LD is then spliced to a 1400 nm ISO for one-direction light propagation, crucial to the safety of the LD as back-propagation of the laser will damage the LD. The pump is introduced into the cavity via the 1400 nm port of a 1400/1500 nm WDM. The WDM's common port is then connected to the TDFF gain medium.

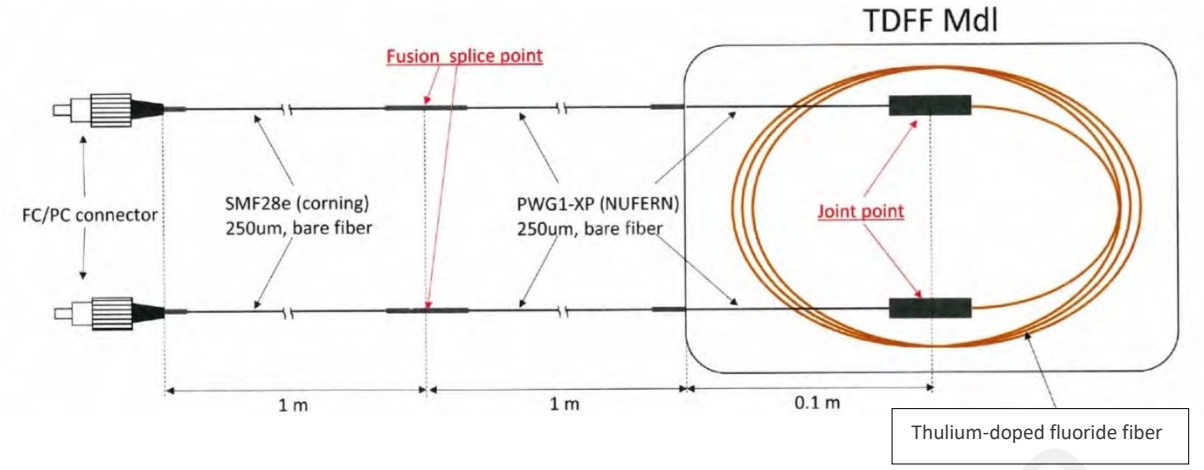

Figure 3.7: TDFF configuration

The 8.3 m TDFF gain medium was obtained from FiberLabs Inc. and came in a hermetically sealed metal box. This is to prevent degradation on the gain medium fiber as it is sensitive to humidity. According to the schematics of the fiber provided by FiberLabs as shown in Figure 3.7, the gain medium was mechanically joined to a planar waveguide (PWG) fiber (NUFERN, PWG1-XP) for optimal coupling efficiency. The PWG fiber pass through the metal box via a gromet and is then spliced to a pair of SMF-28e pigtails.

After the TDFF, another WDM was attached, a 1400/1480 nm WDM, similarly via its common port. The second WDM serves to reduce intracavity laser instability by reducing the excess pump power. Only the 1480 nm port is used from this WDM, where it is connected to an ISO. This second ISO ensures the intracavity light travels in a single direction. The ISO is then connected to a 500 m spool of SMF-28. The spool will help in stimulating mode-locking within the cavity (Ahmad et al., 2022). As the gain medium possesses a highly positive value of material dispersion, the spool will also serve to push the net cavity dispersion to a negative value for a more stable and higher power mode-locked laser. Next, a 90/10 OC was then attached to the SMF spool to allow for 10% of the signal to be extracted for analysis. The 90%

port of the OC is the connected to a PC for intracavity polarization adjustments. This is then connected to the $FePS_3$/arc-shaped fiber SA. the cavity is completed by connecting the SA back to the 1500 nm port of the first WDM.

Without the SA, the laser cavity configuration shown in Figure 3.20 successfully generated a lasing spectrum with a lasing wavelength of 1480 nm. The lasing spectrum is shown in Figure 3.8.

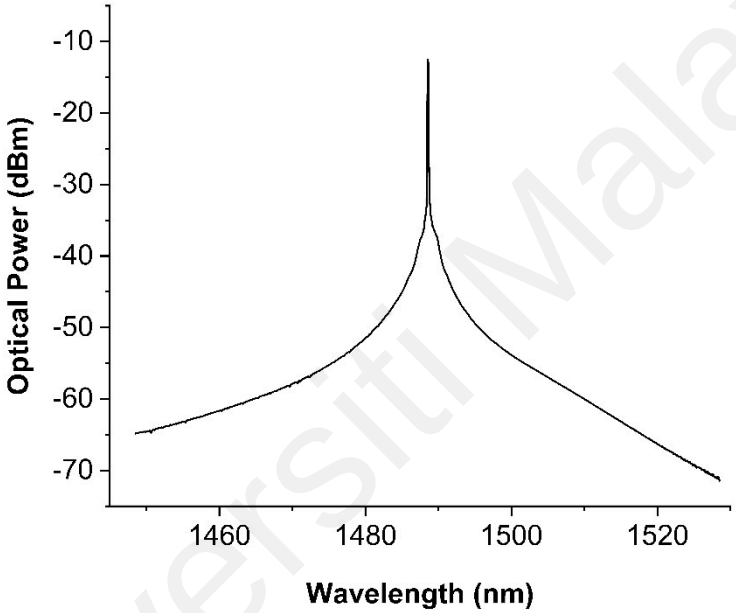

Figure 3.8: Lasing spectrum of TDFF cavity

The completed laser cavity measured a total length of 525 m. This includes the 8.3 m TDFF gain medium, the PWG and SMF included with the gain medium, the 500 m SMF-28 spool, and all connections with the other components (WDM, ISO, PC, OC) which are made from SMF-28 pigtails. As provided by FiberLabs, the gain medium manufacturer, the TDFF has a material dispersion of -8.30 ps nm^{-1} km^{-1}, while Corning provided the SMF-28 material

dispersion value of 14.3 ps nm^{-1} km^{-1}. Calculations showed the group velocity dispersion (GVD) of both types of fibers are 0.010 ps^2 m^{-1} and -0.017 ps^2 m^{-1}, respectively. The net cavity dispersion was calculated using the formula:

$$L_{SMF}GVD_{SMF} + L_{TDFF}GVD_{TDFF} \quad \text{Equation 3.1}$$

Considering a mode-locked central wavelength of 1504.8 nm, the net cavity dispersion was determined to be -8.80 ps^2 at 1504.8 nm. The 500 m SMF-28 spool employed in the cavity contributed to the significant net anomalous dispersion value.

3.3 Characterization of mode-locked pulse operation in Thulium-doped fluoride fiber laser

A number of methods will be used to characterize the TDFF mode-locked pulses generated by the $FePS_3$/arc-shaped fiber SA. First, the optical spectrum of the mode-locked pulses will be analyzed. This is achieved using an AQ6370C Optical Spectrum Analyzer (OSA) obtained from Yokogawa. Next, we will analyze the pulse train of the mode-locked laser using a InfinitiVision DSOX3102T oscilloscope from Keysight, attached to a ThorLabs DET08CFC/M photodetector. The similar photodetector will also be used for the radio frequency analysis, this time attached to a Rohde & Schwarz FPC1000 Radio Frequency Spectrum Analyzer (RFSA). The laser's single pulse analysis was done using an autocorrelator from Alnair, model number HAC-200. Output power analysis is done using a ThorLabs S144C Optical Power Meter (OPM) attached to a USB interface (ThorLabs, PM100USB) into a computer.

3.3.1 Optical spectrum analysis

A light sources or light beam's optical (also known as emission) spectrum contains data on the distribution of optical energy or intensity over a certain wavelength. It is commonly presented in the form of spectral radiance, intensity, or flux against wavelength. Some equipment can present the data in a logarithmic scale, with unit dBm/nm, as used in this study. The equipment used to record the optical spectra of a light source is called an optical spectrum analyzer (OSA). Commonly, OSA's are a type of spectrographs, excluding certain OSA with different operational principles such as using Fabry-Pérot of Michelson interferometers.

As stated above, the analysis of the optical spectrum in this study uses the Yokogawa AQ6370C OSA. This OSA reports in unit dBm/nm with a wavelength range of 600 to 1700 nm. It possesses high wavelength accuracy of 0.01 nm with resolution of 0.02 nm. All these makes this OSA suitable for this study in the S-band spectral region.

3.3.2 Pulse train analysis

The term "light pulse" refers to brief flashes of light. Although lasers are commonly used for its generation, flash lamps can also be used to the same effect. A pulse laser system does not generate single pulse, but rather a regular sequence of pulses with a constant repetition rate. This is called a pulse train. The pulse repetition rate is measured by how many pulses event in a second, with the unit Hertz. The spacing of each singular pulse is the inverse. For mode-locking operations, pulse repetition rates are commonly very high with frequencies in the MHz to GHz region. The inverse of this represents the round-trip time of the cavity.

3.3.3 Radio frequency analysis

A measure of quality for an optical signal is the signal-to-noise ratio, or SNR. Often expressed in the unit decibels (dB), it is widely understood as the ratio of powers and not amplitudes. This concept typically relates to electrical power in a detector's output. SNR allows us to understand the signal integrity and reliability. Particularly in optical telecommunications, detecting a signal correctly and avoiding bit error is dependent on the signals SNR at the detector. In a laser system, the output is connected to a photodetector, resulting in a photocurrent with intensity proportional to the optical power. The noise can come from either optical influence or by the electronics in the detector. Its signal analyzed using a radio frequency spectrum analyzer (RFSA).

3.3.4 Pulse width analysis

Pulse width is the measure of time at which the laser is at its peak optical intensity. Frequently, pulse width is defined as the full width at half-maximum of the optical power against time. However, for soliton pulses, the parameter τ, can be used which is approximately the FWHM value of the pulse multiplied by the sech^2 deconvolution factor of 0.648. Along with the spectral bandwidth, the pulse width can be used to calculate the time bandwidth product (TBP) of the laser. The TBP allows us to understand how close a pulse is to its transform limit, an aspect of the pulse quality. A transform limited sech^2 pulse will have a TBP value of no less than 0.315 and pulses with higher TBP value is said to be chirped.

Measurements of pulse duration can be done using ultrafast photodetectors or photodiodes with and ultrahigh sampling oscilloscope. However, ultrafast pulses with pulse width in the picosecond range, such as mode-locked pulses, will require a device called an autocorrelator.

It works by splitting the incoming pulses into two, which is then superimposed in a nonlinear medium. This allows the device to check the correlation of the temporal pulse trace with itself.

CHAPTER 4: MPX_3/ARC-SHAPED FIBER FABRICATION

4.1 Overview

This chapter discusses the fabrication of the MPX_3/arc-shaped fiber saturable absorber. Initially, the method of MPX_3 material preparation, which is the liquid phase exfoliation method, will be discussed. Various characterization will be done on the each synthesized MPX_3 materials and will be discussed in Chapters 5, 6 and 7. This chapter then continues with the two-step method of the arc-shaped fiber fabrication, including an introduction into the concept of the arc-shaped fiber and how it works.

4.2 Preparation and fabrication of MPX_3

4.2.1 Liquid Phase Exfoliation

Liquid phase exfoliation is a common method of exfoliating 2D materials from its bulk form. Commonly used in the fabrication of graphene, it is used as a way to mass produce graphene in place of the physical exfoliation. It works by suspending the material in a liquid such as an organic solvent and sonicating the mixture. The ultrasound transmits through the mixture, causing ultrasonic-induced cavitation that ruptures the bulk form, forming large flakes. The large flakes then is again peeled again by the ultrasonic force, breaking the weak Van-der-Waals force between the layers of the flakes. This results in single-layer and few-layer exfoliated 2D material.

In this work, 100 mg of bulk MPX_3 crystals obtained from 2DSemiconductors USA was ground using a pestle and mortar into a powder and added into a vile with 10 mL 99% isopropyl alcohol. The solution was first vorticed to disperse the MPX_3 material completely. This mixture is then sonicated in a water-bath sonicator for a period of approximately 8 hours. The cavitation

effect caused by the ultrasound will break the weak Van-der-Waals forces between layers. The resulting suspension is then centrifuged at 5k revolutions per minute (RPM) for a period of 15 minutes to separate the unexfoliated MPX_3 and extract the supernatant for use in the SA device. The resulting solution is few-layers MPX_3 suspended in 99 % IPA at a concentration of 10 mg/mL. The LPE process is visualized in Figure 4.1

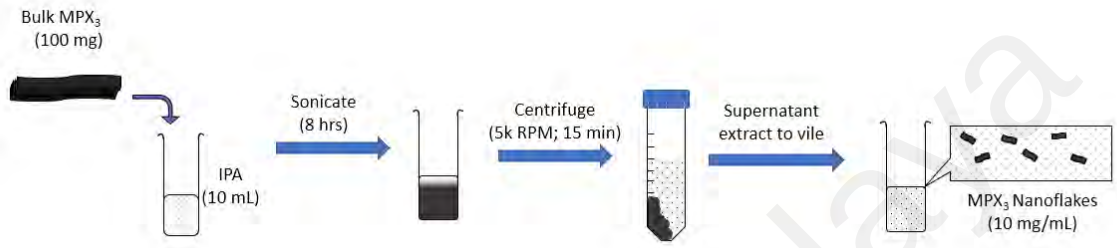

Figure 4.1: Liquid Phase Exfoliation (LPE) process of MPX_3 material

4.3 Fabrication of arc-shaped fiber

Arc-shaped fiber introduces the saturable absorber material into the laser system by means of evanescent wave interaction. In optics, evanescent wave forms when waves travelling through a medium (in this case, silica optical fiber) undergo total internal reflection at the boundary as the waves strikes it at an angle greater than that of the critical angle. A physical explanation of this phenomena would be that the electromagnetic field, in this case, light, cannot be discontinuous at the boundary. Arc-shaped fiber increases the exposure of the evanescent field onto the saturable absorber material by reducing the thickness of the optical fiber cladding, allowing for much stronger interaction between the evanescent wave of the propagating light and the saturable absorber material. This is visualised in Figure 4.2.

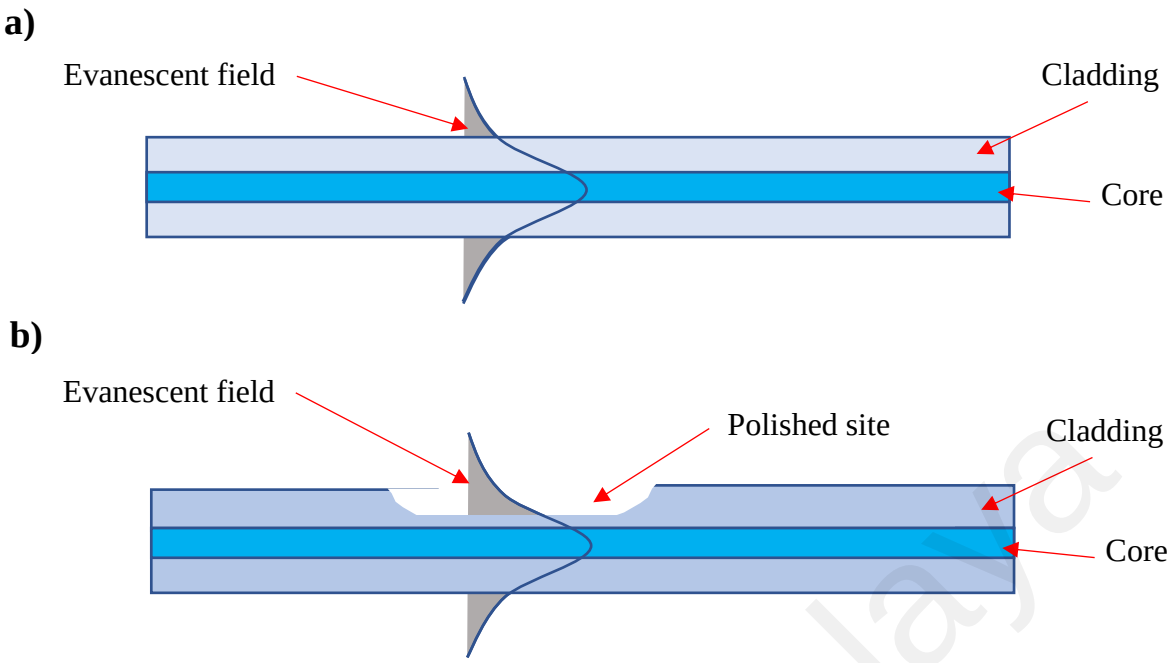

Figure 4.2: Evanescent field in (a) normal optical fiber and (b) arc-shaped fiber

The arc-shaped fiber was fabricated on a polishing stage as shown in Figure 4.3. This setup was designed and studied by Ahmad et al. (Ahmad et al., 2017). The arc-shaped fiber starts from a 1 m length of single-mode fiber (SMF-28) from Corning®. The fiber possesses a core diameter of 9 µm and cladding diameter of 125 µm. The fiber was first spliced to SMF-28 pigtails on either end. Approximately 3 cm of coating was stripped from the center of the fiber, exposing the cladding. The fiber was then clamped onto the stage, with the stripped section on top of the polishing wheel. One end of the pigtail was connected to a tunable laser source (TLS) while the second one was attached to an optical power meter (OPM). The polishing wheel was powered using a tunable DC power source and was wrapped in a 1x5 cm dimension, 30 µm grit size sandpaper. The polishing wheel was raised to contact the fiber, polishing it to an insertion loss of ~2.8 dB. The polishing wheel was then lowered, and its sandpaper was then replaced with a polishing sheet of similar dimension. The polishing sheet is a ThorLabs LFD1 polishing film with a 1 µm grit size. The polishing wheel was then raised again to the fiber and

polishing continued until total insertion loss of 3dB was achieved. The polishing wheel was then stopped and lowered. A glass slide was used to secure the fabricated arc-shaped fiber.

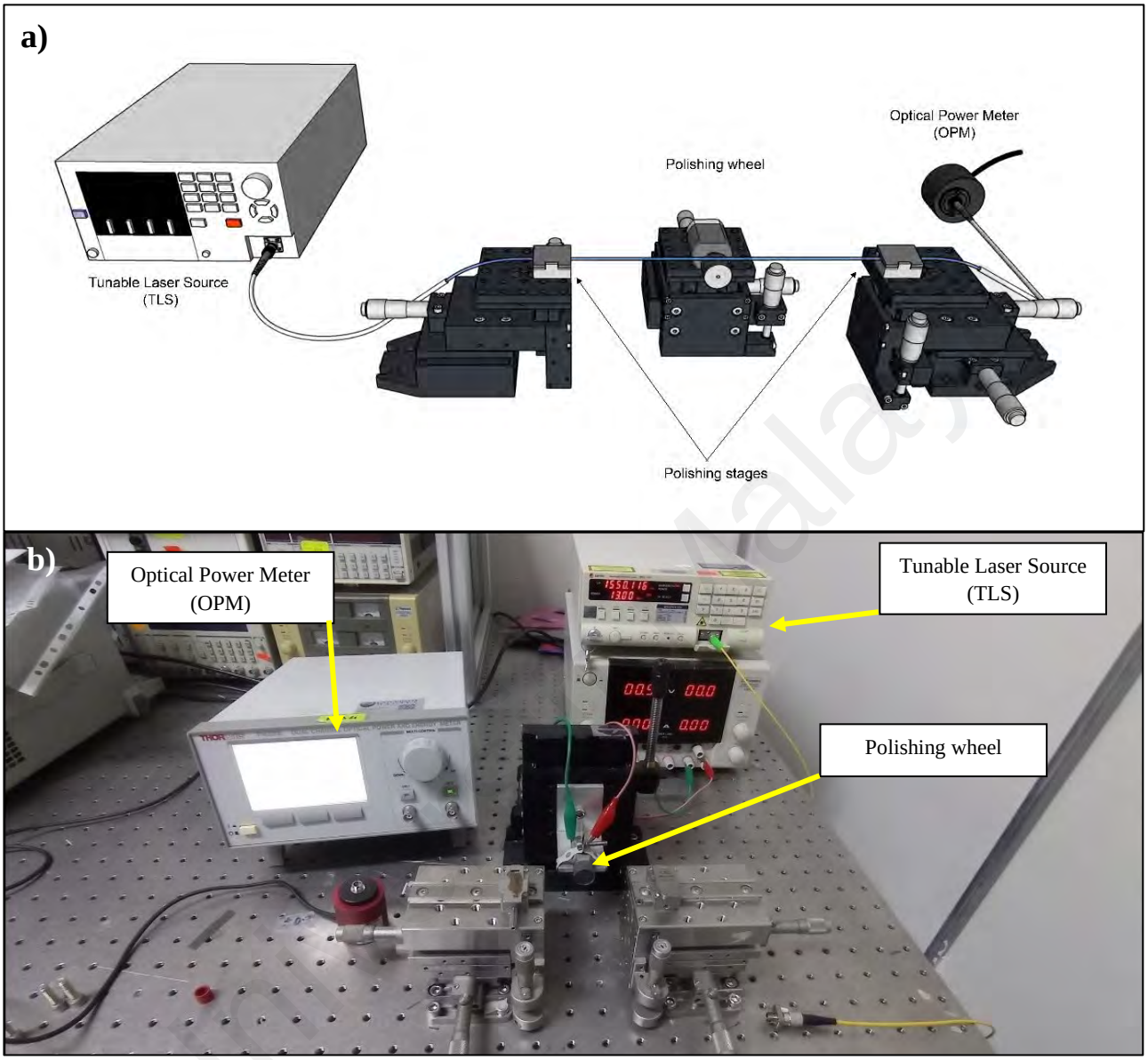

Figure 4.3: Arc-shaped fiber fabrication stage setup: (a) schematics (b) actual setup

The arc-shaped fiber fabrication is called “two-step” due to the change of polishing medium in the middle of the fabrication. This is crucial as the thulium-doped fluoride fiber is sensitive to scattering. Using only the 30 µm sandpaper, we found that it was impossible to achieve mode-locking in the TDFF laser cavity, making the two-step process crucial. Using the 1 µm grit size polishing film allows for a smoother surface finish on the arc-shaped fiber. However, the length of time it takes for the fine polishing film to achieve the desired 3.0 dB insertion loss from the initial fiber is impractical. As such, the first phase uses a larger grit size of 30 µm to polish the majority of the cladding. 2.8 dB loss for the first phase was chosen to allow the polishing film on the second phase to have enough material to shave off and end with a smooth finish without exceeding the final targeted insertion loss.

4.4 Preparation of MPX_3/arc-shaped fiber SA

2.5 µL of the exfoliated MPX_3 was then dropped onto the arc-shaped fiber, completing the MPX_3/arc-shaped fiber saturable absorber. This process is visualized in Figure 4.4. The SA device was allowed to dry for several minutes before being deployed in the laser cavity.

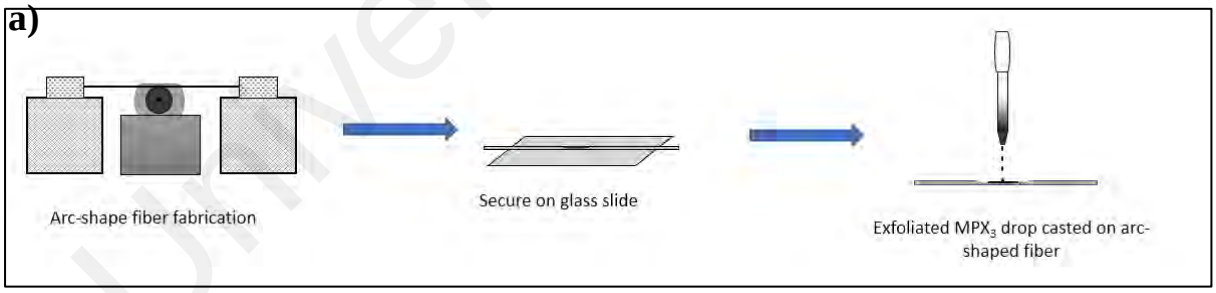

Figure 4.4: arc-shaped fiber fabrication process

4.5 Characterization of MPX_3/arc-shaped fiber SA

The completed SA was characterized to investigate its linear and nonlinear optical characteristics. This is crucial to understand the capabilities of the fabricated MPX_3/arc-shaped fiber SA for mode-locked pulse generation in thulium-doped fluoride fiber laser system.

Linear absorption test was conducted on the SA. White light source used was an SLS201L/M stabilized fiber-coupled light source obtained from ThorLabs. It is capable of emitting light in the wavelength range of 360 – 2600 nm. The light source was connected to the SA, which was then connected to a Yokogawa AQ6370C optical spectrum analyser (OSA). The setup is shown in Figure 4.5.

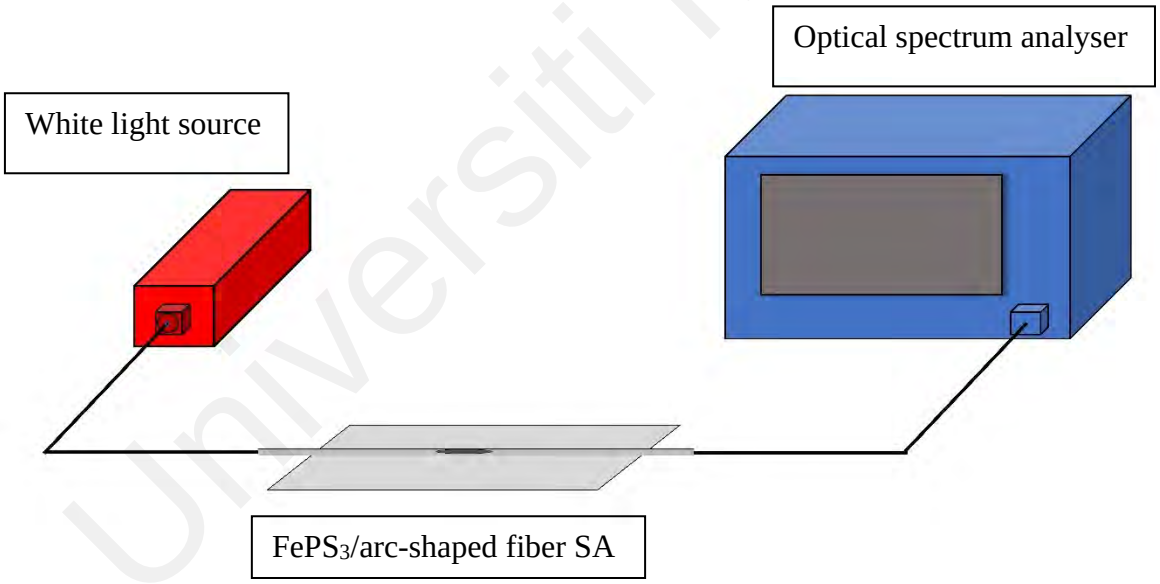

Figure 4.5: Linear absorption measurement setup

The method of choice to analyze the nonlinear properties of the SA is the two-detector measurement method. For this technique, a commercial mode-locked was used as a seed laser source. The ELMO Femtosecond Erbium mode-locked laser from Menlo systems was used for this task. It has a center wavelength of 1550 nm, with a pulse width, repetition rate and output power of 120 fs, 100 MHz and 10 mW respectively. These parameters results in a peak power intensity of ~3.2 GW/cm^2. This is then connected to a AQ2200-311 optical programmable attenuator from Yokogawa. The output of the attenuator was then connected to a 50/50 optical coupler. One end of the coupler was connected to a 1 m patch cord as a reference, while the other end was connected to the $FePS_3$/arc-shaped fiber SA, both of which are then connected to a ThorLabs S144C optical sensors connected to a ThorLabs PM320E Dual-Channel Power Meter. The setup is visualised in Figure 4.6.

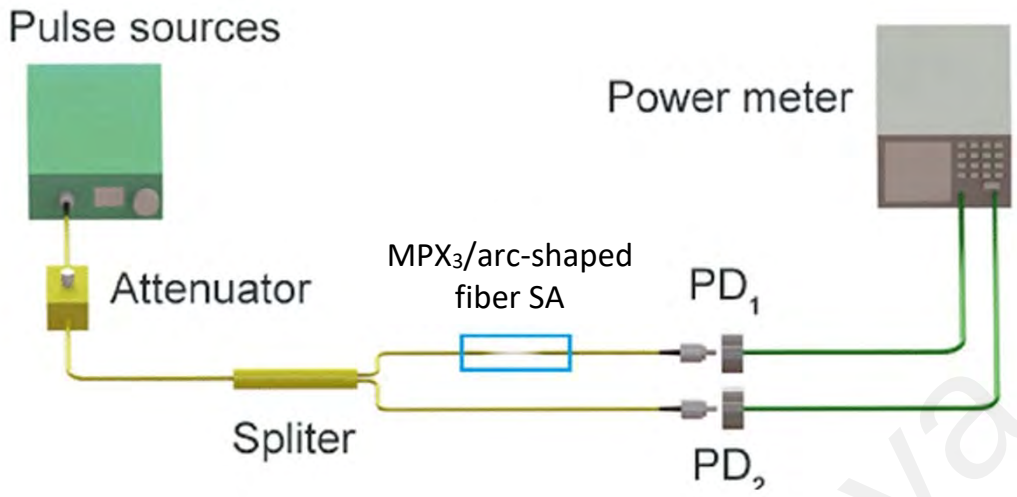

Figure 4.6: Two-detector measurement setup

The raw data will be fitted to the saturation model equation as shown below:

$$\alpha(I) = \frac{\alpha_s}{1 + \frac{I}{I_{sat}}} + \alpha_{ns} \qquad Equation\ 4.1$$

where α, α_s, α_{ns}, I, I_{sat}, are absorption, saturable absorption, non-saturable loss, input intensity, and saturable intensity respectively. Based on the fit, the modulation depth, saturation intensity and non-saturable absorption of each of the MPX_3/arc-shaped fiber SA can be determined.

CHAPTER 5: IRON PHOSPHORUS TRICHALCOGENIDE ($FEPS_3$)/ARC-SHAPED FIBER AS SATURABLE ABSORBER

5.1 Overview

This chapter presents the findings of TDFF mode-locked laser analysis using $FePS_3$/arc-shaped fiber as the SA. The chapter begins with the characterization results and discussion of the $FePS_3$/arc-shaped fiber SA including the material analysis and the optical analysis of the completed SA. Next, the SA was then inserted into the TDFF laser cavity for mode-locking operation and its output analysed. The analysis is separated into 5 portions: optical spectrum, pulse train, radio frequency, single-pulse width, and stability. These subchapters will focus on each results obtained and understand the characteristic of the TDFF mode-locked laser using $FePS_3$ SA.

5.2 $FePS_3$ preparation

5.2.1 $FePS_3$ liquid phase exfoliation (LPE) process

The liquid phase exfoliation (LPE) processed used on the $FePS_3$ material is similar to the one discussed in Chapter 4. The LPE was done with 100 mg of $FePS_3$ crystals in 10 mL of 99% isopropyl alcohol (IPA) to produce a solution of 10 mg/mL concentration. The sonication process was done in an 8-hour period. Centrifugation to separate the unexfoliated $FePS_3$ was done at 5k revolutions per minute (RPM) at 15 minutes. The supernatant was then used for the SA device. The exfoliated $FePS_3$ is shown in Figure 5.1.

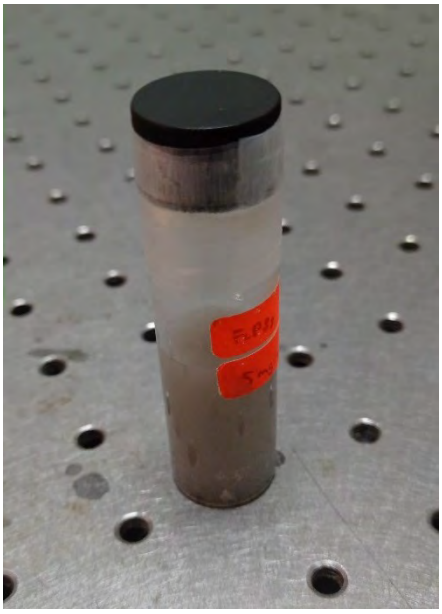

Figure 5.1: Exfoliated $FePS_3$

5.2.2 Characterization of exfoliated $FePS_3$

Multiple material characterizations were done on the exfoliated $FePS_3$ to understand its characteristics. One of them is X-ray diffractometry (XRD). It is commonly used to understand the atomic structures and crystallinity of a material. it can also be used to identify the elements and compounds present in a sample. XRD works by emitting x-ray towards a sample material. The material's crystalline structure will then diffract the incident beam into specific angles. Those diffracted beams also interfere with each other both constructively and destructively resulting in various intensities across various angles. By measuring this the angles and intensity of the diffracted beam, a material's chemical bond, crystallographic disorder and various other information can be obtained.

The XRD used in this study is a Malvern Panalytical Empyrean X-Ray Diffractometer. This machine is equipped with CuKα radiation, with setting of 40 mA at 45 kV. The resulting XRD for $FePS_3$ is shown in Figure 5.2. From the image, we can observe peaks at 2θ = 13.98°, 27.94°, 30.57°, 35.62°, 42.35°, 48.79°, 53.50°, 57.51°, and 73.86°. These sharp peaks signifies that the material possesses high crystallinity and purity. The peaks also correspond with a card set from the Joint Committee on Powder Diffraction (JCPDS) with a number 030-0663 and can be designated to planes (0 0 1), (0 0 2), (2 0 1), (1 3 1), (0 0 3), (3 1 0), (0 6 0), (0 0 4), and (4 4 2). High intensity observed at planes (0 0 1), (0 0 2), (1 3 1), (0 0 4) and (0 0 3) proves the high quality $FePS_3$ crystal structure (Ur Rehman et al., 2018b).

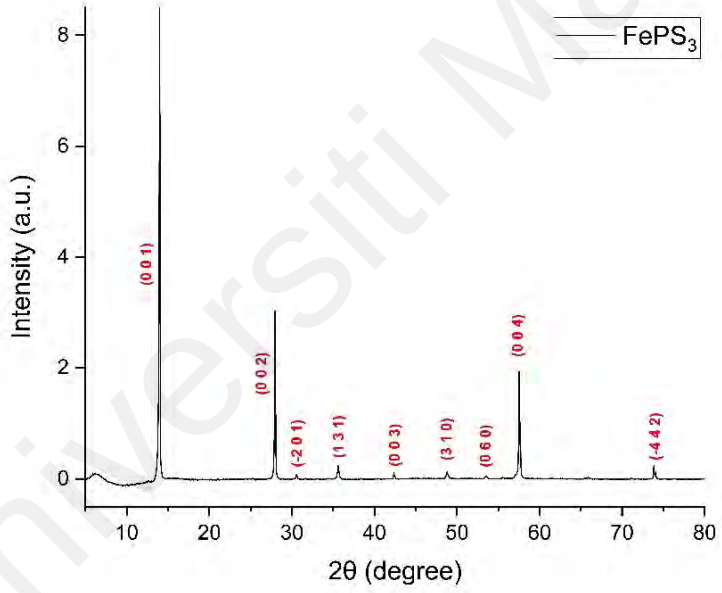

Figure 5.2: X-ray diffraction of $FePS_3$

FESEM or Field Emission Scanning Microscopy is used to investigate the topological structure of a material and its electronic properties. It uses a finely converged electron beam in

a vacuum as the source, which then hits the sample. It then takes advantage of the phenomenon of field electron emission resulting from different work function from various crystallographic planes to obtain an image on the detector. This is then presented as an enlarged image of the sample surface.

For the study of our exfoliated $FePS_3$, the FESEM machine used is a Hitachi SU8220. Resulting images are shown in Figure 5.3. Figure 5.3(a) shows the unexfoliated sample of $FePS_3$. It can be seen that the grain of $FePS_3$ was a result of multiple flakes of individual $FePS_3$ flakes stacked on itself. $FePS_3$ inherently forms 2D nanosheets. However, these nanosheets are held to each other by weak Van der Waals (VdW) forces, forming bulk crystals. These nanosheets can easily be delaminated using the LPE process. The result is as shown in Figure 5.3(b) where single layer $FePS_3$ can be seen. The LPE process have successfully delaminated the $FePS_3$ bulk crystals, resulting in individual layers showing smooth surface with lateral dimension approximately 8 µm.

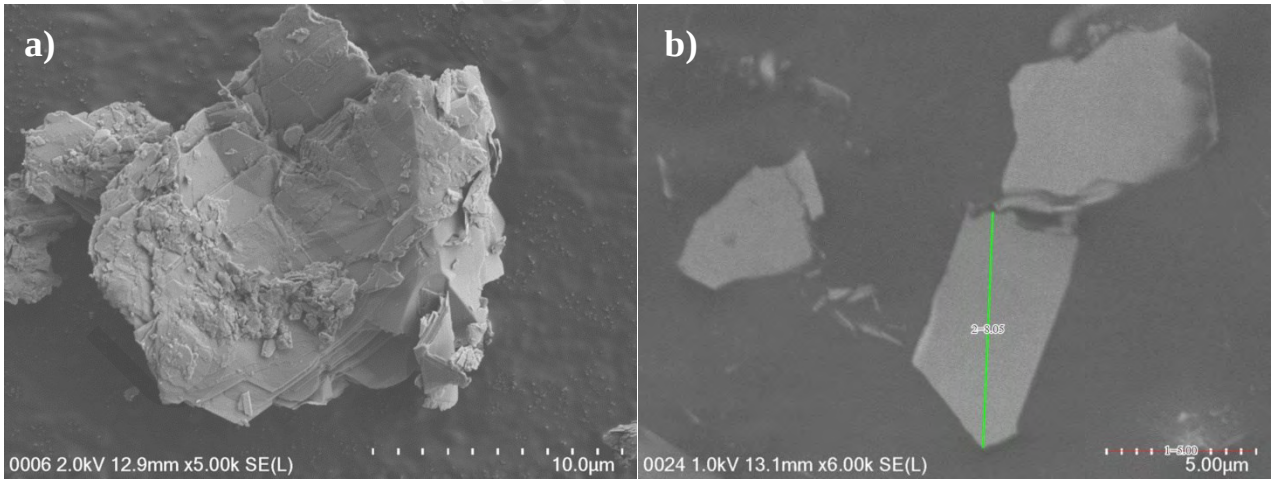

Figure 5.3: FESEM image of (a) bulk $FePS_3$ and (b) post-LPE $FePS_3$

The FESEM used in this study also included an Energy Dispersive X-ray (EDX) detector. EDX is commonly used in tandem with FESEM for elemental analysis or chemical characterization of a sample. It relies on the concept of ionization of atom. When an incident electron hits an atom of a sample, its orbital electron is ejected (ionized). The shell vacancy is then filled by an electron from an outer orbital. The excess energy of the transition is released in the form of X-ray. As the difference of energy between the two orbitals are unique to every elements, the resulting x-ray is also unique to the element. This is known as the characteristic x-ray and used to identify the elements present in a sample.

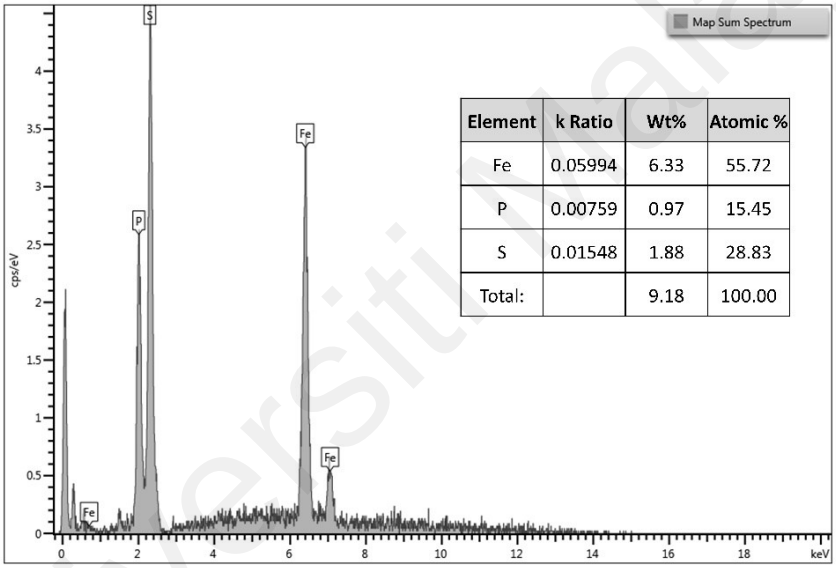

Element	k Ratio	Wt%	Atomic %
Fe	0.05994	6.33	55.72
P	0.00759	0.97	15.45
S	0.01548	1.88	28.83
Total:		9.18	100.00

Energy dispersive x-ray (EDX) spectrum for FePS3

Figure 5.4: $FePS_3$ EDX spectrum (inset: atomic and weight percentages)

EDX analysis was run on our $FePS_3$ sample using the same machine as the FESEM analysis. The resulting spectrum is shown in Figure 5.4. Several signal peaks can be seen which corresponds to the elements of $FePS_3$, which are Iron (Fe), Phosphorus (P) and Sulphur (S). The identified elements atomic and weight percentages are shown in the inset of Figure 3.4. It

can be assumed that the prepares $FePS_3$ sample was pure as there are no other elements detected from the EDX analysis.

Another tool of studying a material is the High-Resolution Transmission Electron Microscopy (HRTEM). HRTEM is a powerful equipment that allows imaging down to the atomic structures. Its high magnification capability allows us to study the properties of materials on atomic scale and understand its lattice structures and crystal grain patterns. In HRTEM, the electron beam is projected through a sample under vacuum conditions. The transmitted electron beam carries a variety of information on the sample. Interaction between the electron beam and the atoms of the sample results in elastically scattered electrons. There is also inelastically scattered electrons which is a result of the electron beam that loses part of its energy from interactions with the sample's atoms. These two along with the transmitted electron make up information that is presented as an image of the sample's internal structure.

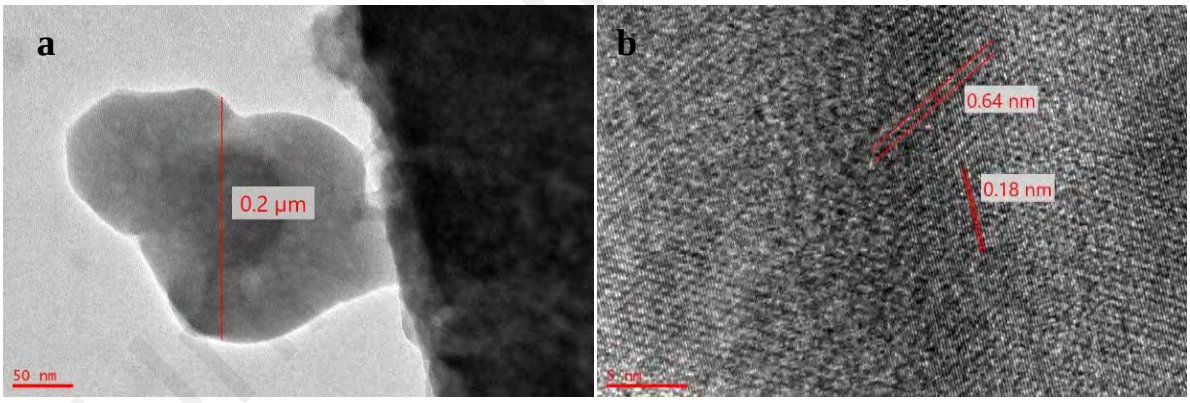

Figure 5.5: HRTEM images of $FePS_3$: (a) single layer (b) lattice structure

In this study, the HRTEM machine used is a JEOL JEM-2100F HRTEM with its accelerating voltage set at 200 kV to confirm the morphology of the processed $FePS_3$. The

HRTEM image is shown in Figure 5.5. Figure 5.5(a) shows a single layer $FePS_3$ 60k magnification. The observed flake was measured to be ~0.2 µm across. Increasing the magnification to 800k, we can see the lattice structure of the $FePS_3$ flake in Figure 5.5(b). Measuring the d-spacing resulted in values of ~0.64 nm and ~0.18 nm. Both these measurements can be assigned to planes (0 0 1) and (3 1 0) respectively, referring to the card number 030-0663 from the JCPDS and agrees with the XRD results obtained.

To further understand the topography of the $FePS_3$, we also employ a profilometer. A profilometer is a measuring instrument to quantify a roughness of a surface profile. In this case, we used the profilometer to understand the layering structure of few layers $FePS_3$ as a result from the LPE process. A cantilever is moved vertically in contact with the sample surface and moved cross the sample laterally at a specified vertical force across a specified distance. The height position of the cantilever will move in reaction to the surface variation of the sample. This reaction is quantified and displayed as the 2D map of the surface topography.

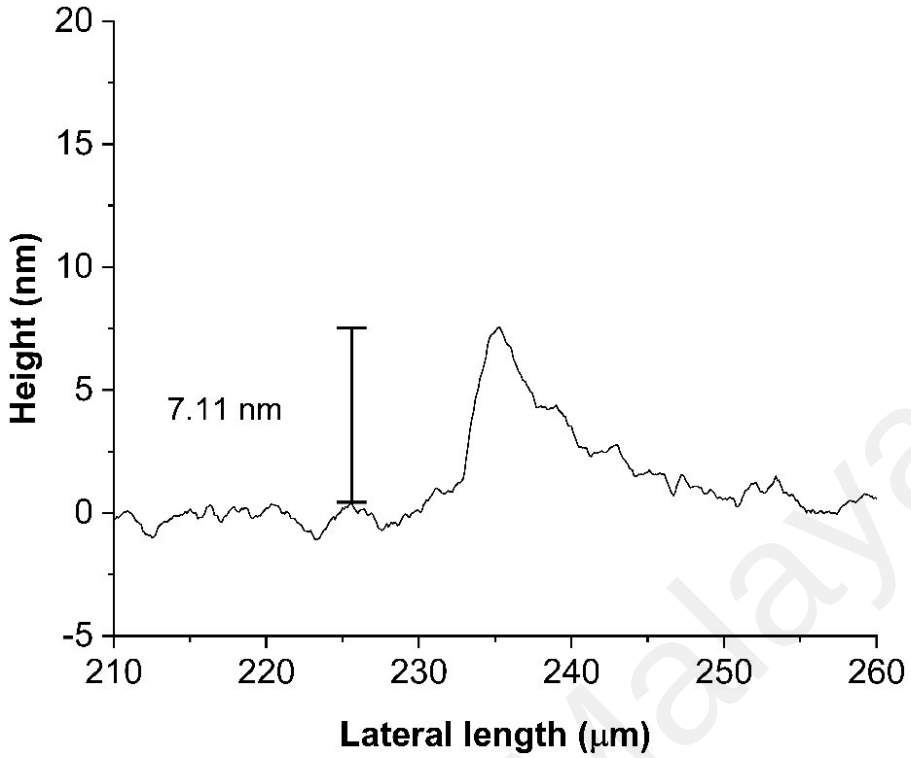

Figure 5.6: $FePS_3$ surface profile

In this work, we used a Veeco Dektak 150 surface Profilometer to understand the thickness of post-LPE $FePS_3$. Resulting graph is shown in Figure 5.6. It can be seen that the thickness of the $FePS_3$ nanoflakes was ~7.11 nm thick with a lateral length of ~5 μm. This suggest the presence of few layers $FePS_3$ in the solution used for the SA.

Considering the use of $FePS_3$ in this work is as an optical material, the optical characteristics of the $FePS_3$ was also studied. One method used is the UV-Visible-Near Infrared (UV-Vis-NIR) absorption spectroscopy. It measures the light intensity after passing through a sample (I) and compares it to the intensity of light before it passes through the sample (I_0). The ratio of I/I_0 is known as transmittance and expressed in form of percentage (%T). From this, the absorbance, A, can be calculated by the formula:

$$A = -\log\left(\frac{\%T}{100\%}\right) \qquad Equation\ 5.1$$

In the UV-Vis-NIR spectrometer, a beam of light source ranging from 200 nm to 2100 nm was split into two beams and shot into two clear cuvette; one containing pure solvent as reference while the second contains the post-LPE $FePS_3$ solution. The reference beam is taken as 0% absorbance baseline. Both beams then go into a detector which then determines the absorbance spectrum of the sample. The resulting spectrum can then be converted to a Tauc's plot to determine the samples band gap.

Our $FePS_3$ sample uses a Perkin Elmer Lambda 750 UV-Vis-NIR spectrometer to analyze its absorbance characteristics from 200 nm to 2100 nm wavelength of light. The resulting spectrum is then converted to its corresponding Tauc's plot to determine its optical band gap. These two results are shown in Figure 5.7. Figure 5.7(a) shows the UV-Vis-NIR spectra, and an absorption peak at 1960 nm was observed. The Tauc's plot shown in Figure 5.7(b) showed a bandgap of 2.3 eV, which agrees with previous report by Aruchamy et al. (Aruchamy et al., 1988) stating that $FePS_3$ have a bandgap between 1.62 to 2.3 eV.

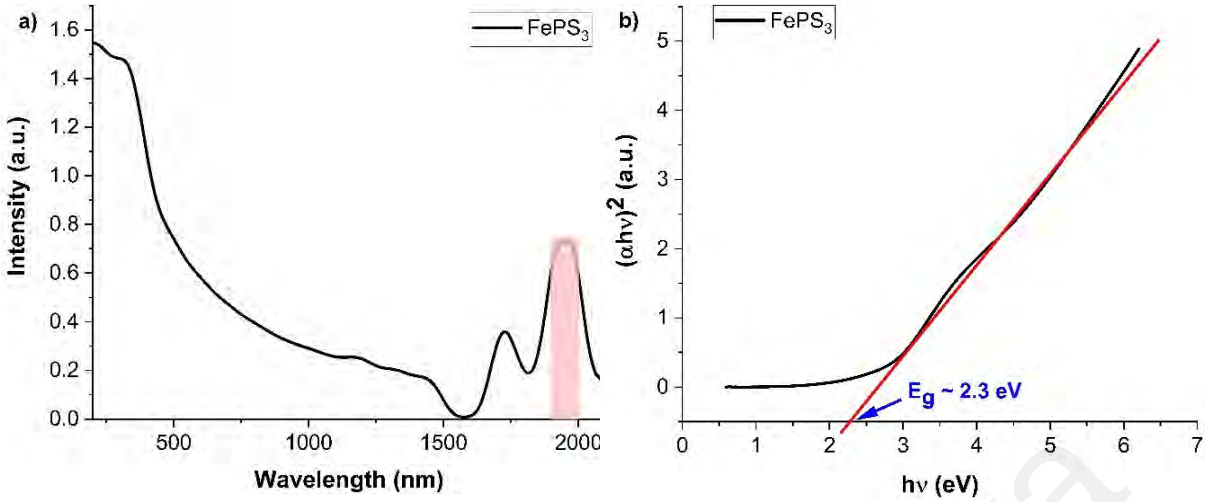

Figure 5.7: UV-Vis-NIR results: (a) UV-Vis-NIR absorption spectrum of $FePS_3$, (b) its corresponding Tauc's plot

Another optical analysis that was done on the $FePS_3$ is the Fourier Transform Infrared (FTIR) spectroscopy. Unlike other optical analysis method where a single monochromatic beam is used as the light source, FTIR shoots a broadband light with multiple frequencies simultaneously. The light then passes through a Michelson interferometer, which is a configuration of moving mirrors designed to periodically block and transmit the beam of light employing the concept of wave interference. Different wavelengths are modulated at different rates, resulting in different spectrum coming out of the interferometer at any given moment. The beam is then directed towards the sample. The amount of light absorbed by the sample is then measured. The beam is then modified to contain a different set of frequencies, resulting in a second data point. This process is repeated multiple times in rapid succession. The computer then analyses the raw data and uses Fourier transform algorithm to output the desired result.

Our FTIR analysis of the $FePS_3$ uses a Perkin Elmer FTIR-Spectrum 400 for identification of its chemical bonds. The FTIR was done from 400 cm^{-1} to 3500 cm^{-1} and is shown in Figure 5.8. A peak can be seen at 554 cm^{-1}, indicating the presence of asymmetric stretching of $(PS_3)^{2-}$

(El-Meligi et al., 2015). The peaks observed at 760 cm^{-1} and 952 cm^{-1} can be assigned to P-O asymmetric stretching vibrations (Jastrzębski et al., 2011). In addition, water molecules presence can be verified as there are peaks at 1438 cm^{-1} and 1611 cm^{-1} (Jastrzębski et al., 2011) including hydroxyl group with peaks at 2925 cm^{-1} and 3402 cm^{-1}, indicating (O-H) stretching vibrations (Chukanov & Chervonnyi, 2016). CO_2 presence in air was also detected with peak at 2283 cm^{-1} (Luna Zaragoza et al., 2009).

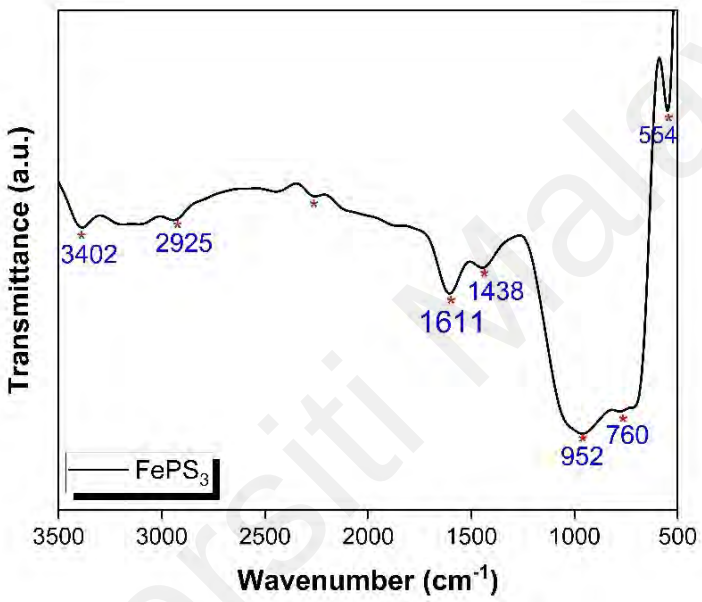

Figure 5.8: $FePS_3$ FTIR spectra

It is also crucial to analyze the stability of the $FePS_3$. One method to do this is by using the Thermogravimetric analysis (TGA). TGA analyses the change of mass of a sample over time as the temperature changes. This measurement can provide data of a material physical phenomena such as phase transition, thermal decomposition, and chemisorption among others. One application of TGA is analysis of thermal stability. If a material is thermally stable, there will be negligible or even no mass change. It can also indicate the maximum use temperature of a material, over which the material will begin to degrade.

In this study, the equipment used for TGA is a Perkin Elmer Pyris Diamond TGA. The resulting TGA curve is shown in Figure 5.9. From the graph, it can be seen that the $FePS_3$ possess a three-step weight loss process, with the first step from 30 °C to 255 °C followed by the second step between 255 °C to 506 °C and last step between 506 °C and 700 °C. The initial 1 % loss in the first step can be contributed to the vaporization of water content on the surfaces. Second step presents further sample dehydration with a <1 % loss of weight (Jastrzębski et al., 2011). The third step showed the maximum loss observed of approximately 6 %, indicating the decomposition of the $FePS_3$ (El-Meligi et al., 2015). The sample showed a total of 8% weight loss, indicating high thermal stability of the $FePS_3$.

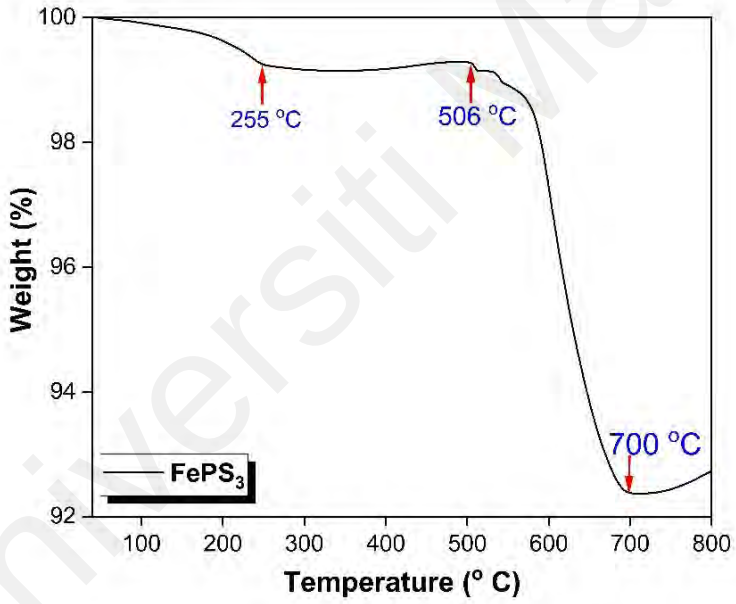

Figure 5.9: TGA curve of $FePS_3$

5.3 $FePS_3$/arc-shaped fiber

5.3.1 Two-step arc-shaped fiber fabrication (3.0 dB loss)

The arc-shaped fiber used in this chapter was fabricated in a similar method as discussed in Section 4.3 of Chapter 4. The targeted insertion loss of the arc-shaped fiber is 3.0 dB, with the first phase of polishing up to 2.8 dB and the remaining 0.2 dB completed at the second polishing phase. The resulting arc-shaped fiber is shown in Figure 5.10(a). 2.5 µL of the post-LPE $FePS_3$ solution was drop-casted on the arc, resulting in flakes on the fiber visible in Figure 5.10(b)

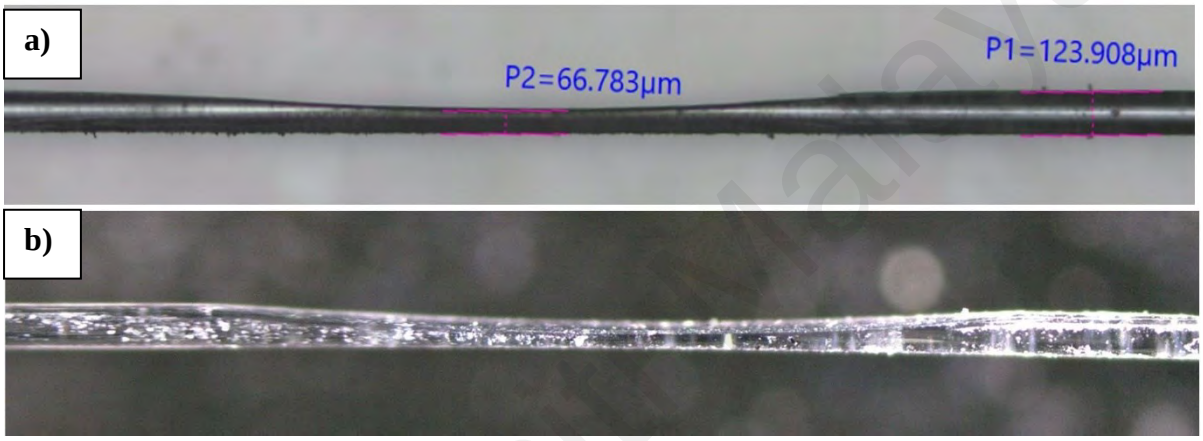

Figure 5.10: (a) arc-shaped fiber, (b) $FePS_3$ drop-casted on arc-shaped fiber

5.3.2 Characterization of $FePS_3$/arc-shaped fiber

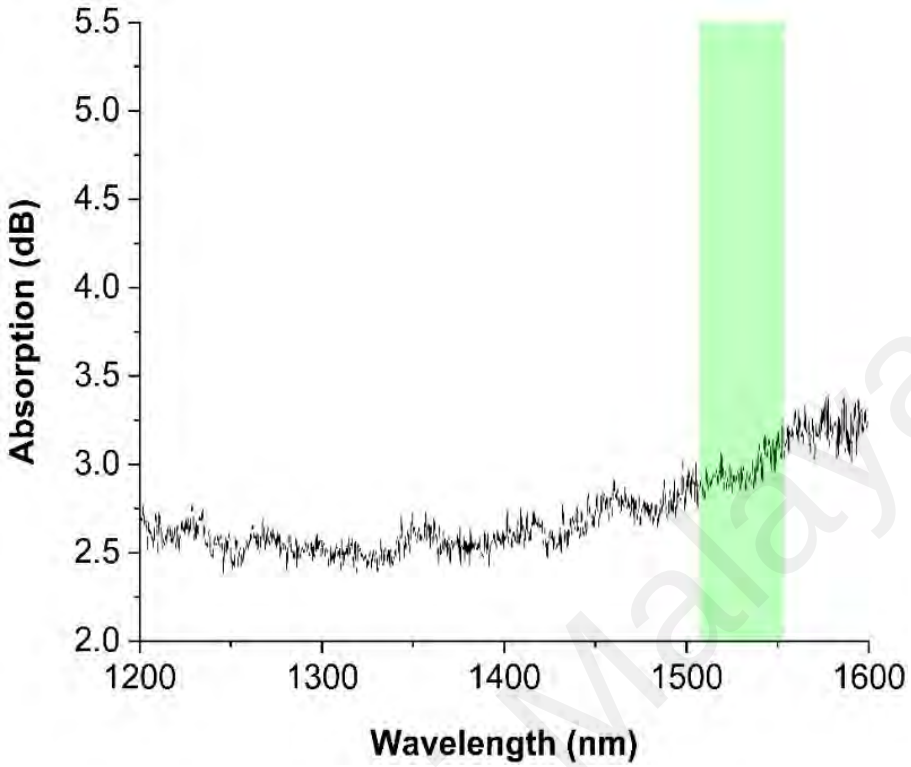

Figure 5.11: $FePS_3$/arc-shaped fiber SA linear absorption

The linear absorption analysis was done as discussed in Chapter 4 and the result for $FePS_3$/arc-shaped fiber was taken over the range of 1200 – 1660 nm and shown in Figure 5.11. It can be seen that the SA showed a linear absorption approximately 2.5 dB at 1200 nm. Highlighted in green is the S-band region, in which the SA have a linear absorption of around 2.5 to 3.1 dB. According to Set et al. and Chiu et al., this value is optimum for the generation of mode-locked pulses (Chiu et al., 2010; Set et al., 2004). Beyond the 1520 nm wavelength, the SA exhibited absorption of above 3.1 dB, which is more favourable in Q-switched pulse generation.

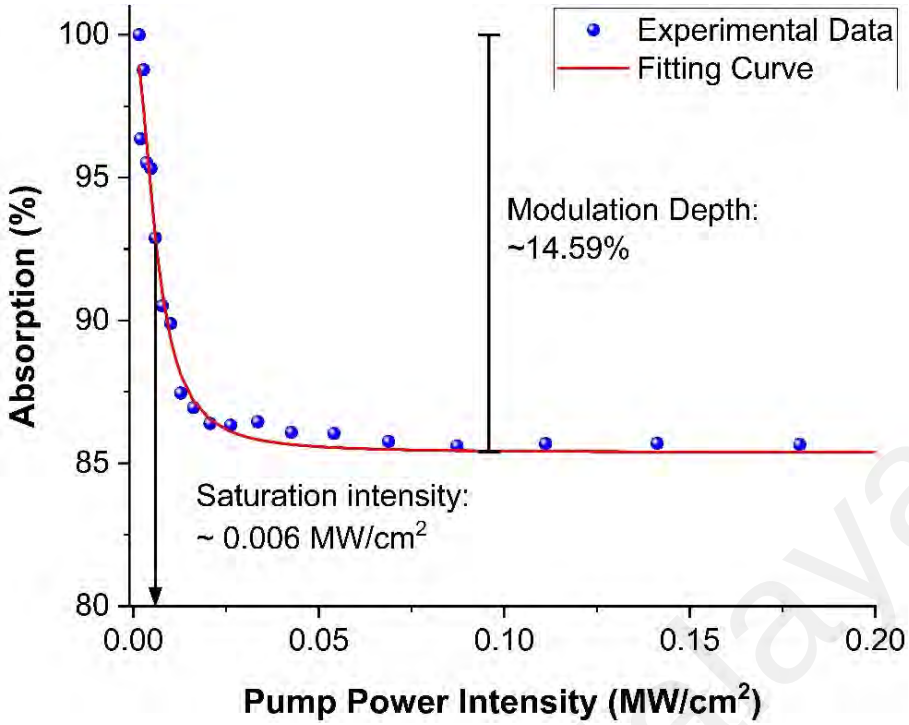

Figure 5.12: Nonlinear characteristic of $FePS_3$/arc-shaped fiber SA

Nonlinear optical properties was investigated using the setup discussed in Chapter 4. The raw data was obtained and fitted to the saturation model equation as shown in Figure 5.12. The result showed a modulation depth of 14.59 % for the $FePS_3$/arc-shaped fiber SA. Its saturation intensity and non-saturable absorption was determined to be 0.006 MW/cm^2 and 85.41% respectively.

5.4 Characterization of S-band mode-locked thulium-doped fluoride fiber using $FePS_3$ as saturable absorber

The $FePS_3$/arc-shaped fiber was introduced into the TDFF laser cavity system as shown in Chapter 3. Mode-locking was achieved at 280 mW pump power, with minor polarization adjustments. The pump power was maintained throughout the experiment for ideal laser

stability. All reading such as optical spectrum, frequency analysis, pulse train and many more were taken under the sustained pump power. There were no pulse observed when the SA was removed from the cavity, indicating that the mode-locked pulses were generated by the SA.

The resulting spectrum can be observed in Figure 5.13. From the graph, it can be seen that the peak wavelength is 1504.8 nm. The spectral bandwidth or also known as the 3-dB bandwidth can be measured to be 0.704 nm. The spectrum shows Kelly's sidebands, indication of anomalous net dispersion of the system and the operation of laser is in the soliton regime.

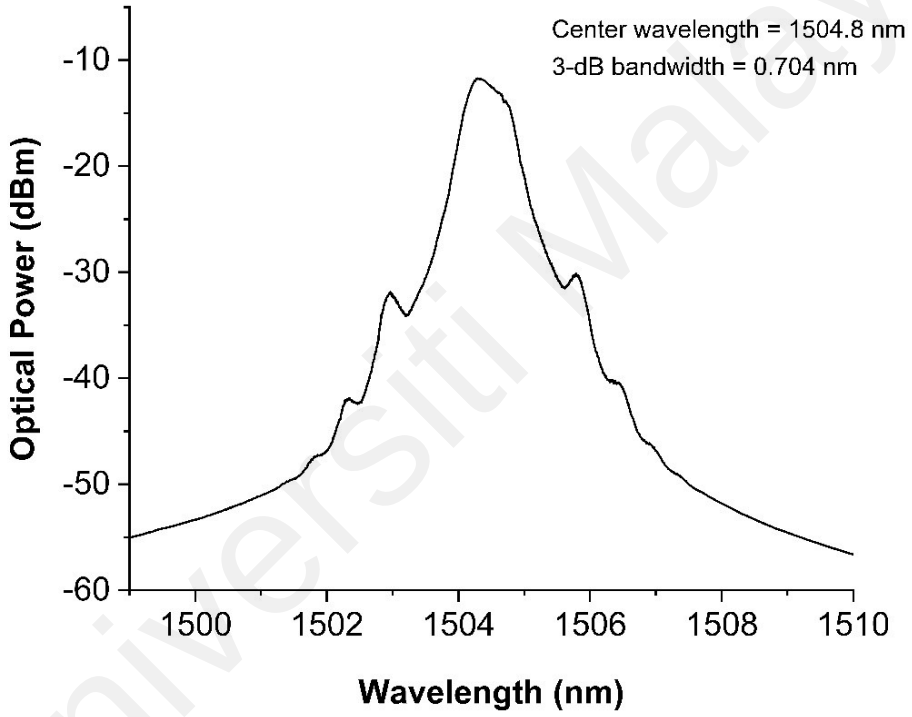

Figure 5.13: Optical spectrum of $FePS_3$-based mode-locked laser

The central wavelength can be tuned using a tunable bandpass filter or known as TBPF. This was not done in this study as the bandwidth limitation of the TBPF would result in a broader pulse width as it would filter the optical spectrum.

For this study, the pulse train was obtained using a DSOX 3102 T InfinitiVision oscilloscope from Keysight. A DET08 CFC/M photodetector from ThorLabs was used to convert output light signal from the laser cavity into electrical signals for the oscilloscope. The resulting pulse train is as depicted in Figure 5.14. It can be seen that the pulse spacing is constant at 2.49 µs every pulse. Inversing this value result is a repetition rate value of 400.6 kHz. This corresponds to the round-trip time taken for light to travel the length of the laser cavity, which is 525 m. This can be related by the following formula:

$$Repetition\ rate = \frac{C}{Ln} \qquad \text{Equation 5.1}$$

where C, L and n identifies as light speed, length of cavity and refractive index of travel medium, and results in the unit Hertz (Hz). The laser's repetition rate also remained constant at all pump power levels. These results further prove that the laser is in mode-locking operation.

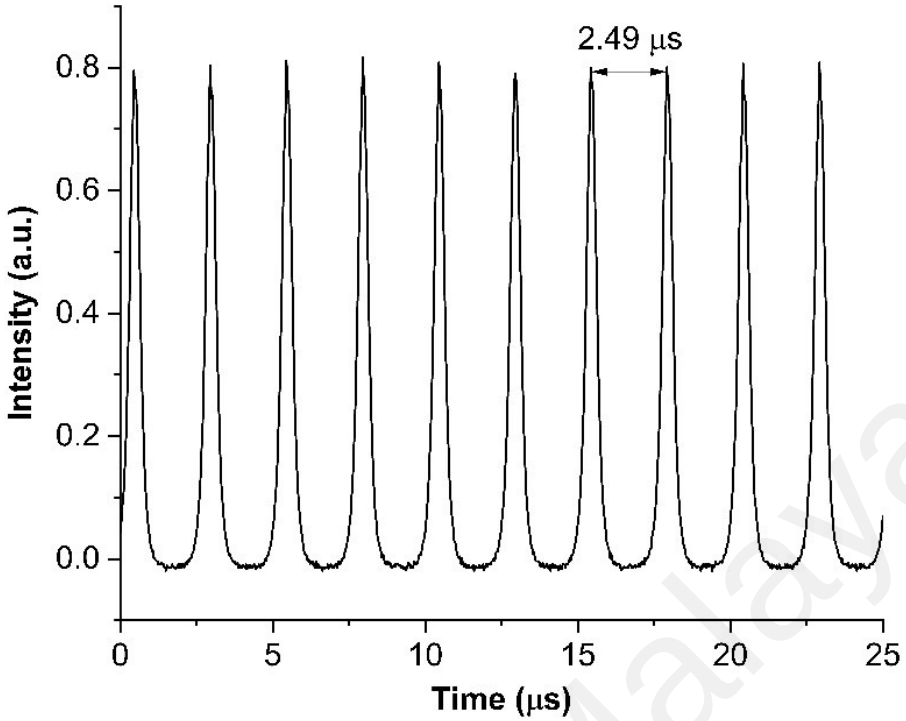

Figure 5.14: Pulse train analysis of $FePS_3$-based mode-locked laser

The output of the mode-locked laser is analyzed using an FPC 1000 RFSA from Rohde & Schwarz. The resulting RF spectrum is as shown in Figure 5.15. The reading was taken at a resolution bandwidth (RBW) of 1 kHz to ensure the optimal signal can be obtained as the mode-locked pulses have ultrashort signal duration. The signal peaks at a center frequency of 400.6 kHz, corresponding to the findings on the oscilloscope. The laser showed a ~45 dB SNR, signifying the $FePS_3$-based mode-locked TDFF system is highly stable.

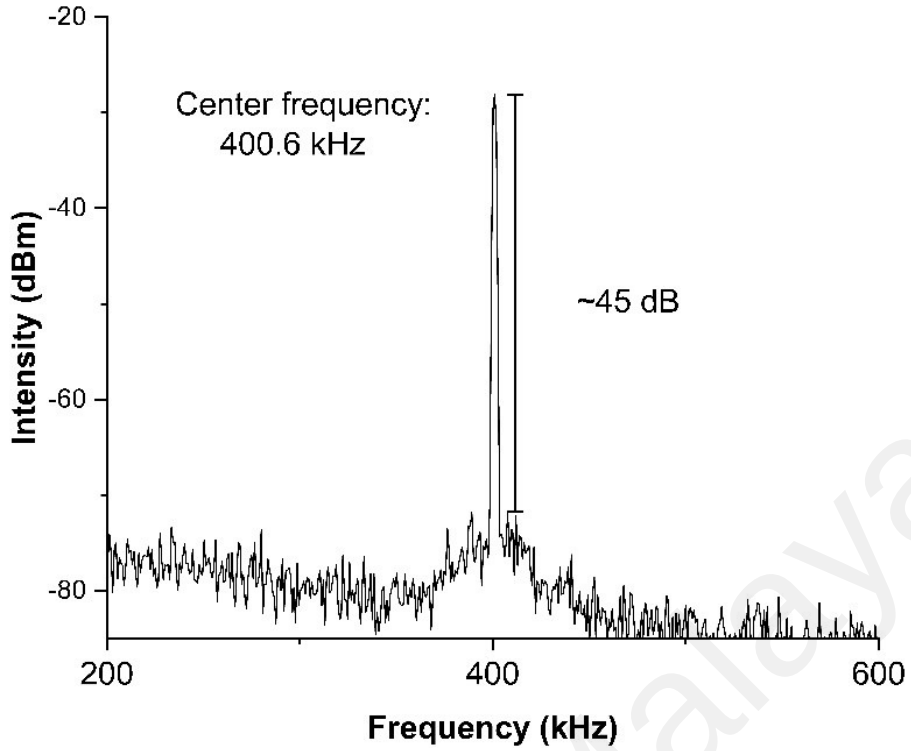

Figure 5.15: Radio frequency spectrum of $FePS_3$-based mode-locked laser

Pulse width of the TDFF mode-locked laser is measured using an Alnair Labs 1.5 µm autocorrelator (model no. HAC-200). The obtained results are as shown in Figure 5.16. The FWHM of the autocorrelation trace measured 6.02 ps. After including the $sech^2$ deconvolution factor of 0.648, the pulse width was determined to be 3.90 ps. The TBP was calculated to be 0.363 after including the center wavelength and spectral width of 1504.8 nm and 0.704 nm respectively. Considering a $sech^2$ transform limited pulse theoretical TBP value to be 0.315, our larger TBP value signifies that the $FePS_3$-based TDFF mode-locked pulse was slightly chirped.

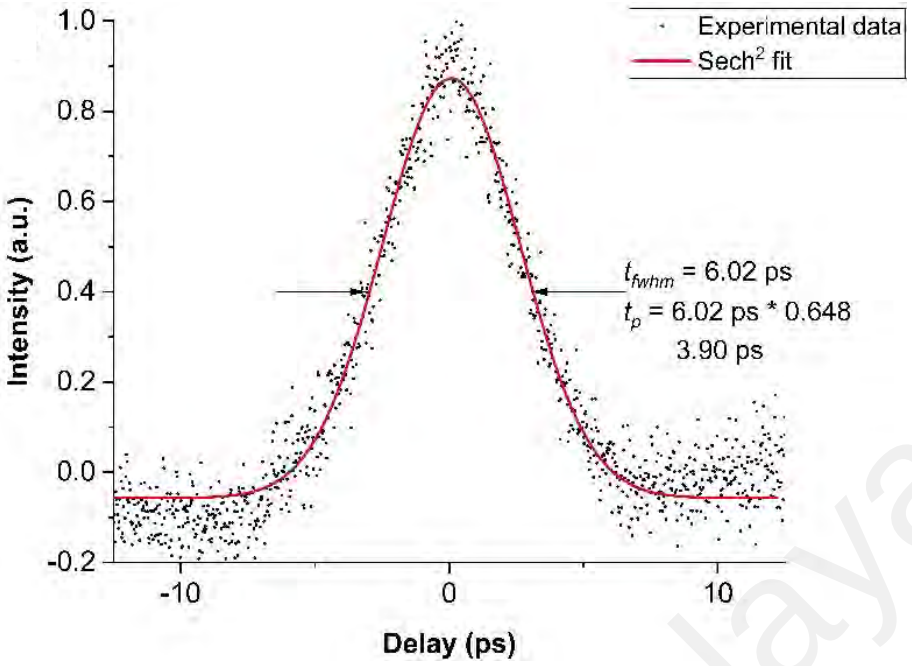

Figure 5.16: Autocorrelator trace with its sech^2 fit $FePS_3$-based mode-locked laser

To ensure that the TDFF/$FePS_3$-SA mode-locked laser is stable over long operational duration, a long-term stability test was conducted over the course of three hours. Pump power was set at a constant 280 mW. A sample of optical spectrum was taken every 30 minutes. The resulting graph is displayed in Figure 5.17, with Figure 5.17(a) showing the 3D plot and Figure 5.17(b) showing the contour plot. Both figures showed central wavelength drift of less than 0.1 nm and power fluctuations of less than 0.01 dB. both these results proves the high stability of the generated mode-locked pulses. The experiment was also repeated and conducted over a longer period of time, with similar observations, further demonstrating the systems outstanding repeatability and stability for mode-locking.

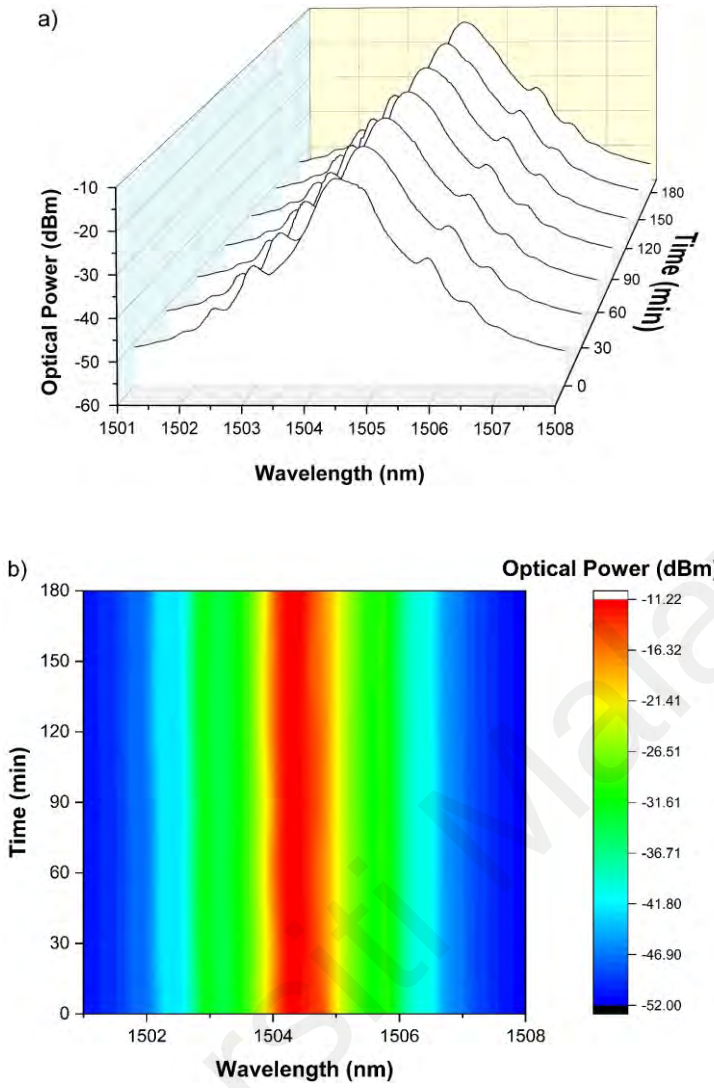

Figure 5.17: Stability test of $FePS_3$-based mode-locked TDFF laser: (a) 3D graph plot, (b) contour plot

The graph showing the relationship between the $FePS_3$-based mode-locked TDFF laser's output power and the applied pump power is shown in Figure 5.18. It can be seen that as pump power increases between 190.9 to 280 mW, the output power also increases between 1.38 to 3.01 mW. This relationship is linear, with the slope of the graph representing efficiency which is 1.8 %. At maximum pump power of 280 mW, the laser remained stable and output power remained constant at 3.01 mW. Calculations showed the laser output had a maximum pulse energy of 7.5 nJ at peak power of 1.9 kW when measured at the 10 % output port of the OC.

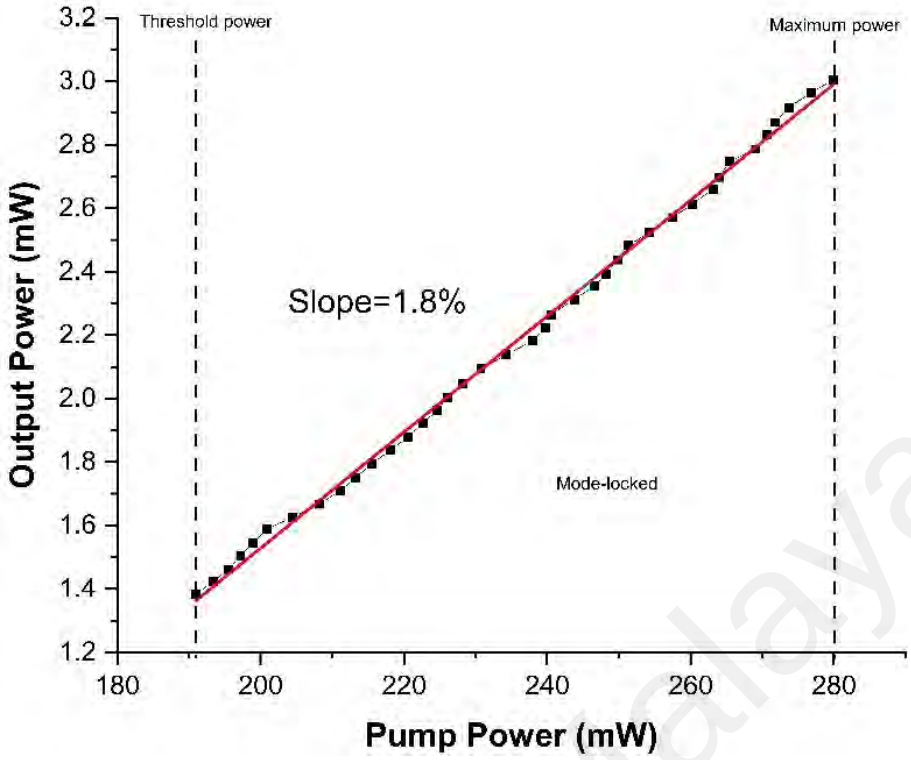

Figure 5.18: Relationship between output power and pump power of $FePS_3$-based TDFF mode-locked laser

With average output power at the 10 % output port measuring 3.01 mW, the intracavity average power is determined to be 30.1 mW, with its corresponding peak power and pulse energy calculated to be 19.3 kW and 7.5 nJ respectively. Intracavity peak power intensity is calculated using the formula:

$$P_P = \frac{P_{AV}}{f_R \cdot t_P} \qquad Equation\ 5.2$$

Where P_P is peak power intensity, P_{AV} is average power, f_R is the repetition rate, and t_P is the pulse width. As provided by the manufacturer, core size of SMF-28 fiber used in the cavity is 9 µm, the intracavity peak power intensity was determined to be 59.5 GW/cm^2. Mode-locking was sustained up to maximum pump power of 280 mW without any observable SA degradation. This can be concluded that the SA possesses a damage threshold of higher than

59.5 GW/cm^2. There was no Q-switching of the laser observed as the intracavity power is too high for Q-switching. For Q-switching to occur, the $FePS_3$ SA would need to be fabricated into a thin film, which would result in a higher saturable loss, more favorable for Q-switching.

CHAPTER 6: MANGANESE PHOSPHORUS TRICHALCOGENIDE ($MNPS_3$)/ARC-SHAPED FIBER AS SATURABLE ABSORBER

6.1 Overview

In this chapter, the use of Manganese Phosphorus Trichalcogenide ($MnPS_3$) as a saturable absorber for S-band thulium-doped fluoride fiber laser is investigated. This chapter starts with the material characterization and optical analysis of the $MnPS_3$/arc-shaped fiber SA. The liquid phase exfoliation process are adjusted to enhance the dispersion of $MnPS_3$ nanoflakes in the solution. The SA device is then introduced into the TDFF laser cavity system to produce mode-locked pulses. The mode-locked output was then studied and analysed in this chapter.

In this chapter, we attempt to increase the repetition rate of the mode-locked pulse. This was done by reducing the SMF-28 spool length as shown in Chapter 3, from 500 m to 300 m. The configuration of components in the cavity remained the same. The insertion loss of the arc-shaped fiber was also reduced from 3.0 dB to 2.5 dB in an attempt to reduce the scattering loss while still maintaining sufficient evanescent field interaction between the laser and the $MnPS_3$ material.

6.2 $MnPS_3$ preparation

6.2.1 $MnPS_3$ liquid phase exfoliation (LPE) process

The $MnPS_3$ is received in a crystal form and underwent the similar liquid phase exfoliation process as discussed in Chapter 4. However, it was found that the ideal solvent to properly disperse the $MnPS_3$ nanoflakes was a chemical called NMP (N-Methyl-2-Pyrrolidone). Other than the solvent, all other steps are according to as shown in Chapter 4. 100 mg of $MnPS_3$ crystals were dispersed in 10 mL of NMP to produce a solution of 10 mg/mL concentration,

which was then water bath-sonicated for 8 hours before centrifuged at 5000 rpm for 15 minutes. The resulting centrifuged solution decanted to remove unexfoliated $MnPS_3$ before being used. The resulting $MnPS_3$ solution is as shown in Figure 6.1

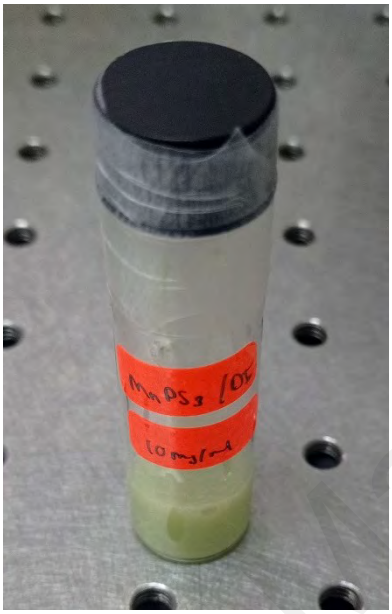

Figure 6.1: Exfoliated $MnPS_3$

6.2.2 Characterization of exfoliated $MnPS_3$

The $MnPS_3$ was subjected to several material characterizations in order to better understand its properties. The X-ray diffractometry is one of them (XRD). It is regularly utilized to properly understand the atomic composition and crystallinity of a substance. It could also be employed to determine which substances and components are found in a sample. Emitting x-rays at a sample material is how XRD operates. The incident beam will then diffract into certain angles due to the material's crystalline structure. These diffracted beams also interfere with one another in both constructive and destructive ways, producing a range of intensities at different angles. This measurement may be used to determine the angles and intensity of the diffracted

beam, a material's chemical bond, the disorder of its crystal structure, and several other information.

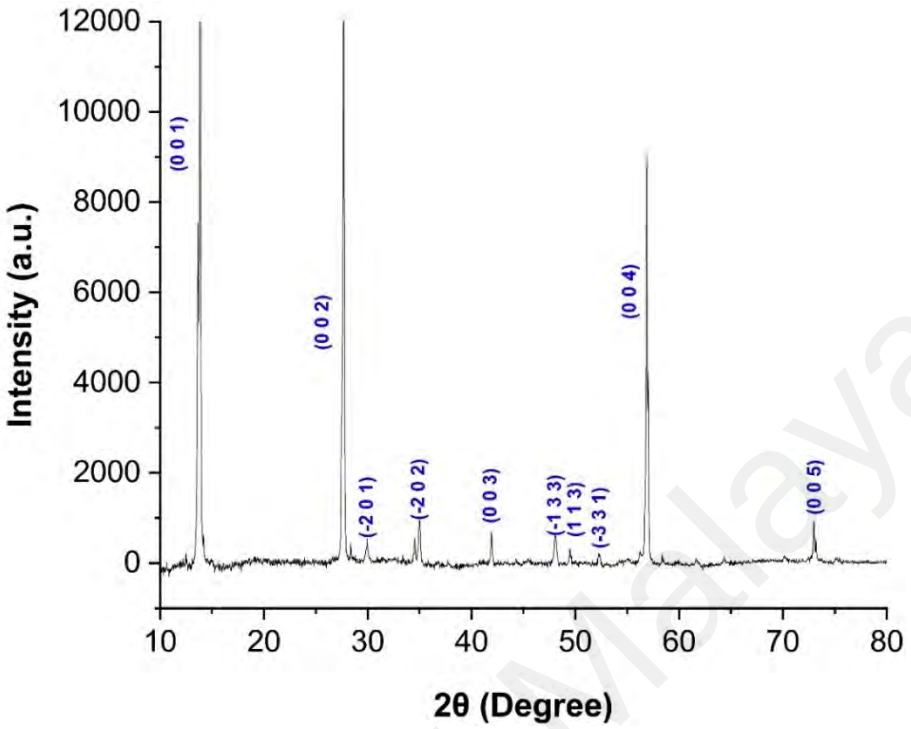

Figure 6.2: $MnPS_3$ XRD spectrum

To confirm the purity and crystallinity of the $MnPS_3$ crystals, a sample was sent for X-ray diffractometry (XRD) analysis prior to LPE process. It was done on an Empyrean XRD machine from Malvern Panalytical and was outfitted with a CuKα radiation source at 45 kV and 40 mA. The resulting spectrum is shown in Figure 6.2. From the image, it can be seen that there are distinct peaks at 2θ = 13.64°, 24.48°, 29.74°, 34.79°, 41.74°, 47.86°, 49.93°, 52.09°, 56.72°, and 72.85°. All these peaks are matched to a card set standard from the JCPDS or the Joint Committee on Powder Diffraction, which shows those peaks can be assigned to planes (0 0 1), (0 0 2), (-2 0 1), (-2 0 2), (0 0 3), (-1 3 3), (1 1 3), (-3 3 1), (0 0 4), (0 0 5). The sharp peaks signifies the high crystallinity and purity of the $MnPS_3$ crystal. According to Rehman *et al.*, the

intense peaks that represent the planes (0 0 2), (0 0 4) and (0 0 1) proves the high-quality crystalline structure of the $MnPS_3$. (Ur Rehman et al., 2018a).

FESEM, also known as field emission scanning microscopy, is used to examine a material's topological structure and electronic characteristics. The source is an electron beam that has been precisely focused in a vacuum, after which it strikes the sample. Then, in order to produce a picture on the detector, it makes use of the phenomena of field electron emission coming from various crystallographic planes' work functions. The sample surface is then shown in greater detail in the display.

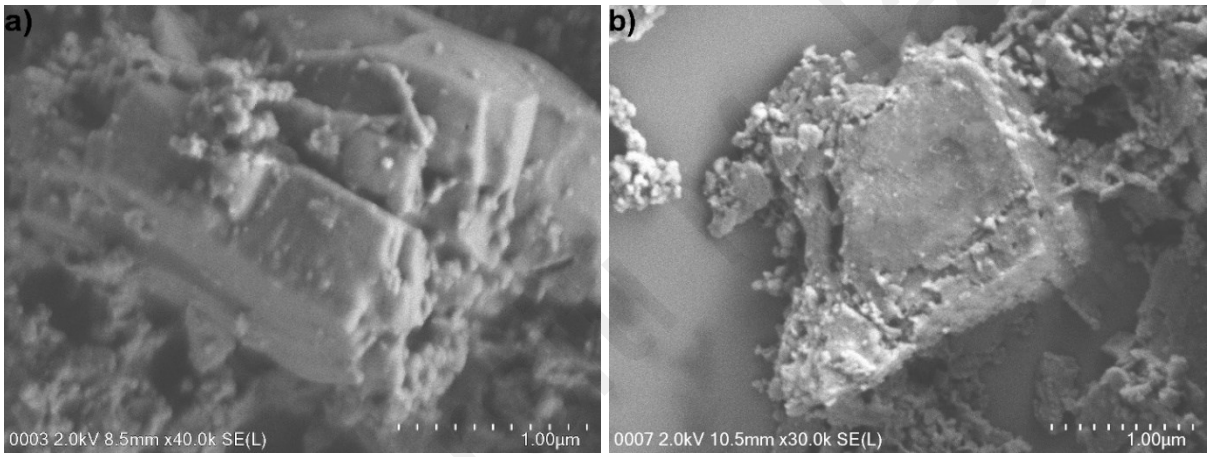

Figure 6.3: $MnPS_3$ FESEM image in (a) bulk form and (b) exfoliated

Both the $MnPS_3$ crystal and post-LPE were studied under a FESEM to analyze its surface morphology and to confirm the success of the LPE process in exfoliating the bulk $MnPS_3$. The FESEM used was a SU8220 FESEM from Hitachi. The images captured for both bulk and exfoliated forms are shown in Figure 6.3. Figure 6.3(a) shows the bulk $MnPS_3$ crystals. It can be seen in the image that the crystals are formed by stacked layers of $MnPS_3$ nanoflakes. These flakes are held together by the weak Van de Waals force. These are simply separated by the sonication procedure in the LPE process, as shown in Figure 6.3(b). The image shows few-

layer configuration of the $MnPS_3$, indicating the success of the LPE process. The layers shown in the image are surrounded by the unevaporated NMP solvent. This is due to the slightly high vaporization temperature of the NMP.

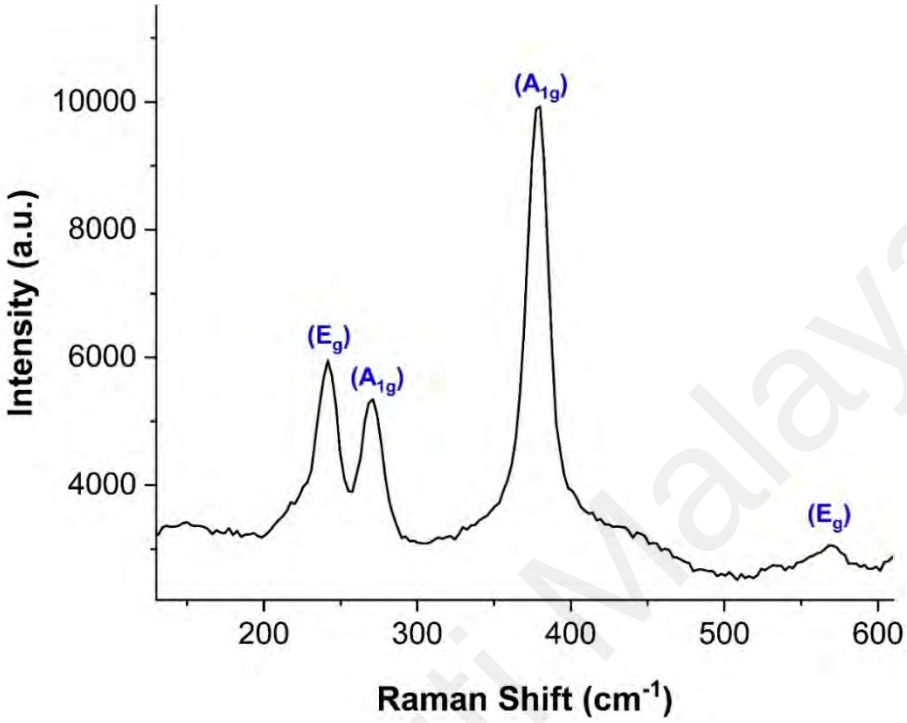

Figure 6.4: $MnPS_3$ Raman spectrum

The post-LPE $MnPS_3$ also underwent Raman spectroscopy analysis to understand its absorption mechanics and excitation states. The analytical machine used for this analysis is the InVia Raman microscope from Renishaw. It has an excitation wavelength of 514 nm. The resulting Raman spectrum is shown in Figure 6.4. From this image, we can see peaks at 241.7 cm^{-1}, 271.1 cm^{-1}, 379.9 cm^{-1}, and 568.0 cm^{-1}. The E_g vibration modes can be proven by the peaks at 241.7 cm^{-1} and 568.0 cm^{-1}, while the A_{1g} vibrational modes can be assigned to peaks 271.1 cm^{-1} and 379.9 cm^{-1} (Ur Rehman et al., 2018a).

6.3 MnPS3/arc-shaped fiber

6.3.1 Two-step arc-shaped fiber fabrication (2.5 dB loss)

Fabrication of the arc-shaped fiber is similar to the method discussed in Chapter 4, with the exception of the target insertion loss. For $MnPS_3$, the targeted insertion loss of the arc-shaped fiber was reduced from 3.0 dB to 2.5 dB in an attempt to reduce the scattering loss of the arc-shaped fiber while still maintaining sufficient evanescent field interaction between the laser beam within the fiber and the $MnPS_3$ nanoflakes on the arc-shaped fiber.

The first phase of polishing using the 30 µm grit sandpaper was done until the insertion loss achieves 2.3 dB, while the second phase using 1 µm grit polishing film was done until the total insertion loss achieves 2.5 dB, completing the arc-shaped fiber. The completed arc-shaped fiber was then drop-casted with ~2.5 µL of the $MnPS_3$ solution. Figure 6.5(a) shows the arc-shaped fiber while Figure 6.5(b) shows the completed SA with the $MnPS_3$ nanoflakes visible on the fiber.

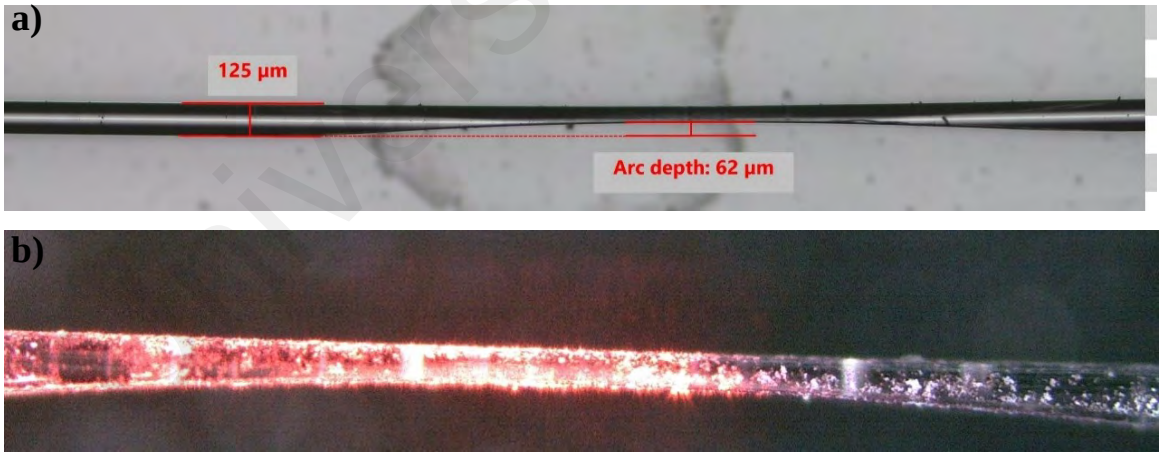

Figure 6.5: (a) 2.5 dB loss arc-shaped fiber (b) $MnPS_3$ coated arc-shaped fiber

6.3.2 Characterization of $MnPS_3$/arc-shaped fiber

The nonlinear properties of the fabricated $MnPS_3$/arc-shaped fiber saturable absorber was investigated using the twin detector measurement setup as discussed in Chapter 4. The raw data obtained was fitted to the saturation model equation and presented in Figure 6.6. From the graph, it can be seen that the SA device have a modulation depth of 25.63 %. The saturation intensity and non-saturable absorption was determined to be 0.002 MW/cm^2 and 74.37 % respectively.

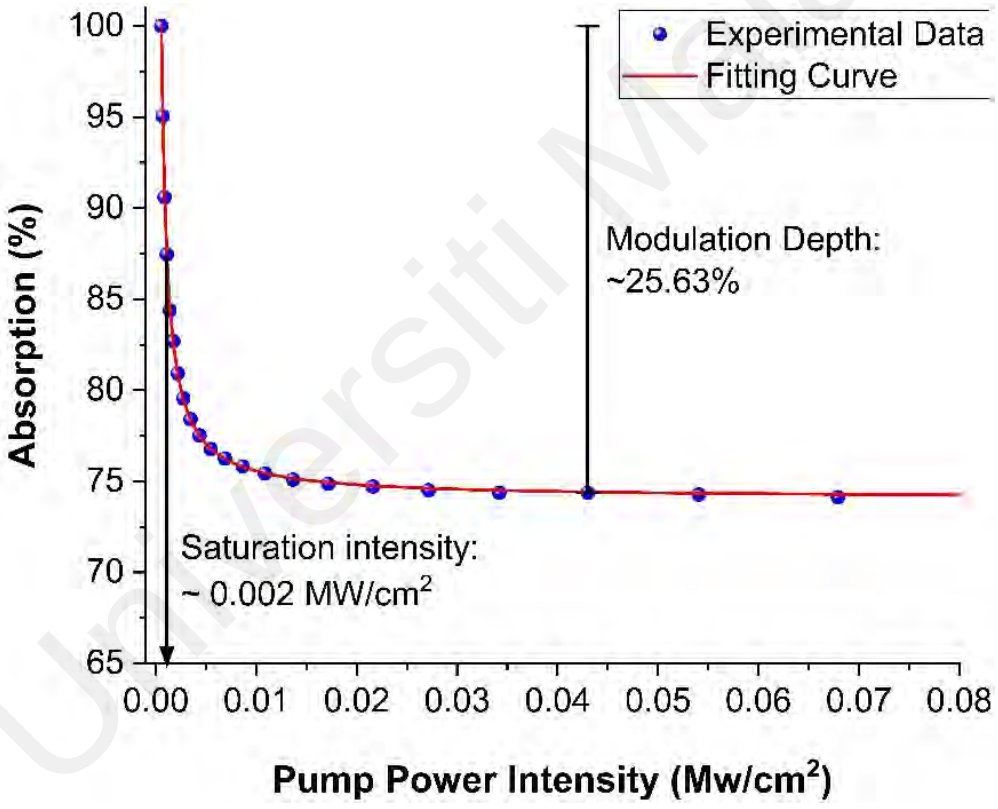

Figure 6.6: Nonlinear characteristics of $MnPS_3$/arc-shaped fiber SA

6.4 Characterization of S-band mode-locked thulium-doped fluoride fiber using $MnPS_3$ as saturable absorber

The fabricated $MnPS_3$/arc-shaped fiber SA was inserted into the TDFF laser cavity system as shown in Chapter 3. The configurations are similar, apart from the length of the SMF-28 spool, which was reduced from 500 m to 300 m. This was done in order to increase the mode-locked pulses repetition rate by reducing the laser roundtrip time. This resulted in a shorter total cavity length of 325 m. Since only the total length of SMF-28 was changed, group velocity dispersion will be calculated using similar material dispersion and center wavelength values as mentioned in Section 3.2.6. Using Equation 3.1, the new net cavity dispersion was calculated to be -5.3 ps^2. Measurements were taken using similar instruments as was used for $FePS_3$ analysis in the previous chapter.

Mode-locked was achieved at pump power 280 mW, with minor polarization adjustments. For optimal mode-locking stability, all measurement were taken at the maximum pump power. Similar to $FePS_3$, no pulse were observed when the SA was removed from the cavity.

The optical spectrum of the TDFF mode-locked laser is shown in Figure 6.7. A central wavelength of 1504.7 nm can be observed, with a 0.604 nm 3-dB bandwidth. The laser operates in a soliton regime, with a net anomalous dispersion, proven by the presence of Kelly's sidebands.

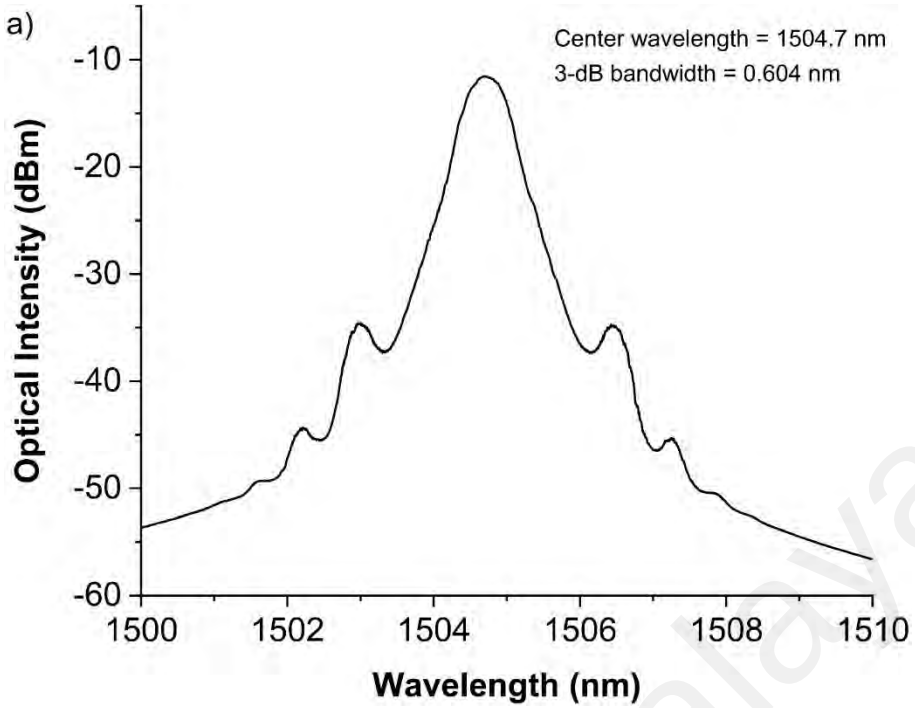

Figure 6.7: Optical spectrum of $MnPS_3$-based mode-locked laser

The mode-locked laser pulse train is shown in Figure 6.8. The pulse spacing can be seen equally spaced at 1.67 µs, matching a repetition rate of 593 kHz. This agrees with the roundtrip time calculated based off the total cavity length using the repetition rate formula shown in Section 5.4 of Chapter 5. The reduced SMF-28 spool length also resulted in a higher repetition rate in comparison to the laser cavity used in Chapter 5. The laser's repetition rate also remained constant at all pump power levels. These results further prove that the laser is in mode-locking operation.

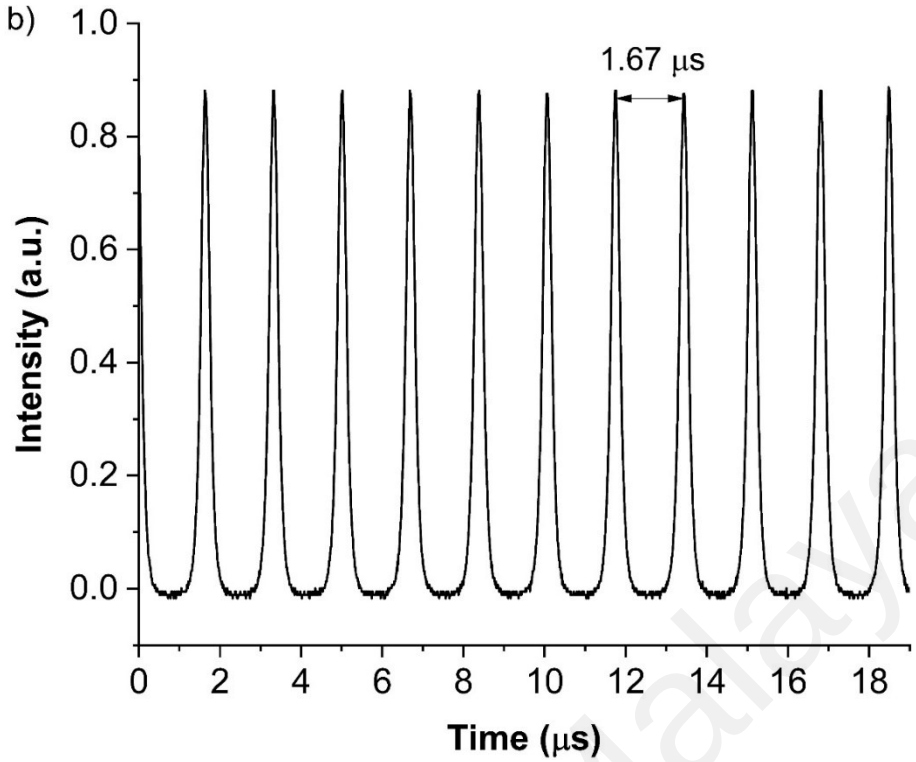

Figure 6.8: Pulse train analysis of $MnPS_3$-based mode-locked laser

The mode-locked laser output was also studied using a radio frequency spectrum analyzer (RFSA). The RFSA was set at a resolution bandwidth (RBW) of 1 kHz. The resulting graph is depicted in Figure 6.9. The signal peaks at a center frequency of 593 kHz, which is in agreement to the findings from the pulse train analysis. The laser exhibited a ~47 dB SNR, signifying a highly stable $MnPS_3$ based TDFF mode-locked laser.

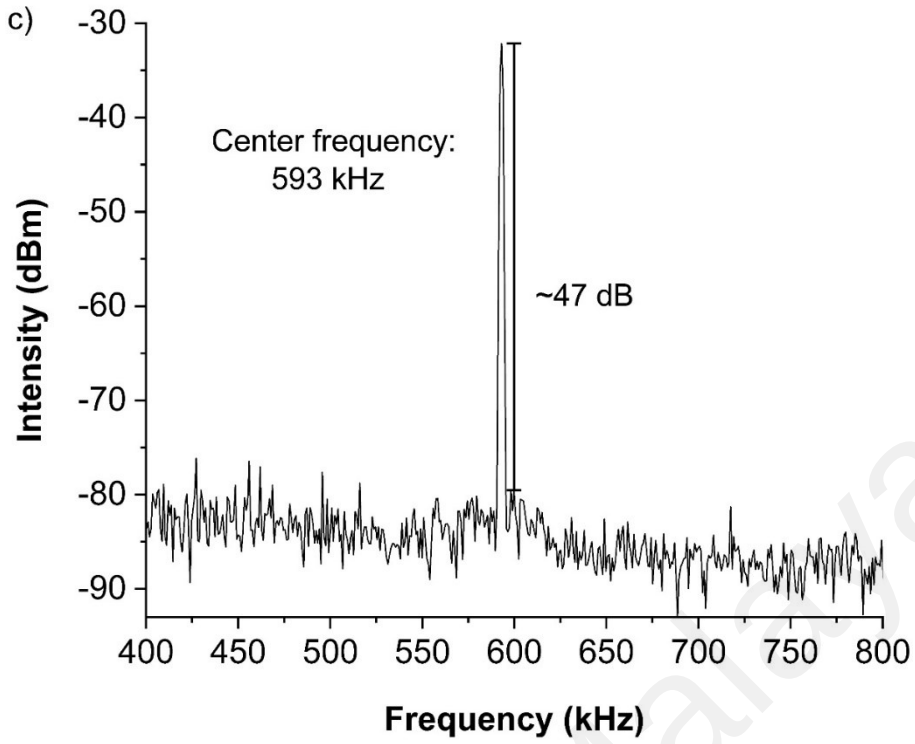

Figure 6.9: Radio frequency spectrum of $MnPS_3$-based mode-locked laser

Similar to $FePS_3$-based TDFF mode-locked laser, the output laser pulse width in this chapter was also analyzed using the Alnair Labs Autocorrelator. The result are as depicted in Figure 6.10. FWHM of the autocorrelation trace for the $MnPS_3$-based mode-locked laser measured 6.15 ps. From there, a pulse width value of 3.98 ps can be derived using the $sech^2$ deconvolution factor of 0.648. Including the center wavelength and 3-dB bandwidth of 1504.7 nm and 0.604 nm respectively, the TBP was calculated to be 0.318. This indicates the pulse generated was slightly chirped when compared to the transform-limited $sech^2$ TBP value of 0.315.

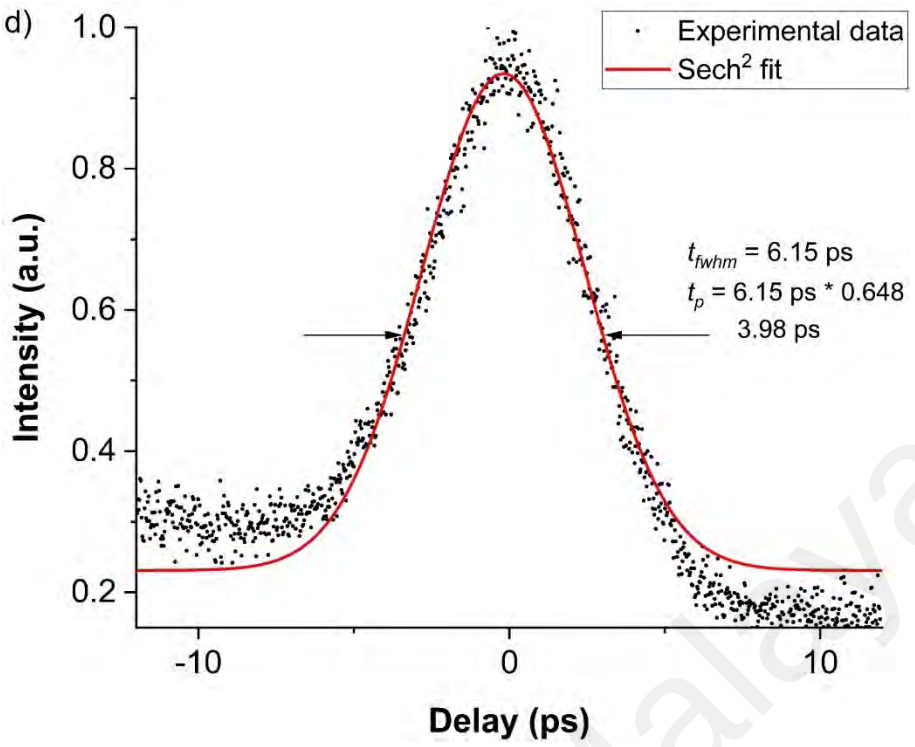

Figure 6.10: Autocorrelator trace with its sech^2 fit $MnPS_3$-based mode-locked laser

Long term operational stability of the $MnPS_3$-based mode-locked TDFF laser was tested by conducting a 3-hour long stability test. Optical spectrum readings were taken every 30 minutes with the pump power set to a stable 280 mW throughout the 3-hour test. The resulting graph is depicted in Figure 6.11, where Figure 6.11(a) shows the 3D plot and Figure 6.11(b) shows its equivalent contour plot. It can be seen that the system remained stable through the test duration, with drift of the center wavelength less than 0.1 nm and peak optical power fluctuates within 0.01 dB. This test was also repeated over longer duration with similar results, indicating that the outstanding stability and repeatability of the $MnPS_3$-based mode-locked TDFF laser and the $MnPS_3$ capability as a stable SA material.

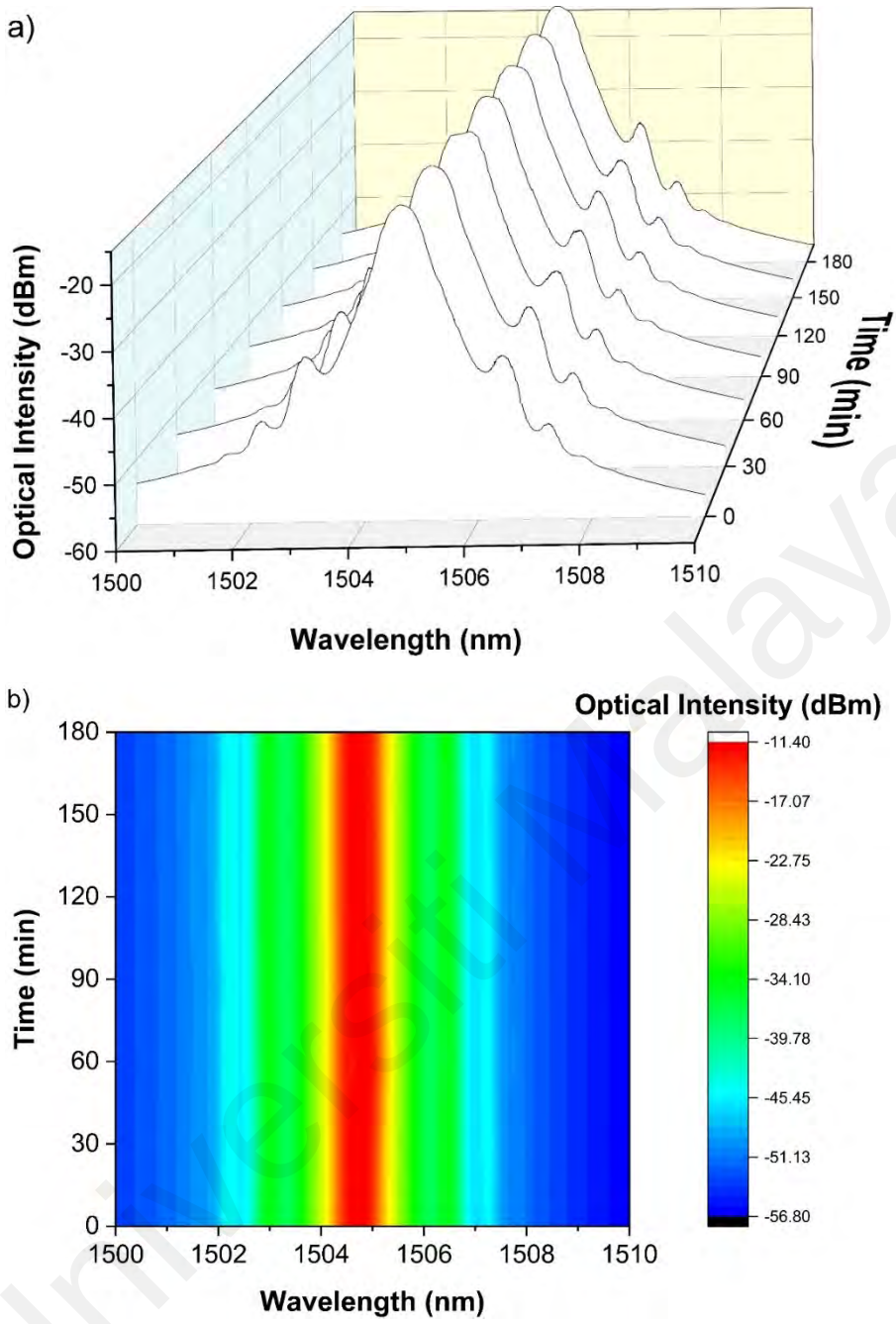

Figure 6.11: Stability test of $MnPS_3$-based mode-locked TDFF laser: (a) 3D graph plot, (b) contour plot

The relation between the $MnPS_3$-based mode-locked TDFF laser's output power and pump power was also studied. This is shown in Figure 6.12. The graph shows that mode-locking operation were sustained between pump power 145 mW and 280 mW, with output power

increasing from 1.14 mW to 3.04 mW respectively. The relationship is linear, with a slope efficiency of 2.1%. At the 10% output port, the laser produced a stable 3.04 mW when pumped at maximum pump power of 280 mW, resulting in a maximum pulse energy of 5.13 nJ and peak power of 1.29 kW.

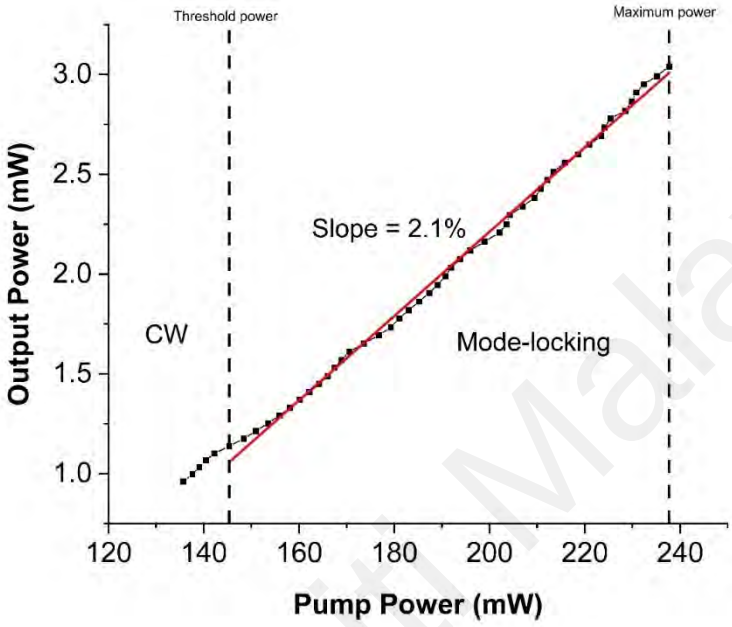

Figure 6.12: Relationship between output power and pump power of $MnPS_3$-based TDFF mode-locked laser

Intracavity average power is determined to be 30.4 mW based off the OC ratio. Using Equation 5.2 and SMF-28 core size of 9 µm as provided by the manufacturer, the intracavity peak power intensity can be calculated to be 3.98 GW/cm^2. Throughout the experiment, the $MnPS_3$/arc-shaped fiber SA showed no observable degradation. This can be concluded that the SA possesses a damage threshold of higher than 3.98 GW/cm^2. As the intracavity power was high, there was no observable Q-switching operation of the laser. To achieve Q-switching, the $MnPS_3$ have to be fabricated into a thin film, resulting in a higher saturable loss suitable for Q-switching operation.

CHAPTER 7: NICKEL PHOSPHORUS TRICHALCOGENIDE ($NIPS_3$)/ARC-SHAPED FIBER AS SATURABLE ABSORBER

7.1 Overview

Another material of the MPX_3 family, Nickel Phosphorus Trichalcogenide ($NiPS_3$) is studied in this chapter as a saturable absorber for mode-locked pulse generation in the S-band wavelength region using the Thulium-doped Fluoride fiber (TDFF) laser system. This chapter will first discuss the fabrication of the $NiPS_3$/arc-shaped fiber SA, including material synthesis and arc-shaped fiber fabrication along with its respective characterizations. The completed device is then introduced into the TDFF system, and its output optical spectrum, pulse train, radio frequency, pulse width and power analyzed and discussed.

In comparison to the TDFF laser cavity showed in Chapter 3, a component in the laser cavity was replaced to further optimize the stability and performance of the laser system and consequently, the mode-locked pulses produced when the SA is inserted. One notable change is the length of the SMF-28 spool was reduced from 500 m to 300 m. This was done to reduce the cavity roundtrip time and as a result, increase the mode-locked pulse repetition rate. This is discussed further in this chapter

The arc-shaped fiber fabrication was also adjusted in an attempt to further improve the mode-locked laser performance. The arc-shaped fiber insertion loss was reduced to 2.0 dB to reduce scattering loss when the $NiPS_3$ nanoflakes are added, all while still maintaining sufficient evanescent field interaction between the laser and the material. This will also be discussed further in this chapter.

7.2 $NiPS_3$ preparation

7.2.1 $NiPS_3$ liquid phase exfoliation (LPE) process

Similarly, the $NiPS_3$ was received in its crystal form before being processed. Different to previous chapter, it was found that the best solvent for $NiPS_3$ nanoflakes to disperse properly is deionized water (DIW). Other than that, the formulation and methodology remained similar to as discussed in Chapter 4. 100 mg of $NiPS_3$ crystals was dispersed in 10 mL of DIW to obtain a $NiPS_3$ solution of 10 mg/mL. This was then bath-sonicated for 8 hours before centrifuged at 5000 rpm for 15 minutes to remove unexfoliated material. The decanted solution is then used as the SA device. Resulting solution is as shown in Figure 7.1.

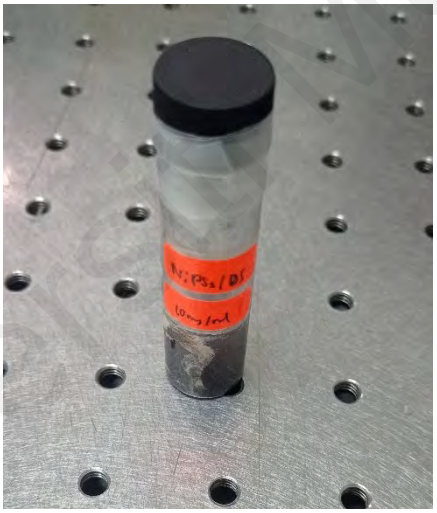

Figure 7.1: Exfoliated $NiPS_3$

7.2.2 Characterization of exfoliated $NiPS_3$

To further understand its characteristics, the $NiPS_3$ underwent a number of material characterizations. One of them is X-ray diffractometry (XRD). It is frequently used to accurately describe a substance's atomic structure and crystallinity. It can also be used to

identify the constituents and compounds present in a sample. XRD works by emitting x-rays at a sample material. Due to the material's crystalline structure, the incident beam will then diffract into certain angles. These diffracted beams also interfere with one another in both constructive and destructive ways, resulting in a variety of intensities at various angles. This measurement may be used to assess a material's chemical bond, the disorder of its crystals, the angles and intensity of the diffracted beam, and more.

Prior to exfoliation, a sample of the $NiPS_3$ crystal was sent for X-ray diffractometry analysis (XRD) to study its purity and crystallinity. The analytical machine used for this is the Empyrean XRD machine from Malvern Panalytical, outfitted with a CuKα radiation source set at 45 kV and 40 mA. Resulting spectrum is shown in Figure 7.2. From the spectrum, it can be seen that all peaks are well defined and sharp, indicating high crystallinity and purity of the $NiPS_3$ sample. These peaks are coordinated at 2θ = 14.24, 28.38°, 30.29°, 31.30°, 36.37°, 45.96°, 49.71°, 53.58°, 54.78°, 58.39°, and 75.06°, and according to the Joint Committee on Powder Diffraction Standards, these peaks can be assigned to planes (0 0 1), (0 0 2), (1 1 2), (1 3 0), (1 3 1), (0 4 1), (-1 3 3), (-1 5 2), (0 6 0), (0 0 4), and (-2 2 5).According to Ouvrard *et al.*, sharp peaks corresponding to planes (0 0 1), (0 0 4) and (0 0 2) for $NiPS_3$ indicates high purity of the sample (Ouvrard et al., 1985).

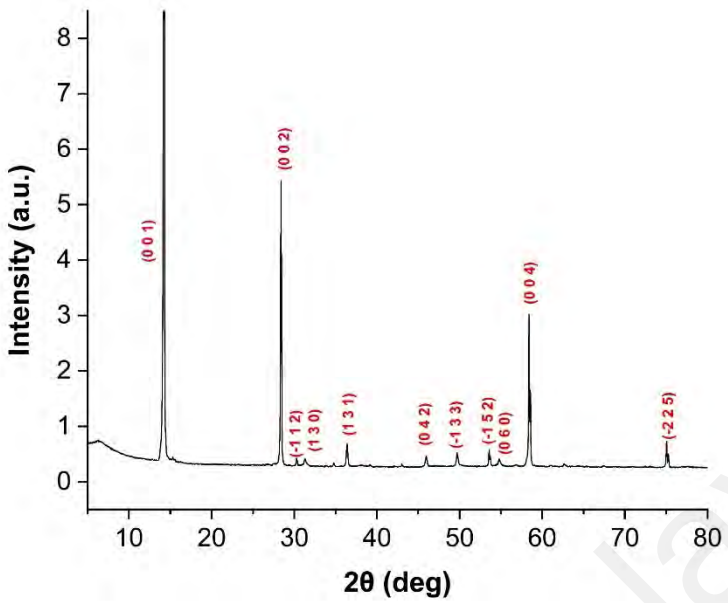

Figure 7.2: $NiPS_3$ XRD spectrum

High-Resolution Transmission Electron Microscopy is an additional technique for material analysis (HRTEM). HRTEM is a sophisticated tool that enables imaging down to atomic scales. We can investigate the atomic-scale characteristics of materials and comprehend their lattice structures and crystal grain patterns courtesy to its tremendous magnification capability. In HRTEM, a sample is passed through by an electron beam in a vacuum. Several elements of information about the sample are carried in the transmitted electron beam. Elastically scattered electrons are produced as a result of the electron beam's interaction with the atoms in the sample. Additionally, there are electrons that are inelastically dispersed as a result of the electron beam losing some of its energy via interactions with the atoms in the sample. These two, coupled with the electron that is transmitted, form a complete image of the sample's internal structure.

This was done on the exfoliated sample to study its morphology and lattice structure. This also to confirm that the exfoliation process was successful. The resulting image is shown in Figure 7.3. Figure 7.3(a) was captured at 4k magnification and shows the few-layer characteristics of the $NiPS_3$ morphology. This also confirms that the LPE process was a success and the bulk form of the $NiPS_3$ was exfoliated. Figure 7.3(b) shows the lattice structure of $NiPS_3$ at 400k magnification. Further magnification was unviable as the high energy electron beam of the HRTEM damaged the focused site, making image capture impossible. Nevertheless, at 400k magnification, we can see uniform grains of the $NiPS_3$, indicating high crystallinity of the nanoflakes. This agrees with the XRD findings.

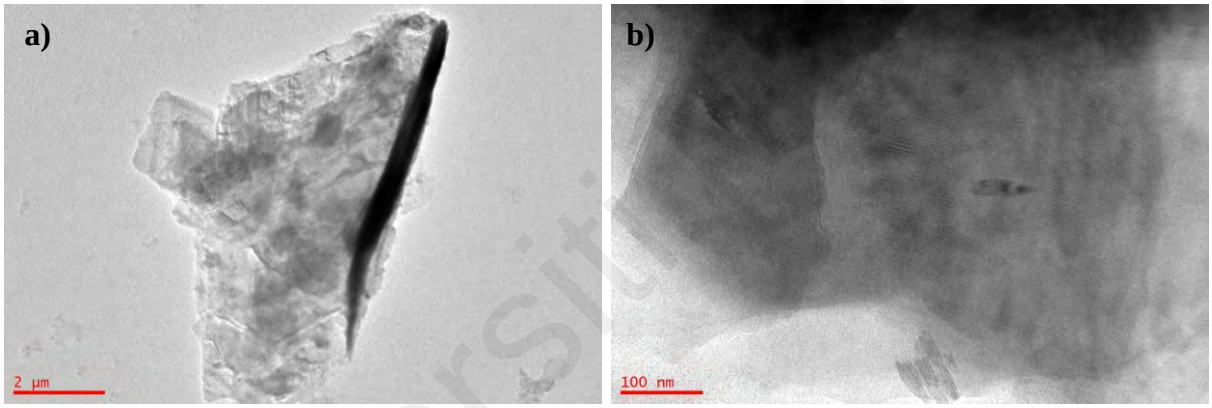

Figure 7.3: HRTEM images of $NiPS_3$: (a) few-layer flake (b) lattice structure

The optical properties of $NiPS_3$ were also investigated since it is used in this work as an optical material. The UV-Vis-NIR (UV-Visible-Near Infrared) absorption spectroscopy is one technique employed. It measures the intensity of light after it has passed through a sample (I) and contrasts it with the intensity of light before the sample (I_0). Transmittance, often known as the I/I0 ratio, is quantified as a percentage (%T). This allows the formula below to be used to determine the absorbance, A:

$$A = -\log\left(\frac{\%T}{100\%}\right) \qquad Equation\ 7.1$$

The exfoliated $NiPS_3$ underwent a UV-Vis-NIR spectroscopy to understand its absorbance characteristics. This characterization also allows us to determine the optical band gap of the exfoliated $NiPS_3$. Similar to the one used in Chapter 5, UV-Vis-NIR analysis done on $NiPS_3$ uses the Perkin Elmer Lambda 750 UV-Vis-NIR spectrometer with the wavelength of light range set between 200 nm to 2100 nm. Resulting spectrum was also converted to its matching Tauc's plot to determine its band gap. Both graphs are shown in Figure 7.4, with Figure 7.4(a) showing the UV-Vis-NIR spectrum and Figure 7.4(b) showing the Tauc's plot. It can be seen that the $NiPS_3$ have a broad absorption wavelength range between 300 nm to 1600 nm. The Tauc's plot extrapolation shows the $NiPS_3$ possesses a band gap of ~1.8 eV.

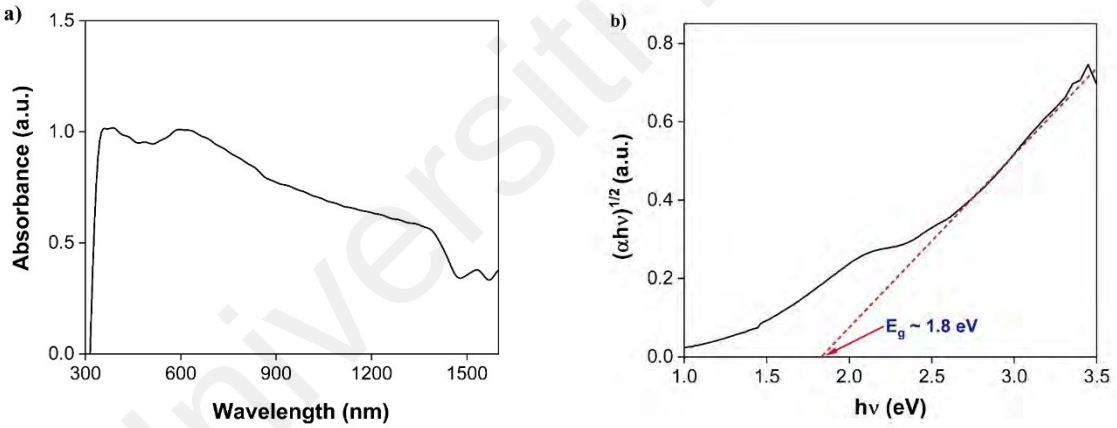

Figure 7.4: UV-Vis-NIR results: (a) UV-Vis-NIR absorption spectrum of $NiPS_3$, (b) its corresponding Tauc's plot

7.3 $NiPS_3$/arc-shaped fiber

7.3.1 Two-step arc-shaped fiber fabrication (2.0 dB loss)

Arc-shaped fiber fabrication method is similar to the one discussed in Chapter 4. The only change is the targeted insertion loss. The arc-shaped fiber used for $NiPS_3$/arc-shaped fiber SA was fabricated to a reduced loss of 2.0 dB.

The first polishing phase using the 30 µm grit sandpaper was done until loss was about 1.8 dB. The sandpaper was changed to the 1 µm grit polishing film for the second phase until loss was 2.0 dB. The completed arc-shaped fiber was then coated with approximately 2.5 µL of the exfoliated $NiPS_3$ solution. Figure 7.5(a) shows the arc-shaped fiber, while Figure 7.5(b) shows the completed $NiPS_3$/arc-shaped fiber SA, where the coating can be seen.

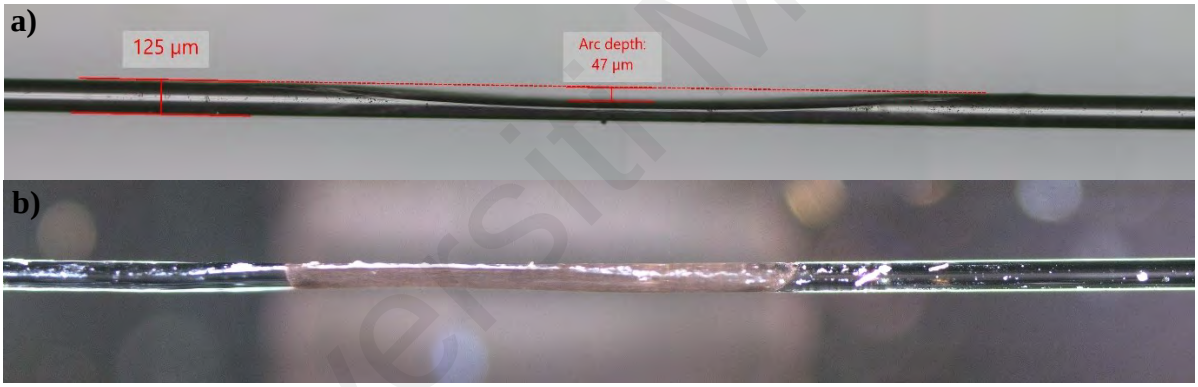

Figure 7.5: (a) 2.0 dB loss arc-shaped fiber (b) $NiPS_3$ coated arc-shaped fiber

7.3.2 Characterization of $NiPS_3$/arc-shaped fiber

The modulation depth of the $NiPS_3$/arc-shaped fiber SA was determined using the twin-detector measurement method as depicted in Chapter 4. The raw data obtained from the procedure was fitted to the saturation equation model as presented in Figure 7.6. Results shows

the SA device have a modulation depth of 29.44 %. The saturation intensity and non-saturable absorption was determined to be 0.547 kW/cm^2 and 70.56 % respectively.

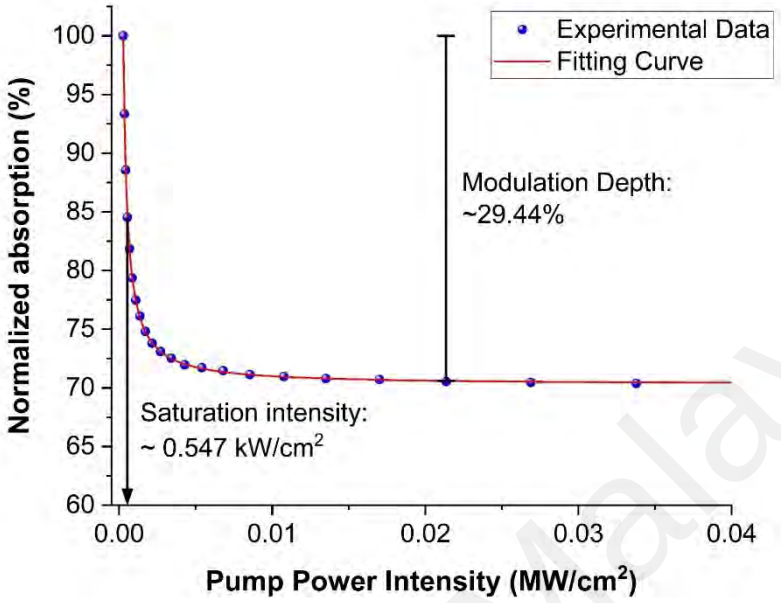

Figure 7.6: Nonlinear characteristics of $NiPS_3$/arc-shaped fiber SA

7.4 Characterization of S-band mode-locked thulium-doped fluoride fiber using $NiPS_3$ as saturable absorber

The $NiPS_3$/arc-shaped fiber SA was inserted into the TDFF as depicted in Section 3.2.6: 'Final cavity configuration' of Chapter 3. Configuration and position of components of the cavity was similar, with the exception of the SMF-28 spool, which was reduced from 500 m to 300 m. Some components were changed with a more efficient part. Nonetheless, specifications such as the output coupler ratio, polarization controller configuration and other remained the same as configured in Chapter 3.

For this experiment, the cavity length amounted to a total of 350 m, with the inclusion of TDFF gain medium, and the SMF-28 pigtails used for all components such as ISO, WDM, OC

and PC. The group velocity dispersion will be calculated using similar material dispersion and center wavelength values as mentioned in Section 3.2.6. The new total cavity length was used in Equation 3.1, resulting in a net cavity dispersion of -5.73 ps^2. All measurements were taken with similar analytical equipment as used in Chapter 5. Mode-locking operation were obtained at the pump power of 280 mW. Minor polarization adjustments using the PC was required. The power was kept constant during readings to optimize stability and uniformity among the different types of characterization. Similar to reports in Chapter 5 and 6, no pulses were detected when the $NiPS_3$/arc-shaped fiber SA was removed from the cavity, indicating that the

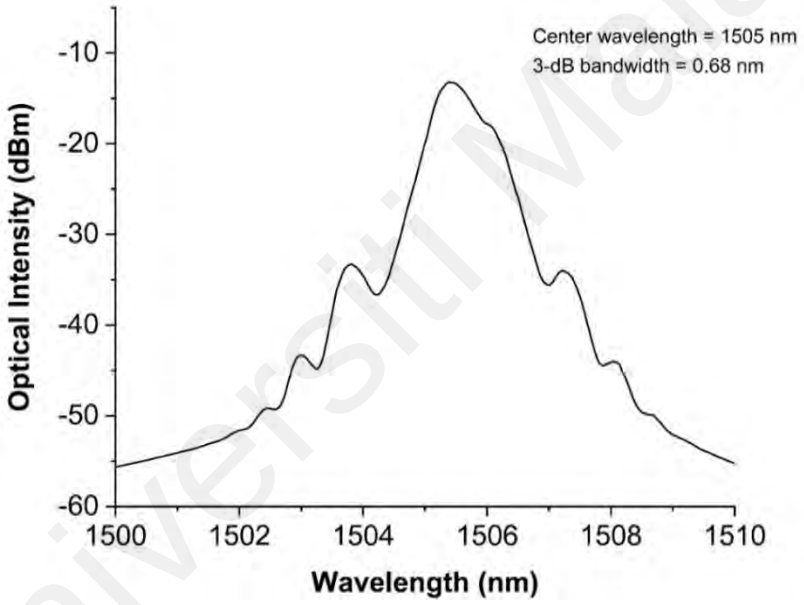

Figure 7.7: Optical spectrum of $NiPS_3$-based mode-locked laser

mode-locked pulses are resulted by the application of the SA.

The $NiPS_3$-based TDFF mode-locked laser produced an optical spectrum as shown in Figure 7.7. The spectrum showed a central wavelength of 1505 nm with a 3-dB bandwidth of 0.68 nm.

Kelly's sidebands were observed in the spectrum, indicating the operation of the mode-locked TDFF laser was in the soliton regime with net anomalous dispersion.

Pulse train of the mode-locked laser was also analyzed and shown in Figure 7.8. It can be seen that the pulses have an equal separation at 1.71 μs, matching a repetition rate of 582 kHz. This agrees with the roundtrip time calculated based off the total cavity length using the repetition rate formula f=c/Ln, where c, L and n identifies as light speed, length of cavity and refractive index of travel medium, and results in the unit Hertz (Hz). Reducing the length of the SMF-28 spool resulted in a higher repetition rate compared to the results shown in Chapter 5. The laser's repetition rate also remained constant at all pump power levels. These results further prove that the laser is in mode-locking operation.

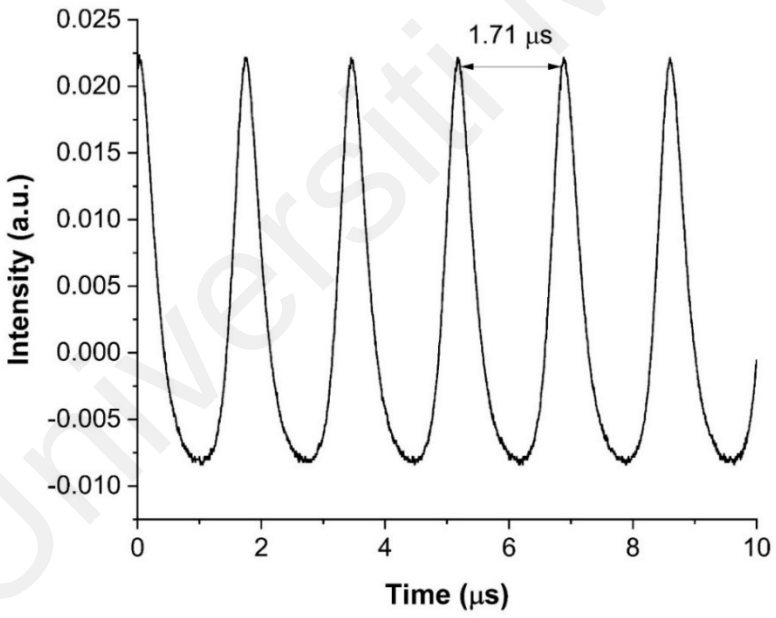

Figure 7.8: Pulse train analysis of $NiPS_3$-based mode-locked laser

Radio frequency analysis was also conducted on the mode-locked laser output, as shown in Figure 7.9. The resolution bandwidth (RBW) was set to 1 kHz. The spectrum showed a sharp peak at 582 kHz, matching the findings pulse train analysis. The mode-locked laser also exhibited a signal-to-noise ratio (SNR) of 58 dB, signifying the high-stability of the $NiPS_3$-based mode-locked laser.

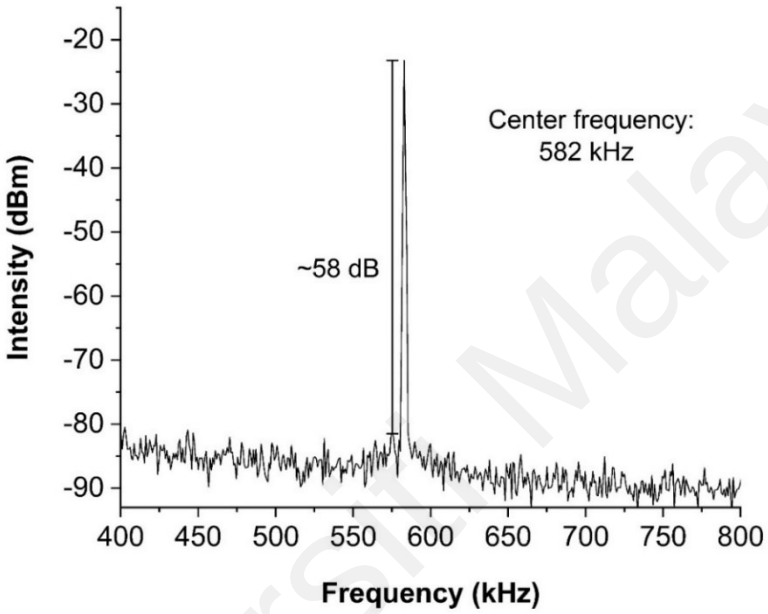

Figure 7.9: Radio frequency spectrum of $NiPS_3$-based mode-locked laser

The pulse width of the mode-locked laser is shown in Figure 7.10. The full width at half maximum (FWHM) of the autocorrelation trace for the $NiPS_3$-based mode-locked laser measured 5.49 ps. From there, a pulse width value of 3.56 ps can be derived using the $sech^2$ deconvolution factor of 0.648. Including the center wavelength and 3-dB bandwidth of 1505 nm and 0.68 nm respectively, the TBP was calculated to be 0.320. This indicates the pulse generated was slightly chirped when compared to the transform-limited $sech^2$ TBP value of 0.315.

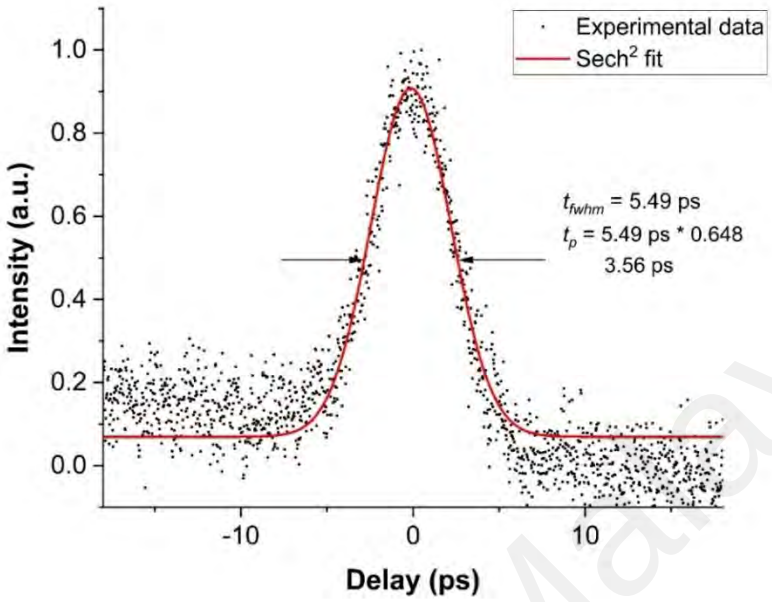

Figure 7.10: Autocorrelator trace with its sech^2 fit $NiPS_3$-based mode-locked laser

The laser was operated at 280 mW pump power for 3 hours to study it long term operational stability. Optical spectrum of the laser's output was taken every 30 minutes. The resulting graph was plotted in Figure 7.11. It can be observed that the laser remained stable through the test duration with central wavelength drift of less than 0.1 nm and peak optical power fluctuation of less than 0.01 dB. The $NiPS_3$/arc-shaped fiber SA also showed no significant degradation The test was also replicated over a longer period, with similar outcome. This proves that the $NiPS_3$-based mode-locked TDFF system is very stable and the $NiPS_3$ a viable SA material.

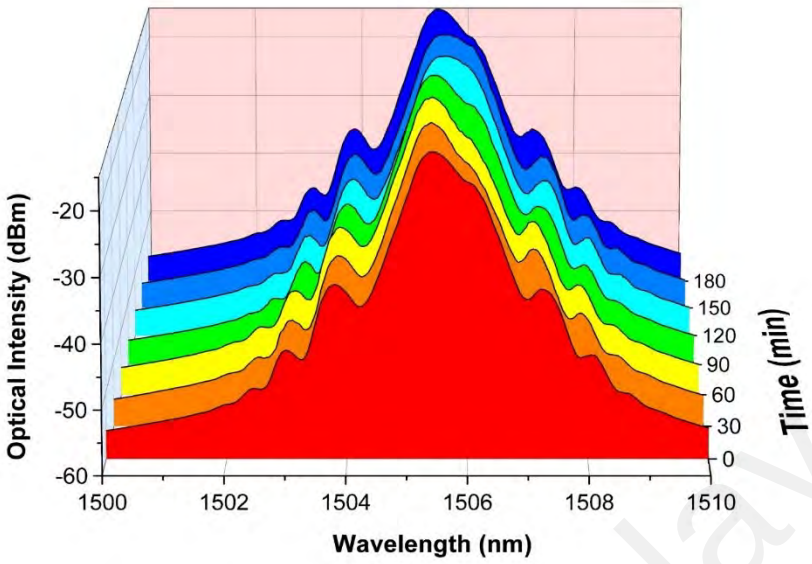

Figure 7.11: Stability test of $NiPS_3$-based mode-locked TDFF laser

Output power/pump power relation was also analyzed. The graph is shown in Figure 7.12. The TDFF laser was in mode-locking operation between pump powers 211 mW to 280 mW. Output power at the 10 % port was observed to be 1.7 mW to 2.4 mW respectively. This gives a slope efficiency of 1.6 %. At the 10% output port, output power of 2.4 mW results in pulse energy and peak power of 4.12 nJ and 1.16 kW respectively.

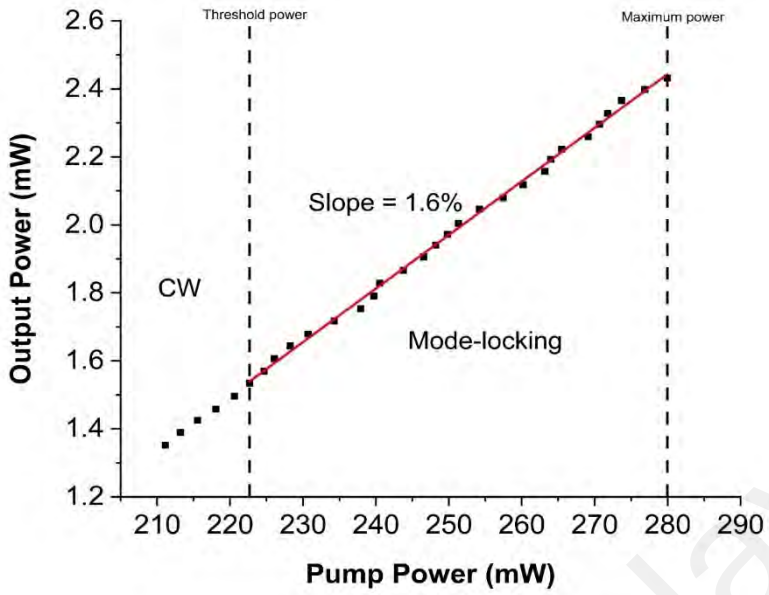

Figure 7.12: Relationship between output power and pump power of $NiPS_3$-based TDFF mode-locked laser

Based on the OC ratio, the intracavity power is 24 mW. Using Equation 5.2 and the SMF-28 core size is 9 µm as provided by the manufacturer, this results in an intracavity peak power intensity of 18.21 GW/cm^2. Since the $NiPS_3$/arc-shaped fiber SA was not damaged throughout the experiment, it can be concluded that the SA possesses a damage threshold of higher than 18.21 GW/cm^2. Intracavity power is high, making any Q-switching virtually impossible. For Q-switching to be achieved, the $NiPS_3$ have to be fabricated into a film, which would result in a higher non-saturable loss, suitable for Q-switching.

CHAPTER 8: CONCLUSIONS

8.1 Conclusion

In this thesis, the performance of transition metal phosphorus trichalcogenide (MPX_3) as a saturable absorber in a thulium-doped fluoride fiber laser system for generation of mode-locked pulses in S-band optical region was studied. In Chapter 1, the background of this work was discussed as well as an introduction into the S-band fiber laser and MPX_3 materials. Chapter 2 then discussed the history of fiber lasers, its developments, and the theoretical basis of S-band lasers. Basics of pulse in a fiber laser system, specifically mode-locked pulses are also discussed including the use of saturable absorbers, its history, and applications. The chapter also focuses on thulium-doped fluoride fiber in particular as the gain medium, and the MPX_3 materials as saturable absorbers.

This thesis then proceeds with the methodology of this work. Chapter 3 describes the build of the thulium-doped fluoride fiber laser cavity, with the introduction and operational understanding of each components and its role in the laser system. The chapter also includes the analytical instruments used in this work and its role in measuring the output of the mode-locked laser. Chapter 4 then continues with the fabrication of the MPX_3/arc-shaped fiber used in this work. The methodology background including the synthesis method of the MPX_3 materials, and the polishing method of the arc-shaped fiber was described in the chapter.

Chapters 5, 6, and 7 discusses the results and analysis of each materials of the MPX_3 family used in this work (Iron Phosphorus Trichalcogenide ($FePS_3$), Manganese Phosphorus Trichalcogenide ($MnPS_3$) and Nickel Phosphorus Trichalcogenide ($NiPS_3$). The characterization of the materials and the completed saturable absorber device is discussed in

the chapters. The performance of each saturable absorbers are analyzed using equipment such as optical spectrum analyser, oscilloscope, radio frequency spectrum analyser and autocorrelator, among others. The outputs were studied and presented in the chapters.

8.1.1 Iron Phosphorus Trichalcogenide ($FePS_3$)/arc-shaped fiber as Saturable Absorber

This chapter discussed the fabrication and characterization of Iron Phosphorus Trichalcogenide ($FePS_3$)/arc-shaped fiber SA and the generated mode-locked pulse in the TDFF laser cavity system.

The $FePS_3$ crystal underwent liquid phase exfoliation (LPE) process in isopropyl alcohol (IPA) solvent to produce a solution of 10 mg/mL. The $FePS_3$ was characterized using XRD, FESEM, HRTEM and UV-Vis-NIR among others. The arc-shaped fiber was fabricated using the two-step polishing method to an insertion loss of 3.0 dB, before being drop-casted with 2.5 µL of the $FePS_3$ solution. The completed SA was analysed for its nonlinear and linear absorption characteristics. The SA showed linear absorption of around 2.5 to 3.1 dB within the S-band region and a nonlinear modulation depth of 29.44%

The SA was introduced to the TDFF laser cavity and generated mode-locked pulses at 1504.8 nm central wavelength and 3-dB bandwidth of 0.704 nm. The repetition rate was determined to be 400 kHz with a SNR of ~45 dB. Pulse width of the output laser was measured to be 3.90 ps and the laser had a TBP of 0.363. The $FePS_3$-based TDFF mode-locked laser showed an admirable long term-stability with minimal central wavelength shift and optical power fluctuations. The SA also sustained optical intensity of 59.5 GW/cm^2 without noticeable damage or performance degradation, showing the very high damage threshold of the $FePS_3$/arc-

shaped fiber SA. The results proves the applicability of $FePS_3$ as a SA for S-band mode-locked pulse generation in TDFF laser system.

8.1.2 Manganese Phosphorus Trichalcogenide ($MnPS_3$)/arc-shaped fiber as Saturable Absorber

This chapter discussed the fabrication and characterization of Manganese Phosphorus Trisulfide ($MnPS_3$)/arc-shaped fiber SA and the generated mode-locked pulse in TDFF laser cavity system.

The $MnPS_3$ crystal underwent liquid phase exfoliation (LPE) process in N-Methyl-2-Pyrrolidone (NMP) solvent to produce a solution of 10 mg/mL. This solvent was selected in comparison to IPA mentioned in Chapter 4 due to the better dispersion of the material in NMP. The $MnPS_3$ was characterized using XRD, FESEM, Raman spectroscopy among others. The arc-shaped fiber was fabricated using the two-step polishing method to an insertion loss of 2.5 dB, before being drop-casted with 2.5 µL of the $MnPS_3$ solution. The lower loss results in a more stable laser system with lower SA insertion loss. The completed SA was analysed for its nonlinear absorption characteristics. The SA a nonlinear modulation depth of 25.63% at 1500 nm.

The TDFF laser cavity was modified in comparison to Chapter 3, specifically on the length of the SMF-28 spool. The spool was reduced from 500 m to 300 m to increase the repetition rate. The SA was introduced to the TDFF laser cavity and generated mode-locked pulses at 1504.7 nm central wavelength and 3-dB bandwidth of 0.604 nm. The repetition rate was determined to be 593 kHz with a SNR of ~47 dB. Pulse width of the output laser was measured to be 3.98 ps and the laser had a TBP of 0.318. The $MnPS_3$-based TDFF mode-locked laser

showed an admirable long term-stability with minimal central wavelength shift and optical power fluctuations. The SA also sustained optical intensity of 3.98 GW/cm^2 without noticeable damage or performance degradation, showing the very high damage threshold of the $MnPS_3$/arc-shaped fiber SA. The results proves the applicability of $MnPS_3$ as a SA for S-band mode-locked pulse generation in TDFF laser system

8.1.3 Nickel Phosphorus Trichalcogenide ($NiPS_3$)/arc-shaped fiber as Saturable Absorber

This chapter discussed the fabrication and characterization of Nickel Phosphorus Trisulfide ($NiPS_3$)/arc-shaped fiber SA and the generated mode-locked pulse in TDFF laser cavity system.

The $NiPS_3$ crystal underwent liquid phase exfoliation (LPE) process in De-ionized Water (DIW) solvent to produce a solution of 10 mg/mL. This solvent was selected in comparison to IPA mentioned in Chapter 4 due to the better dispersion of the material in DIW. The $NiPS_3$ was characterized using XRD, HRTEM and UV-Vis-NIR among others. The arc-shaped fiber was fabricated using the two-step polishing method to an insertion loss of 2.0 dB, before being drop-casted with 2.5 µL of the $NiPS_3$ solution. The lower loss results in a more stable laser system with lower SA insertion loss. The completed SA was analysed for its nonlinear absorption characteristics. The SA a nonlinear modulation depth of 29.44% at 1500 nm.

The TDFF laser cavity was modified in comparison to Chapter 3, specifically on the length of the SMF-28 spool. The spool was reduced from 500 m to 300 m to increase the repetition rate. The SA was introduced to the TDFF laser cavity and generated mode-locked pulses at 1505 nm central wavelength and 3-dB bandwidth of 0.68 nm. The repetition rate was determined to be 582 kHz with a SNR of ~58 dB. Pulse width of the output laser was measured

to be 3.56 ps and the laser had a TBP of 0.320. The $NiPS_3$-based TDFF mode-locked laser showed an admirable long term-stability with minimal central wavelength shift and optical power fluctuations. The SA also sustained optical intensity of 18.21 GW/cm^2 without noticeable damage or performance degradation, showing the very high damage threshold of the $MnPS_3$/arc-shaped fiber SA. The results proves the applicability of $MnPS_3$ as a SA for S-band mode-locked pulse generation in TDFF laser system.

8.2 Summary

Three MPX_3 materials, $FePS_3$, $MnPS_3$, and $NiPS_3$ were fabricated into an arc-shaped fiber saturable absorber for mode-locked pulse generation. The mode-locked pulses were generated in a Thulium-doped fluoride fiber ring laser cavity, resulting in the output in the S-band optical region. The results of this work can be summarized in Table 8.1.

Table 8.1: Summary of thesis

	$FePS_3$	**$MnPS_3$**	**$NiPS_3$**
Center wavelength (nm)	1504.8	1504.7	1505
3-dB bandwidth (nm)	0.704	0.604	0.68
Repetition rate (kHz)	400.6	593	582
Signal-to-noise ratio (SNR) (dB)	45	47	58
Pulse width (ps)	3.90	3.98	3.56
Wavelength shift after 3 hours (nm)	<0.1	<0.1	<0.1

Power fluctuations after 3 hours (dB)	<0.01	<0.01	<0.01
Max output power (mW)	3.01	3.04	2.4
Intracavity peak power intensity (GW/cm^2)	59.5	3.98	18.21

8.3 Future works

The significance of this work is proving the capabilities of the transition metal phosphorus trisulfide 2D material family as an optical material capable of generating mode-locked pulse in a laser cavity. The gain medium used can be replaced with other fluoride glass fibers such as praseodymium-doped fluoride fiber, which can generate laser in the O-band optical wavelength region.

Similar methodology can be applied on other materials of the same 2D material family such as cobalt phosphorus trisulfide ($CoPS_3$) and zinc phosphorus trisulfide ($ZnPS_3$). Possibilities and applicability of other methods of material synthesis including chemical vapor transportation (CVT) can be experimented further. The findings can be compared and studied. The arc-fiber fabrication method can also be adjusted and refined to reduce the intracavity loss while still maintain a stable evanescent field interaction between the material and the laser system. The arc-depth may differ for each material.

The concept of biconical tapered fiber and microfiber can also be studied in place of the arc-shaped fiber in this work as a method of introducing the MPX_3 material into the laser path. The

uniform diameter of the tapered region may provide lower polarization dependent loss in comparison to the arc-shaped fiber.

REFERENCES

Addanki, S., Amiri, I. S., & Yupapin, P. (2018). Review of optical fibers-introduction and applications in fiber lasers. *Results in Physics*, *10*, 743-750.

Agrawal, G. P. (2001). *Applications of nonlinear fiber optics*. Elsevier.

Ahmad, H., Azmy, N. F., Norisham, N. F., Reduan, S. A., & Zulkifli, M. Z. (2022). Thulium-doped fluoride mode-locked fiber laser based on nonlinear polarization rotation. *Optical and Quantum Electronics*, *54*(2), 1-11.

Ahmad, H., Hassan, H., Zulkifli, A., Thambiratnam, K., & Amiri, I. (2017). Characterization of arc-shaped side-polished fiber. *Optical and Quantum Electronics*, *49*(6), 1-13.

Ahmad, H., Zulkifli, M. Z., Latif, A. A., Thambiratnam, K., & Harun, S. W. (2009). Bidirectional S-band continuous wave operation in a depressed-cladding erbium doped fiber amplifier. *Journal of Optoelectronics and Advanced Materials*, *11*(5), 547-553.

Ahmed, M. H. M. (2015). *Development of Q-switched and mode-locked erbium doped fiber lasers based on carbon nanotubes saturable absorbers* Jabatan Kejuruteraan Elektrik, Fakulti Kejuruteraan, Universiti Malaya].

Amemiya, T., & Nakano, Y. (2010). Single Mode Operation of 1.5-μm Waveguide Optical Isolators Based on the Nonreciprocal-loss Phenomenon. In *Advances in Optical and Photonic Devices*. IntechOpen.

Aozasa, S., Sakamoto, T., Kanamori, T., Hoshino, K., Kobayashi, K., & Shimizu, M. (2000). Tm-doped fiber amplifiers for 1470-nm-band WDM signals. *IEEE Photonics Technology Letters*, *12*(10), 1331-1333.

Arbore, M. A. (2005). Communication system using S-band Er-doped fiber amplifiers with depressed cladding. In: Google Patents.

Aruchamy, A., Berger, H., & Levy, F. (1988). Photoelectronic properties of the p-type layered trichalcogenophosphates FePS3 and FePSe3. *Journal of Solid State Chemistry*, *72*(2), 316-323. https://doi.org/https://doi.org/10.1016/0022-4596(88)90035-7

Bünzli, J.-C. G., & Piguet, C. (2005). Taking advantage of luminescent lanthanide ions. *Chemical Society Reviews*, *34*(12), 1048-1077.

Chiu, J.-C., Lan, Y.-F., Chang, C.-M., Chen, X.-Z., Yeh, C.-Y., Lee, C.-K., Lin, G.-R., Lin, J.-J., & Cheng, W.-H. (2010). Concentration effect of carbon nanotube based

saturable absorber on stabilizing and shortening mode-locked pulse. *Optics express*, *18*(4), 3592-3600.

Chukanov, N. V., & Chervonnyi, A. D. (2016). Some general aspects of the application of IR spectroscopy to the investigation of minerals. In *Infrared Spectroscopy of Minerals and Related Compounds* (pp. 1-49). Springer.

Csele, M. (2011). *Fundamentals of light sources and lasers*. John Wiley & Sons.

DeMaria, A., Stetser, D., & Heynau, H. (1966). Self mode-locking of lasers with saturable absorbers. *Applied Physics Letters*, *8*(7), 174-176.

Digonnet, M. J. (2001). *Rare-earth-doped fiber lasers and amplifiers, revised and expanded*. CRC press.

Dong, B., Hu, J., Liaw, C.-Y., Hao, J., & Yu, C. (2011). Wideband-tunable nanotube Q-switched low threshold erbium doped fiber laser. *Applied optics*, *50*(10), 1442-1445.

El-Meligi, A., Madian, M., & Ismail, N. (2015). Fabrication and characterization single crystal of FePS3 layered material. *Iarjset.*, *2*, 117.

Electronics, C. (2023). Wavelength Division Multiplexing Diagram. In. Electronics Coach. https://electronicscoach.com/wavelength-division-multiplexing.html

Ennejah, T., & Attia, R. (2013). Mode locked fiber lasers. *Current Developments in Optical Fiber Technology*, 405-426.

Floridia, C., Carvalho, M., Lüthi, S., & Gomes, A. (2004). Modeling the distributed gain of single-(1050 or 1410 nm) and dual-wavelength-(800+ 1050 nm or 800+ 1410 nm) pumped thulium-doped fiber amplifiers. *Optics letters*, *29*(17), 1983-1985.

Gomes, A., Carvalho, M., Sundheimer, M., Bastos-Filho, C., Martins-Filho, J., e Silva, M. C., Von der Weid, J., & Margulis, W. (2003). Characterization of efficient dual-wavelength (1050+ 800 nm) pumping scheme for thulium-doped fiber amplifiers. *IEEE Photonics Technology Letters*, *15*(2), 200-202.

Gui, Q., Feng, Y., Chen, B., Gu, F., Chen, L., Meng, S., Xu, M., Xia, M., Zhang, C., & Yang, J. (2021). Extrinsic-Structured Bimetallic-Phase Ternary Metal Phosphorus Trisulfides Coupled with N-Doped Graphitized Carbon for Superior Electrochemical Lithium Storage. *Advanced Energy Materials*, *11*(8), 2003553. https://doi.org/https://doi.org/10.1002/aenm.202003553

Gursel, A. T. (2018). Fiber lasers and their medical applications. *Optical Amplifiers-A Few Different Dimensions*.

Gusmão, R., Sofer, Z., & Pumera, M. (2019). Exfoliated layered manganese trichalcogenide phosphite (MnPX3, X= S, Se) as electrocatalytic van der Waals materials for hydrogen evolution. *Advanced Functional Materials*, *29*(2), 1805975.

Han, X., Song, P., Xing, J., Chen, Z., Li, D., Xu, G., Zhao, X., Ma, F., Rong, D., Shi, Y., Islam, M. R., Liu, K., & Huang, Y. (2021). High-Performance Phototransistors Based on MnPSe3 and Its Hybrid Structures with Au Nanoparticles. *ACS Applied Materials & Interfaces*, *13*(2), 2836-2844. https://doi.org/10.1021/acsami.0c19530

He, J., Tao, L., Zhang, H., Zhou, B., & Li, J. (2019). Emerging 2D materials beyond graphene for ultrashort pulse generation in fiber lasers. *Nanoscale*, *11*(6), 2577-2593.

Ishio, H., Minowa, J., & Nosu, K. (1984). Review and status of wavelength-division-multiplexing technology and its application. *Journal of lightwave technology*, *2*(4), 448-463.

Jastrzębski, W., Sitarz, M., Rokita, M., & Bułat, K. (2011). Infrared spectroscopy of different phosphates structures. *Spectrochimica Acta Part A: Molecular and Biomolecular Spectroscopy*, *79*(4), 722-727.

Jha, A., Richards, B., Jose, G., Teddy-Fernandez, T., Joshi, P., Jiang, X., & Lousteau, J. (2012). Rare-earth ion doped TeO2 and GeO2 glasses as laser materials. *Progress in Materials Science*,*57*(8),1426-1491. https://doi.org/https://doi.org/10.1016/j.pmatsci.2012.04.003

Kao, K. C., & Hockham, G. A. (1966). Dielectric-fibre surface waveguides for optical frequencies. Proceedings of the Institution of Electrical Engineers,

Kasim, N., Anyi, C., Haris, H., Ahmad, F., Ali, N., Ahmad, H., Munajat, Y., & Harun, S. (2014). Q-switched erbium-doped fiber laser using multi-layer graphene based saturable absorber. *Journal of Nonlinear Optical Physics & Materials*, *23*(01), 1450009.

Keiser, G. E. (1999). A review of WDM technology and applications. *Optical Fiber Technology*, *5*(1), 3-39.

Keller, U., Weingarten, K. J., Kartner, F. X., Kopf, D., Braun, B., Jung, I. D., Fluck, R., Honninger, C., Matuschek, N., & Der Au, J. A. (1996). Semiconductor saturable absorber mirrors (SESAM's) for femtosecond to nanosecond pulse generation in solid-state lasers. *IEEE Journal of Selected Topics in Quantum Electronics*, *2*(3), 435-453.

Koester, C. (1966). 9A4-Laser action by enhanced total internal reflection. *IEEE Journal of quantum electronics*, *2*(9), 580-584.

Koester, C. J., & Snitzer, E. (1964). Amplification in a fiber laser. *Applied optics*, *3*(10), 1182-1186.

Kuo, H.-H., & Hong, S.-F. (2014). Nanographene-based saturable absorbers for ultrafast fiber lasers. *Journal of Nanomaterials*, *2014*.

Leigh, G. J. (1990). *Nomenclature of inorganic chemistry: recommendations 1990*. Blackwell scientific publications Oxford.

Li, J., Luo, H., He, Y., Liu, Y., Zhang, L., Zhou, K., Rozhin, A. a., & Turistyn, S. (2014). Semiconductor saturable absorber mirror passively Q-switched 2.97 μm fluoride fiber laser. *Laser Physics Letters*, *11*(6), 065102.

Liu, J., Li, X., Xu, Y., Ge, Y., Wang, Y., Zhang, F., Wang, Y., Fang, Y., Yang, F., & Wang, C. (2019). NiPS 3 nanoflakes: a nonlinear optical material for ultrafast photonics. *Nanoscale*, *11*(30), 14383-14391.

Luna Zaragoza, D., Romero Guzmán, E. T., & Reyes Gutiérrez, L. R. (2009). Surface and physicochemical characterization of phosphates vivianite, Fe2 (PO4) 3 and hydroxyapatite, Ca5 (PO4) 3OH.

Martinez, A., & Sun, Z. (2013). Nanotube and graphene saturable absorbers for fibre lasers. *Nature Photonics*, *7*(11), 842-845.

Mary, R., Choudhury, D., & Kar, A. K. (2014). Applications of fiber lasers for the development of compact photonic devices. *IEEE Journal of Selected Topics in Quantum Electronics*, *20*(5), 72-84.

Melton, C. N., Riahinasab, S. T., Keshavarz, A., Stokes, B. J., & Hirst, L. S. (2018). Phase transition-driven nanoparticle assembly in liquid crystal droplets. *Nanomaterials*, *8*(3), 146.

Miyajima, Y., Komukai, T., Sugawa, T., & Yamamoto, T. (1994). Rare earth-doped fluoride fiber amplifiers and fiber lasers. *Optical Fiber Technology*, *1*(1), 35-47.

Mocker, H. W., & Collins, R. (1965). Mode competition and self-locking effects in aq-switched ruby laser. *Applied Physics Letters*, *7*(10), 270-273.

Muhammad, F. D., Zulkifli, M. Z., Latif, A. A., Harun, S. W., & Ahmad, H. (2012). Graphene-based saturable absorber for single-longitudinal-mode operation of highly doped erbium-doped fiber laser. *IEEE Photonics Journal*, *4*(2), 467-475.

Mur, J. (2011). Fiber Lasers.

NASA.(1998).Science@NASA:The Sun Does a Flip. *Science NASA*. https://science.nasa.gov/science-news/science-at-nasa/1998/msad05feb98_1

Ouvrard, G., Brec, R., & Rouxel, J. (1985). Structural determination of some MPS3 layered phases (M= Mn, Fe, Co, Ni and Cd). *Materials research bulletin*, *20*(10), 1181-1189.

Peterka, P., Kasik, I., Dhar, A., Dussardier, B., & Blanc, W. (2011). Theoretical modeling of fiber laser at 810 nm based on thulium-doped silica fibers with enhanced 3 H 4 level lifetime. *Optics express*, *19*(3), 2773-2781.

Poole, S. B., Payne, D. N., & Fermann, M. E. (1985). Fabrication of low-loss optical fibres containing rare-earth ions. *Electronics Letters*, *17*(21), 737-738.

Popa, D., Sun, Z., Torrisi, F., Hasan, T., Wang, F., & Ferrari, A. (2010). Sub 200 fs pulse generation from a graphene mode-locked fiber laser. *Applied Physics Letters*, *97*(20), 203106.

Poulain, M., Poulain, M., & Lucas, J. (1975). Verres fluores au tetrafluorure de zirconium proprietes optiques d'un verre dope au Nd3+. *Materials Research Bulletin*, *10*(4), 243-246.

Semrau, D., Sillekens, E., Killey, R. I., & Bayvel, P. (2020). The benefits of using the S-band in optical fiber communications and how to get there. 2020 IEEE Photonics Conference (IPC),

Set, S. Y., Yaguchi, H., Tanaka, Y., & Jablonski, M. (2004). Laser mode locking using a saturable absorber incorporating carbon nanotubes. *Journal of lightwave Technology*, *22*(1), 51.

Sharma, R., & Raghuwanshi, S. K. (2017). Modeling and analysis of overmodulation in erbium-doped fiber amplifiers including amplified spontaneous emission. *Optical Engineering*, *56*(2), 026105-026105.

Snitzer, E. (1961). Optical maser action of Nd+ 3 in a barium crown glass. *Physical Review Letters*, *7*(12), 444.

Thorlabs. (2023). Thorlabs Optical Fiber Product Page. https://www.thorlabs.com/newgrouppage9.cfm?objectgroup_id=10758

Tippett, J. T., Borkowitz, D. A., Clapp, L. C., Koester, C. J., & Vanderburgh Jr, A. (1965). *Optical and electro-optical information processing*.

Ur Rehman, Z., Muhammad, Z., Adetunji Moses, O., Zhu, W., Wu, C., He, Q., Habib, M., & Song, L. (2018a). Magnetic Isotropy/Anisotropy in Layered Metal Phosphorous Trichalcogenide MPS3 (M = Mn, Fe)Single Crystals. *Micromachines*, *9*(6), 292. https://www.mdpi.com/2072-666X/9/6/292

Ur Rehman, Z., Muhammad, Z., Adetunji Moses, O., Zhu, W., Wu, C., He, Q., Habib, M., & Song, L. (2018b). Magnetic isotropy/anisotropy in layered metal phosphorous trichalcogenide MPS3 (M= Mn, Fe) single crystals. *Micromachines*, *9*(6), 292.

Urquhart, P. (1988). Review of rare earth doped fibre lasers and amplifiers. *IEE Proceedings J (Optoelectronics)*, *135*(6), 385-407.

Valdmanis, J., & Fork, R. (1986). Design considerations for a femtosecond pulse laser balancing self phase modulation, group velocity dispersion, saturable absorption, and saturable gain. *IEEE Journal of quantum electronics*, *22*(1), 112-118.

Wang, F., Shifa, T. A., Yu, P., He, P., Liu, Y., Wang, F., Wang, Z., Zhan, X., Lou, X., Xia, F., & He, J. (2018). New Frontiers on van der Waals Layered Metal Phosphorous Trichalcogenides. *Advanced Functional Materials*, *28*(37), 1802151. https://doi.org/https://doi.org/10.1002/adfm.201802151

Wang, L., Gao, C., Gao, M., Li, Y., Yue, F., Zhang, J., & Tang, D. (2014). A resonantly-pumped tunable Q-switched Ho: YAG ceramic laser with diffraction-limit beam quality. *Optics express*, *22*(1), 254-261.

Wang, M., Han, J., Liu, W., Kamiko, M., & Yagi, S. (2021). Energy storage mechanism of monocrystalline layered FePS3 and FePSe3 as active materials for Mg batteries and pseudocapacitors. *Journal of Alloys and Compounds*, *883*, 160822. https://doi.org/https://doi.org/10.1016/j.jallcom.2021.160822

Zhang, S., Xu, R., Luo, N., & Zou, X. (2021). Two-dimensional magnetic materials: structures, properties and external controls. *Nanoscale*, *13*(3), 1398-1424.

Zhao, J., Wang, Y., Yan, P., Ruan, S., Tsang, Y., Zhang, G., & Li, H. (2014). An Ytterbium-doped fiber laser with dark and Q-switched pulse generation using graphene-oxide as saturable absorber. *Optics Communications*, *312*, 227-232.

Zhou, R., Tang, P., Chen, Y., Chen, S., Zhao, C., Zhang, H., & Wen, S. (2014). Large-energy, narrow-bandwidth laser pulse at 1645 nm in a diode-pumped Er: YAG solid-state laser passively Q-switched by a monolayer graphene saturable absorber. *Applied optics*, *53*(2), 254-258.

Zhu, W., Gan, W., Muhammad, Z., Wang, C., Wu, C., Liu, H., Liu, D., Zhang, K., He, Q., & Jiang, H. (2018). Exfoliation of ultrathin FePS 3 layers as a promising electrocatalyst for the oxygen evolution reaction. *Chemical Communications*, *54*(35), 4481-4484.